Integrated Hydrological Model to Study Surface-Groundwater Interaction in Hard Rock Systems Using an Unstructured Grid Approach, The Sardon Catchment, Spain.

MOSTAFA GOMAA MOHAMED DAOUD
July, 2020

SUPERVISORS:
Dr. Ir. Maciek W. Lubczynski
Dr. Zoltan Vekerdy

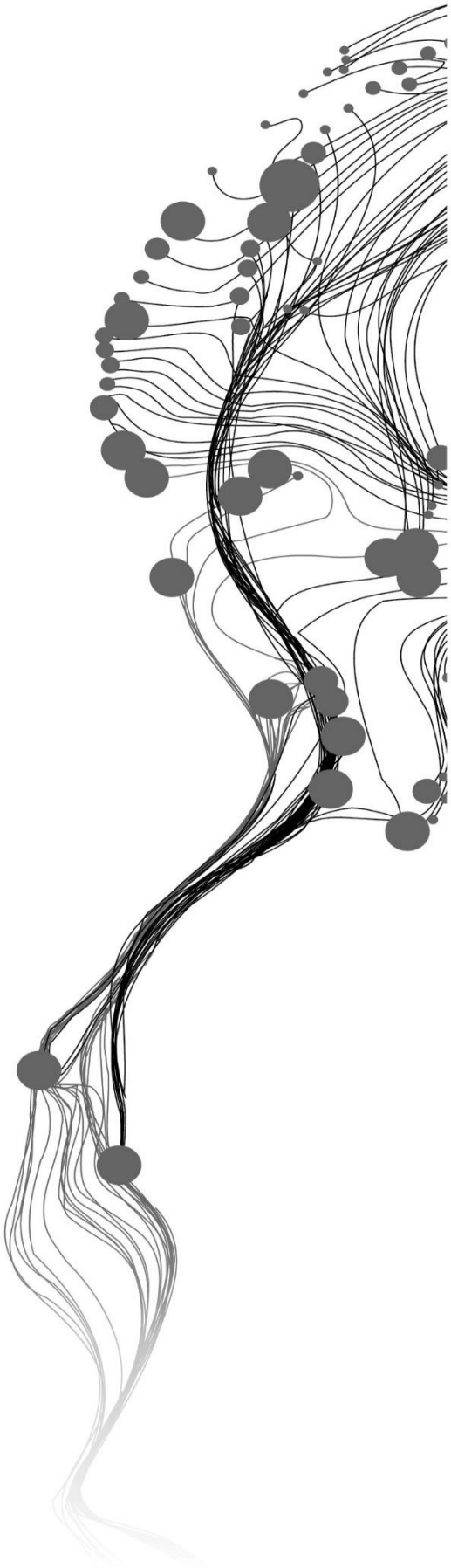

Integrated Hydrological Model to Study Surface-Groundwater Interaction in Hard Rock Systems Using an Unstructured Grid Approach, The Sardon Catchment, Spain.

MOSTAFA GOMAA MOHAMED DAOUD
Enschede, The Netherlands, July, 2020

Thesis submitted to the Faculty of Geo-Information Science and Earth Observation of the University of Twente in partial fulfilment of the requirements for the degree of Master of Science in Geo-information Science and Earth Observation.
Specialization: [Water Resources and Environmental Management]

SUPERVISORS:
Dr.Ir. Maciek W. Lubczynski
Dr. Zoltan Vekerdy

THESIS ASSESSMENT BOARD:
Prof.dr. Bob Z. Su (Chair)
Dr. Jacek Gurwin (External Examiner, University of Wroclaw, Poland)

ABSTRACT

Hard rock systems (HRSs) cover a large proportion of the Earth, widely spreading in different regions of the world. They are characterized by high heterogeneity, dense drainage network, shallow groundwater table and low storage conditions. These characteristics lead to complex surface-groundwater interactions. Moreover, many hard rock systems are classified as water-limited environment (WLE) which are characterized by low precipitation / potential evapotranspiration ($P/PET \leq 0.65$), high spatial and temporal variability of precipitation, 'thirsty' woody vegetation and fast recharge responses reflected by substantial groundwater exfiltration. The areas with both characteristics, HRS and WLE, such as the Sardon catchment (~80 km^2) in Spain, have complex system dynamics. The integrated hydrological models were identified as the most reliable option to study surface-groundwater interaction in such complex systems, also identified as the objective of this study.

For the assessment of Sardon catchment system dynamics, the most recent MODFLOW development of MODFLOW 6 was used, benefiting from its new capabilities in terms of grid flexibility and new concepts, particularly in the water balance representation. The grid used in this study is a Voronoi unstructured grid to realistically represent the main hydrologic features such as the Sardon streams and faults; as compared to previous Sardon modelling efforts, the Voronoi grid allowed to increase the accuracy of representation of the model objects, while code improvements added credibility to the model solution.

The Sardon model was calibrated in transient state over 7-year simulation period using daily groundwater heads and streamflow observation data. The transient simulation showed 7-year mean gross groundwater recharge of 37% of P, but very low net recharge (2% of P) due to significant groundwater exfiltration (26% of P) and groundwater evapotranspiration (9% of P). The net recharge was highly spatially variable with mosaic characteristics influenced by dense drainage network and temporally variable ranging from 22.13 mm.yr^{-1} in wet year 2010 to -6.35 mm.yr^{-1} in dry year 2009.

In this study, a novel concept of re-infiltration of the rejected infiltration and the groundwater exfiltration was introduced to MODFLOW 6. The rejected components contributed significantly to the water balance (together 46% of P), and to the total stream discharge at the catchment outlet (together 92% of q). The re-infiltration concept allows transferring the rejected components from the upslope fully saturated zones to the downslope unsaturated zones. Moreover, the applied methods, particularly the cascade routing (CR) concept, showed better simulation of the overland flow comparing to the previous MODFLOW versions.

The MODFLOW 6, with the modifications implemented in this study, showed a great ability to realistically simulate the surface-groundwater interactions and to define realistic water balance.

Keywords: hard rock systems, water-limited environments, integrated hydrological models, MODFLOW 6, unstructured grid, water balance, re-infiltration concept.

ACKNOWLEDGEMENTS

First and foremost, praise and thanks to Allah (God) almighty who gave me the knowledge and the ability to complete this work.

I would like to express my gratitude to the Netherlands government that gave me the opportunity to do my Master of Science degree at the ITC by providing the financial support through the Orange Knowledge Programme (OKP).

I have no words to describe how much I liked to work under the supervision of Dr. Maciek Lubczynski (my first supervisor). I am very grateful for his guidance, patience and support during the research time. His office was always open for me to come and discuss with him. He was very generous with his knowledge and tips when I need them. He believed in me a lot and always pushed me forward, which gave me more enthusiasm to do my best and work harder. I admit I learned a lot from him, and I was lucky to work under his supervision.

I am also very thankful to Dr. Zoltan Vekerdy, my second supervisor, for his help, advice and encouragement during the research time. His comments and discussions were always valuable for my work to be more precise and professional. He was always thinking with me loudly, which helped me to always think in a critical attitude. I can honestly say that many aspects of my work have been achieved better through his consultations and contributions.

I would like to thank former ITC students (Tanvir Hassan, Alain Frances and Enrico Balugani) for providing me with some data and explanations which were very useful in the research. Special thanks to Mr. Bas Retsios for helping me to fix some coding problems. Also, I am very thankful to Mr Arno van Lieshout, the course director of the department of water resources and environmental management (WREM), and all the teaching staff in the department for their collaboration during my study in ITC.

I would like to express my gratitude to the ITC help desk and the secretary of the WREM department for helping me to rent a laptop for the last two month of my work. I admit that this helps me a lot to finish the research properly. I also thank the ITC's administration for providing all the required arrangements for a pleasant and comfortable stay and education.

Special thanks to the USGS team of MODFLOW 6, especially Mr. Eric Morway for providing me with the MODFLOW 6 version that fixes the bug problem that I faced and also for his discussions with me about some alternatives related to my research.

Last but not least, I would like to thank all my family members, all my colleagues and friends [Fanshu Ma, Daniel and Zhoobin] for their support and encouragement which have led me through the difficult times.

TABLE OF CONTENTS

LIST OF FIGURES

LIST OF TABLES

LIST OF ABBREVIATIONS

$\alpha_{i,j}$	Fraction of flow from the cell i to the neighbouring j cell
α_j	Contributing fraction for each contributing cell, j
α_n	Contributing fraction of cell n
a	Percentage of the area coverage by each landcover class to the total cell area
A	Grid cell area
ADAS	Automated data acquisition system
AI	Aridity index
$A_\perp$	Flow perpendicular area
b_b	Bed thickness to stream reach
b_d	Bed thickness of drain
Bot_1	Bottom elevation of layer one
Bot_2	Bottom elevation of layer two
c	Fractional canopy cover
c_j	Contributing cell
c_m	Connected cell
c_n	Grid cell
$cond$	Drain conductance
CR	Cascade routing
C_u	Conversion coefficient
CVFD	Control volume finite difference
Δ	Slope vapour pressure curve
ΔS	Total catchment storage
ΔS_g	Groundwater zone storage
ΔS_u	Unsaturated zone storage
d_b	Water depth of stream reach
DEM	Digital elevation model
d_{ext}	Extinction depth
$d_{i,j}$	Distance between the centres of the connected i and j cells
DIS	Structured discretization
DISU	Unstructured discretization
DISV	Discretization by vertices
DMHR	Dehesa hard rocks in the western of Iberian Peninsula
d_{surf}	Surface depth where groundwater exfiltration can start
ε	Brooks-Corey exponent
E	Potential evaporation
e_a	Actual vapour pressure
elv	Land surface elevation
EPM	Equivalent porous medium
e_s	Saturation vapour pressure
E_{sf}	Evaporated Canopy interception
ET	Evapotranspiration
ET_c	Crop evapotranspiration
ET_g	Groundwater evapotranspiration
ET_o	Reference evapotranspiration
ET_{oc}	Potential evapotranspiration per unit area of canopy cover
ET_u	Unsaturated zone evapotranspiration

Exf_{gw}	Groundwater exfiltration
Exf_{gw}^{r}	Groundwater exfiltration routed either to downslope UZF cells or to streams
Exf_{gw}^{ri}	Re-infiltrated groundwater exfiltration
Exf_{gw}^{e}	Evaporated groundwater exfiltration
Exf_{gw}^{s}	Groundwater exfiltration routed to streams
γ	Psychrometric constant
G	Soil heat flux density
GHB	General head boundary package
GIS	Geographic information system
GNC	Ghost node package
GUI	Graphical user interface
h_{aq}	Aquifer head
h_b	Stage of stream reach
h_{drn}	Drain elevation
h_m	Observed head
$\overline{h}_m$	Mean of observed head
HRS	Hard rock system
h_s	Simulated head
i_{ET}	Unsaturated evapotranspiration rate per unit depth
IHM	Integrated hydrological model
K_b	Hydraulic conductivity of stream reach's bed
K_c	Crop coefficient
K_{cb}	Basel crop coefficient
K_d	Hydraulic conductivity of drain's bed
K_e	Soil evaporation coefficient
K_h	Horizontal hydraulic conductivity
K_{sat}	Saturated vertical hydraulic conductivity
$K(\theta)$	Vertical unsaturated hydraulic conductivity as a function of water content
K_v	Vertical hydraulic conductivity
LAI	Leaf area index
L_b	Length of stream reach
MAE	Mean absolute error
MFD	Multi flow direction
MVR	Water mover package
n	Number of records
n_b	Manning coefficient of stream reach
$NDVI$	Normalized difference vegetation index
NPF	Node property flow package
NSE	Nash-Sutcliffe coefficient
OBS	Observation package
P	Precipitation
P_e	Effective precipitation
PET	Potential evapotranspiration
q	Total streams discharge at the catchment outlet
q_a	Infiltration rate
q_B	Base flow
q_g	Lateral groundwater outflow at the catchment outlet
QGRID	Quadtree grid

q_{gs}	Groundwater leakage to streams
Q.ilex	Quercus ilex
Q_m	Observed flow
Q_{out}	Flow from the aquifer to the drain
Q.pyrenaica	Quercus pyrenaica
Q_R	Available rate for the receiver package
Q_p	Provided rate
Q_s	Simulated flow
q_{sg}	Streams leakage to groundwater
$\overline{R}$	Average rainfall intensity
R_g	Gross groundwater recharge
RI	Rejected infiltration
RI^e	Evaporated rejected infiltration
RI^r	Rejected infiltration routed either to downslope UZF cells or to streams
RI^{ri}	Re-infiltrated rejected infiltration
RI^s	Rejected infiltration routed to streams
RIV	River package
$RMSE$	Root mean square error
R_n	Net groundwater recharge
R_{net}	Net radiation at crop surface
S	Canopy storage capacity
S_c	Canopy storage capacity per unit area of canopy cover
SFR	Streamflow routing package
$S_{i,j}$	Slope gradient between cell i and j
S_o	Slope of stream reach
s_s	Specific storage
STO	Storage package
s_y	Specific yield
θ	Volumetric water content
θ_i	Initial water content
θ_{ext}	Extinction water content
θ_{resid}	Residual water content
θ_{sat}	Saturated water content
t	Time
T	Potential transpiration
T_{air}	Mean daily air temperature at 2m height
th_1	Layer one thickness
th_2	Layer two thickness
Top_1	Top elevation of layer one
Top_2	Top elevation of layer two
u_2	Wind speed at 2m height
UZF	Unsaturated zone flow package
W_b	Width of stream reach
WLE	Water-limited environment
VE	Volumetric Efficiency
VGRID	Voronoi grid
z	Distance in the vertical direction

1. INTRODUCTION

1.1. General Background

Groundwater is one of the primary water resources that is used everywhere for domestic and irrigation purposes. In arid and semi-arid climate conditions, groundwater is the only source of water to survive droughts, by people, cattle plants and even wildlife if supported by people as it is the case in Southern Africa. However, misuse of the groundwater can lead to problems which are irreversible such as groundwater salinization. Therefore, managing groundwater is critical, especially in areas with limited water resources.

Groundwater is one component of the hydrological cycle which is in a dynamic interaction with other hydrological components. Studying the interaction between these components, especially the surface and the groundwater, interaction is essential for assessing the water resources availability. As the interaction between the surface and the groundwater is complex, most of the current hydrological models focused on modelling either the surface flow alone, such as HBV, PRMS and SWAT or the groundwater flow alone, such as MODFLOW, FEFLOW or AQUIFEM. The concept of these models, further referred as standalone models, is to study either the surface or the groundwater flow, taking the effect of the other, as a simplified input. The main reason for such complexity is the difference between the behaviour of the surface system and the groundwater system in terms of flow and time. The surface flow takes place in a free open medium with relatively high velocities over short time periods comparing to the groundwater flow, which takes place in a porous medium with lower velocities over longer time periods. This leads to high nonlinearity between the two systems' processes with different equations for each one of them and more complexity to couple them in one solution.

The traditional groundwater models (standalone models) simulate only the saturated zone with applying arbitrary recharge. The standalone models do not simulate the unsaturated zone which significantly affects the recharge/discharge conditions of the saturated zone and therefore, applying such arbitrary recharge within the standalone models is very critical and in some cases is unreliable. Recently, a new theme was developed, which is called "Integrated Hydrological Models". The integrated hydrological models (IHMs) are considered as the most reliable among all the models, as they can simulate the interaction between the surface water and the groundwater (Spanoudaki et al., 2009), taking into consideration other hydrological components such as precipitation and evapotranspiration. Furthermore, it can simulate the unsaturated zone and give more representative recharge/discharge conditions of the saturated zone instead of applying such arbitrary recharge as it is the case within the standalone models. Consequently, the IHMs are much more realistic and representative of a real case than standalone models.

1.2. Hard Rock Systems (HRSs)

The entire Earth's land surface is covered by different kind of rocks; crystalline rocks, volcanic rocks and carbonate (sedimentary) rocks (Singhal & Gupta, 2010). Crystalline rocks (referred here as hard rock systems (HRSs)) are the plutonic igneous rocks (granites and diorites) and the metamorphic rocks (gneisses, granulites, quartzites, marbles and schists). The typical profile for the HRS has two layers, the weathered layer, and the fractured layer. The typical weathered layer composed of zones of sandy clay cover, saprolite zone and the parent rock (Singhal & Gupta, 2010). The weathered layer can form a potential aquifer with good water supply in HRSs (Dewandel et al., 2006). The fractured layer is composed of discontinuous fractures that facilitate the storage and movements of fluids through them.

HRSs are well-known with low primary porosity and permeability comparing to other rock types. The groundwater flow occurs in the HRSs, mainly due to the secondary porosity and permeability (formed by faults, fractures, or weathering). The groundwater in HRSs is typically shallow, which leads to fast recharge responses. In HRSs with intensive rainfall events, the water table rises abruptly resulting in groundwater exfiltration to the land surface, short flow paths, and short groundwater residence time (Hassan et al., 2014).

Earlier, HRSs were not given so much attention due to their low productivity (low hydrological conditions such as permeability and storage) and difficulties in water-well drilling (Singhal & Gupta, 2010). However, in many countries, there is still a need for extracting groundwater resources even with low productivity aquifers, especially when other water resources are not available. Therefore, proper groundwater modelling is highly required in such aquifers to evaluate the groundwater resources.

Modelling HRSs (fractured medium) is affected by the characteristics of the fractures (aperture, length, density, orientation, interconnection and filling material). Within different characteristics, multiple conceptual models were developed for describing the groundwater flow in HRSs such as: parallel plate model, double porosity model, discrete fracture network model and equivalent porous medium model (EPM). The EPM is commonly used due to its simplicity as it avoids the fractures characteristics. The EPM is valid to be used for a fractured medium when: (a) fracture density is increased, (b) apertures are constant rather than distributed, (c) orientations are distributed rather than constant, (d) larger sample sizes are tested (Long et al., 1982), (e) the interest is mainly on volumetric flow such as for groundwater supplies (Singhal & Gupta, 2010), and (f) fractures are interconnected with the representative elementary volume (REV) corresponding with the model grid size (Hassan et al., 2014).

The challenge in dealing with the HRSs is their complex structure and high heterogeneity (Hassan et al., 2014). These lead to the complexity of the groundwater flow mechanism and difficulty to understand and simulate the system. The surface-groundwater interaction in HRSs is largely unknown as HRSs are affected by the preferential flow through the faults and the fractures (Hassan et al., 2014). Therefore, the detection of the fault zones and the corresponding hydrogeological parameters is a fundamental need.

Moreover, the complexity of HRSs requires the development of a proper conceptual model. The conceptual model is essential to identify the main aspects that are related to the system such as system processes, the interaction between these processes and the representation of the hydrostratigraphic units (Anderson et al., 2015). Then, the conceptual model is followed by a numerical model which is used to simulate such complex system, particularly the surface-groundwater interaction.

The most well-known numerical code that is widely used for groundwater models is called MODFLOW (McDonald & Harbaugh, 1988). In standard MODFLOW models, the problem domain is discretized using a rectangular finite-difference grid. The finite-difference grid consists of a group of columns, rows and layers. However, there are two limitations for this grid type (Panday et al., 2013). First, some features which have highly irregular shapes cannot be well represented with the traditional rectangular grid. In HRSs, this can be an issue due to the irregularity of the faults and the fracture network. Second, the refinement option cannot be limited only to the areas of interest, and it is carried out through the selected columns and rows till the grid edges. As a result, the model has more unneeded cells resulting in a longer run time. Also, the pinchouts cannot be represented properly as discontinuous layers with the traditional rectangular grid and an arbitrary layer with small thickness of <1 m needs to be defined to represent a pinchout (Anderson et al., 2015).

Furthermore, to deal with the complexity of the HRSs, enough data should be provided, because an insufficient amount of data, particularly monitoring time-series data, in addition to the system complexity, can lead to non-uniqueness and complete meaningless results. In this research, the modelled area is the Sardon catchment (described in section 2), where a good dataset is available including different monitoring time-series records for the last 20 years.

1.3. Water-Limited Environments (WLEs)

For water resources studies, defining the state of the humidity/aridity conditions of the study area can be useful to understand how this particular area react to different water conditions. Several attempts had been made to identify the humidity/aridity conditions based on geomorphic, climatic and vegetational indices. The aridity index (AI) is one of the most relevant indicators, calculated by dividing the annual precipitation (P) by the annual potential evapotranspiration (PET) (Parsons & Abrahams, 2009). The AI can be defined as a bioclimatic index as it takes into account both physical processes (P and PET) and biological processes (plant transpiration) (Salvati et al., 2013). The AI is classified into four classes (hyper-arid regions: AI < 0.05, arid regions: 0.05< AI <0.2, semi-arid regions: 0.2< AI <0.5 and dry sub-humid regions: 0.5< AI <0.65); (figure 1 in Parsons & Abrahams (2009) and table 1 in Salvati et al. (2013). The group of hyper-arid, semi-arid, arid and dry sub-humid areas (which AI < 0.65) can be called together the dry lands or water-limited environments (WLEs) and occupy around ~50% of the global land (Parsons & Abrahams, 2009).

The WLEs are characterized by environmental changes: (a) high spatial and temporal variability of precipitation with typical showers, (b) landcover changes (type and pattern of vegetations), and (c) vulnerable to desertification, groundwater depletion, salinization, soil erosion and nutrients limitation. These changes can have significant ecological, hydrological, and societal impacts. Therefore, ecohydrology science can be useful for such WLEs to understand vegetation-water-nutrients interaction.

The typical vegetations in WLEs are the woody vegetations which are small and patchy. The nature and extent of such woody vegetations are essential for determining biodiversity, wildlife habitat and livestock-grazing (Newman et al., 2006). The WLEs are vulnerable to frequent droughts due to the intermittent and temporal variability of precipitation. Such events can lead to more expanding of the woodlands, most likely due to the ability of the woody vegetations to survive within the WLEs. Newman et al. (2006) had shown an example of landcover changes occurred in San Francisco Peaks, Arizona caused by a combination of drought and infestation by bark beetles between May 2003 and September 2003. His example showed more green trees in September (wet conditions) than in May (dry conditions) (figure 1 in Newman et al. (2006).

The vegetations had a role in the dynamic of the streamflow in WLEs. The typical, frequent high-intensity storms in the WLEs result in overland flow which is the main contributor to the streamflow. With adding the sparseness of the vegetation to these high-intensity storms, overland flow is expected to be increased over short time periods, and channel networks will be formulated (Newman et al., 2006). The streamflow in WLEs has the same characteristics of the overland flow: high intensity, occurred over short time periods, and intermittent.

In WLEs, the interaction between the vegetations and the groundwater recharge is a vital process. The groundwater degradation is expected to occur if changes in climate or land use (large nitrate storage in the vadose zone) result in flushing the vadose zone (Newman et al., 2006). Large-scale of tree removal of eucalypt woody lands in Australia led to the increase of the groundwater recharge rates to two orders of magnitude (Allison et al., 1990). Also, Lubczynski (2009) had indicated that the groundwater resources in a WLE are highly influenced by the existed woody tree species for their survival. Such effects are essential in groundwater balances and groundwater management models.

1.4. Software Selection for HRS-WLE

Study areas represented by HRS-WLE conditions are particularly demanding considering modelling techniques applied. In the last two decades, the U.S. Geological Survey developed several versions of MODFLOW. Each version has its own characteristics and its uniqueness to better simulate specific cases. It is always fundamental for hydrologists to choose the most suitable MODFLOW version to simulate a certain groundwater system with its own conditions. Also, it is

vital to understand the concept of the applied MODFLOW version. The recent MODFLOW improvements went in two directions, towards improving grid flexibility (MODFLOW-USG), and towards improving the model performance (MODFLOW-NWT). The following paragraphs describe those improvements which are related to this research and highlight the most suitable MODFLOW version for this research.

MODFLOW-USG is a version of MODFLOW that can support different types of structured and unstructured grids, compared to other versions of MODFLOW which only work with the traditional rectangular grid. MODFLOW-USG is based on the control volume finite difference (CVFD) which adds flexibility in grid types, cell shapes and sizes (Panday et al., 2013). As MODFLOW-USG provides the option to use different grid types such as rectangles, hexagons, triangles and nested grids with different cell sizes. This flexibility can be used to provide higher accuracy for the groundwater flow calculations and better resolution around the main hydrologic features such as rivers or wells. Furthermore, MODFLOW-USG allows the sub-discretization of individual layers for better representation of the hydrostratigraphic units. Another advantage of MODFLOW-USG is that the refinement option can be limited only to the areas of interest with no need to carry it out till the grid edges as it is the case in MODFLOW-2005. So, the number of cells is reduced, resulting in shorter model run times and better model convergence. However, MODFLOW-USG does not support the UZF package, which simulates the flow in the unsaturated zone (Panday et al., 2013).

MODFLOW-NWT is a version of MODFLOW which can better handle the system nonlinearity by using the Newton method (Niswonger et al., 2011). As a result, MODFLOW-NWT gives the opportunity to better simulate those cases with high nonlinearity such as representing unconfined aquifers, nonlinear boundary conditions and the surface-groundwater interaction. It also handles better the problem of drying-rewetting cells, which sometimes can cause convergence failure of the groundwater flow solution. Additionally, the complex surface-groundwater interaction in HRSs can be better simulated by using the modified SFR and UZF packages in MODFLOW-NWT.

Recently the U.S. Geological Survey developed the latest version of MODFLOW, which is called MODFLOW 6 (Langevin et al., 2017). MODFLOW 6 is an object-oriented framework which supports the use of multiple models within the same simulation (Hughes et al., 2017). MODFLOW 6 includes most of the functions of the previous MODFLOW versions (MODFLOW-2005, MODFLOW-USG, MODFLOW-NWT and MODFLOW-LGR). It is based on a generalized control volume finite-difference in which a cell can be connected to any number of arbitrary cells. It has high flexibility in defining the model grid using one of three different discretization packages (details in section 4.5.2.1). The main advantage of MODFLOW 6 is that multiple models can be incorporated and solved numerically within the same simulation. Using MODFLOW 6 can provide a reliable representation of complex systems such as the HRSs, benefiting from simultaneous use of MODFLOW-USG and MODFLOW-NWT under the same numerical solution.

2. STUDY AREA

The Sardon catchment study area represents typical HRS-WLE conditions. This area has been investigated by multiple studies for the last 20 years. Therefore, there is good ecological and hydrological knowledge about the area. This area also has the advantage of good and long-time records of data which facilities its on-going research.

2.1. Description and Related Work in the Sardon Catchment

The Sardon catchment is located in the western part of Spain about 40 km west of Salamanca city (Figure 1). The catchment's area is about 80 km^2 with altitude that varies from 730 in the north to 860 m a.s.l., in the south. It is mainly composed of weathered and fractured granite with local outcrops of non-fractured rocks, dominantly in the southern,

south-western and north-western parts. The catchment is characterized by well-defined boundaries, semi-arid conditions, rainfall highly temporally variable, ranging from <300 $mm.yr^{-1}$ (2012) to >900 $mm.yr^{-1}$ (2001), low population and therefore low human impact. The main land use is pasture as the soil contains massive weathered granite with low nutrients, and that's why the agriculture activities are rare.

Many previous studies were done before in the Sardon area. Some of them were heavily referred to and their results were used in this study. The following paragraphs illustrate the most relevant works to this research.

Lubczynski & Gurwin (2005) had developed an integrated approach using different sources and different methods to access the spatial-temporal variability of the recharge and the groundwater evapotranspiration fluxes in the Sardon area. Their approach was based on a combination between a GIS-RS environment and a numerical groundwater MODFLOW model. It was one of the few available options at that time to understand the surface-groundwater interaction. However, nowadays, there are new techniques and more powerful models that can better integrate the surface, unsaturated and saturated flow.

Reyes-Acosta & Lubczynski (2013) had mapped the dry season transpiration for two tree species in the Sardon area. Their study had tackled mainly four targets: (a) classify the two tree species using remote sensing techniques, (b) measure the individual tree transpiration using sap flow measurements for both species, (c) upscale the trees transpiration to the catchment scale, and (d) model the dry-season sap-flow variability.

Hassan et al. (2014) had used GSFLOW (Groundwater and Surface-Water Flow) to apply a transient integrated hydrological model in the Sardon area with a quite long time of calibration (18 years). GSFLOW is an integrated hydrological model based on the integration between PRMS (Precipitation-Runoff Modelling System) and MODFLOW which was developed to integrate the surface, unsaturated and saturated flow (Markstrom et al., 2008).

Francés et al. (2014) had developed a multi-technique method for investigating the geometry and the hydrological parameters of the hard rock aquifer in the Sardon area. Their method was based on a combination of remote sensing techniques, hydro-geophysical techniques and hydrological field data acquisition to contribute for designing a conceptual hydrological model. Then, this conceptual model was followed by an integrated numerical model using MODFLOW-NWT (Weldemichael, et al., 2016).

Tekle et al. (2017) had upscaled the groundwater recharge from a small area (80 km^2) of Sardon catchment into a larger area (141,43 km^2) of Dehesa hard rocks in the western of Iberian Peninsula (DMHR). They concluded that the groundwater recharge dynamics is complex due to the spatial-temporal variability of rainfall and evapotranspiration and the system heterogeneity.

Balugani et al. (2017) had partitioned the evapotranspiration process into evaporation and transpiration, define their source either from the saturated or the unsaturated zones and estimate their contributions. They concluded that for arid and semi-arid areas with sparse vegetation, the often-neglected groundwater evaporation is a relevant contribution to evapotranspiration and that the water vapour flow should be taken into account in the calculation of extinction depth.

Hassan et al. (2017) had estimated the rainfall interception of the two tree species by: (a) rainfall, throughfall and stemflow measurements during two-year period, (b) Gash model temporal extrapolation, and (c) remote sensing spatial upscaling. Their proposed method is expected to improve catchment water balances, replacing common arbitrary or literature-based tree interception loss estimates.

2.2. Climate Conditions

The area has a Mediterranean climate with semi-arid conditions, and typical for the Central Iberian Peninsula. The mean precipitation in the period of 1951-2012 was 586 mm.yr^{-1} with a standard deviation of 179 mm.yr^{-1} (Hassan et al., 2014). The driest months are July and August with a mean precipitation of < 20 mm.month^{-1}, while the wettest months are October and November with a mean precipitation of > 70 mm.month^{-1}. The warmest months are July and August with a mean temperature of 20°C and mean potential evapotranspiration of 5 mm.day^{-1}. The coldest months are January and February with a mean temperature of 5°C and the lowest potential evapotranspiration is in December and January, on average ~ 0.5 mm.day^{-1} (Lubczynski & Gurwin, 2005).

2.3. Topography

The terrain elevation of the catchment ranges from 730 m a.s.l along the main fault zone (catchment's central) to 860 m a.s.l at the watershed boundaries. The southern parts, which are composed of granites and impermeable schists have higher elevations, while the northern parts are relatively flat with lower elevations. The western parts are marked by outcrops of non-fractured rocks composed of granites and impermeable schists and fractures filled with quartzite material along the eastern boundary (Hassan et al., 2014). The central area has steeper slopes due to the existence of the Sardon river and its tributaries (Figure 1).

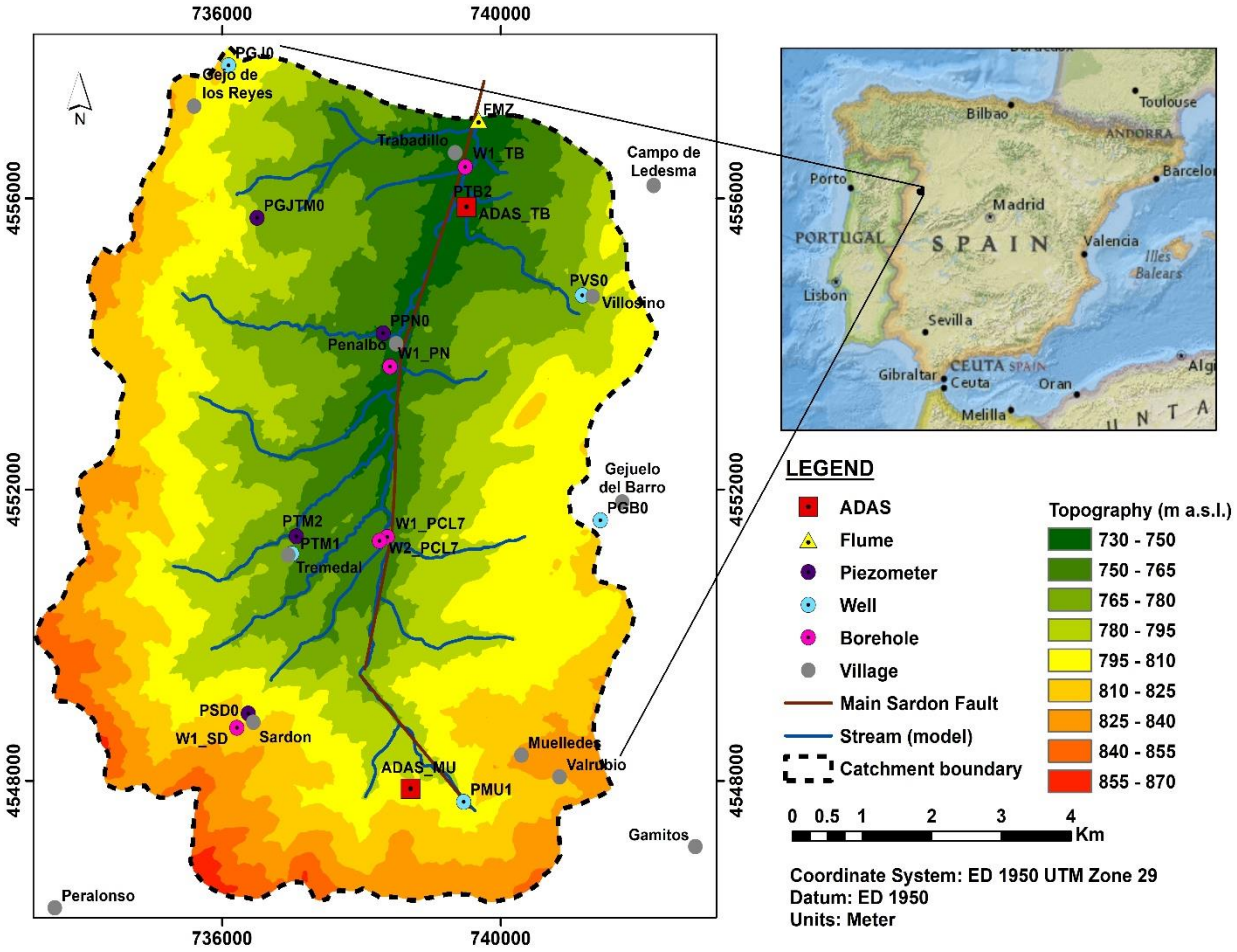

Figure 1: Base map of the catchment with topography and monitoring network.

2.4. Land Cover

The area is mainly a pasture land where the grass is dominant only for three months (from April to June) per year, and in the rest of the year is bare soil (Francés, 2015). The area is characterized by natural woody shrub vegetation with ~ 7% sparse coverage of two tree species: evergreen oak (*Quercus ilex*), and broad-leafed deciduous oak (*Quercus pyrenaica*) (Reyes-Acosta & Lubczynski, 2013). The topographic boundaries are marked by outcropping and shallow sub-cropping of massive non-fractured rocks (Lubczynski & Gurwin, 2005). These different landcover types can affect the system dynamic and have to be reflected in the model parameterization; therefore, a classification map is needed. Francés et al. (2014) had mapped the granite outcrops in the area using two high-resolution multi-spectral satellite images (Quickbird from August 2009 and Worldview-2 from December 2012), while Reyes-Acosta & Lubczynski (2013) had used the same images to classify the two tree species with overall accuracy 90%. The two maps of Francés et al. (2014) and Reyes-Acosta & Lubczynski (2013) were combined together to get a landcover classification map with the identification of whether the trees are grown on soil or outcrops. The classification map has 6 landcover classes, shown in Figure 2.

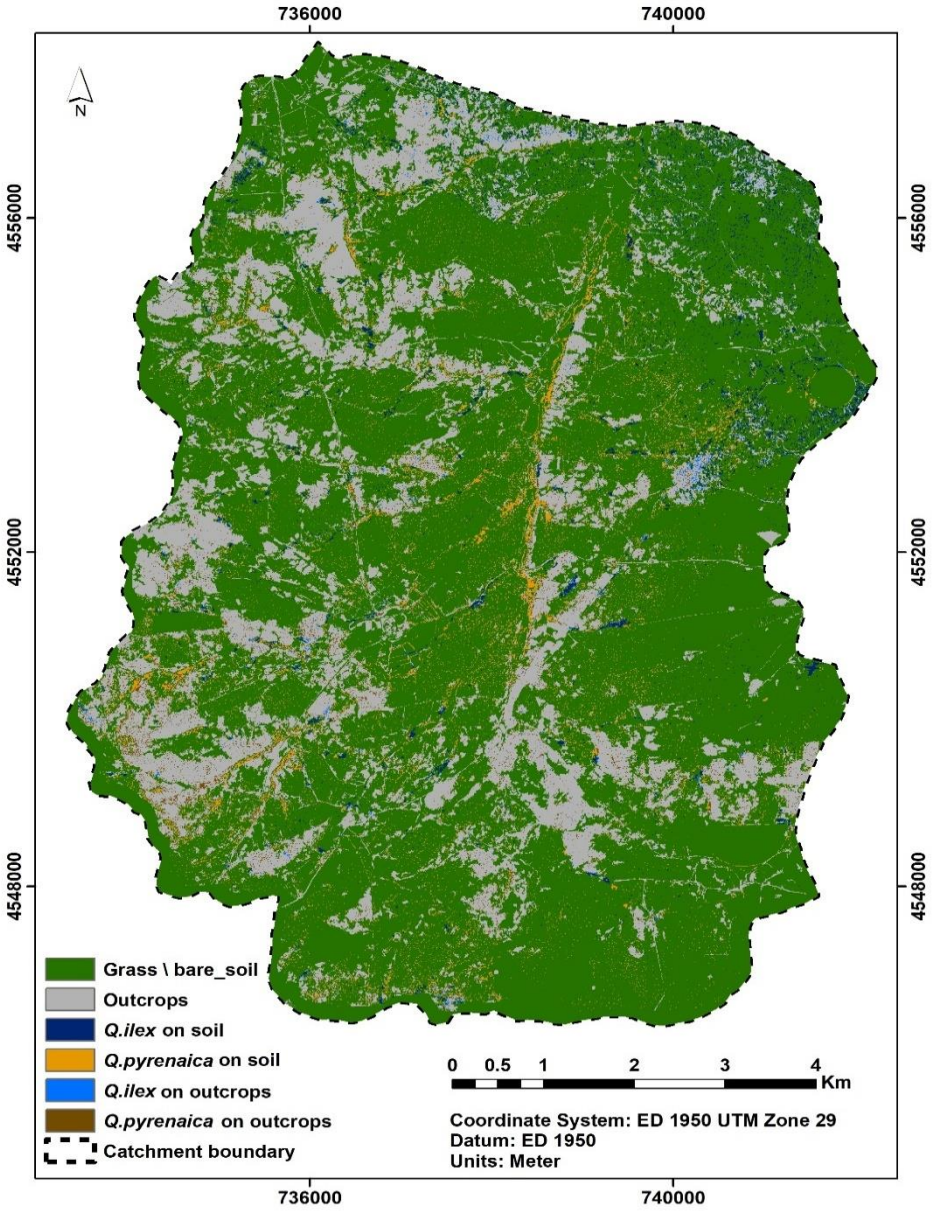

Figure 2: Landcover classification map.

2.5. Hydrology

The area is characterized by a dense network of faults which are mainly oriented in the NE-SW direction (Francés et al., 2014). The fault network was obtained from Francés et al. (2014) through the application of high pass filter on a high-resolution digital terrain model (DTM). They showed that there is a main fault which goes parallel to the Sardon river, while a set of secondary faults, linked with the main fault affect the catchment hydrology by controlling the direction of the tributaries of the Sardon river. The main fault divides the area into two geomorphologically different parts, a gentler undulating western part and a steeper undulating eastern part. Along the main fault, there is an open fracture zone which is filled in with alluvial deposits and weathered materials. This zone was eroded in the rock basement and filled in with deposits and weathered rocks, creating a channel fill structure (Lubczynski & Gurwin, 2005). The main fault and the channel-fill structure are both permeable and hydraulically connected (acting as groundwater drainage). The tributaries of the Sardon river drain the water by gravity (direct runoff) to the Sardon river, from mid-October to mid-June, while at the remaining period, the Sardon river and its tributaries are typically dry. There are also artificially-made ponds supplying water for cattle's; some of these ponds dry up in dry seasons, while others, those that bottom below the lowest groundwater level, do not dry up, indicating groundwater table position.

2.6. Hydrogeology

The hydrogeological framework of the study area consists of three layers which were defined by Lubczynski & Gurwin, (2005) as shown in Figure 3. The first layer is an unconsolidated layer of weathered material and alluvial deposits with thickness ranges from 0 to 10 m and limited areal extent due to the abundant of the bedrock outcrops. The second layer is a fractured granite layer with thickness varying from 0 m in the upland parts to 60 m in the central part of the catchment. The third layer is a massive granite layer, which is assumed as impermeable basement.

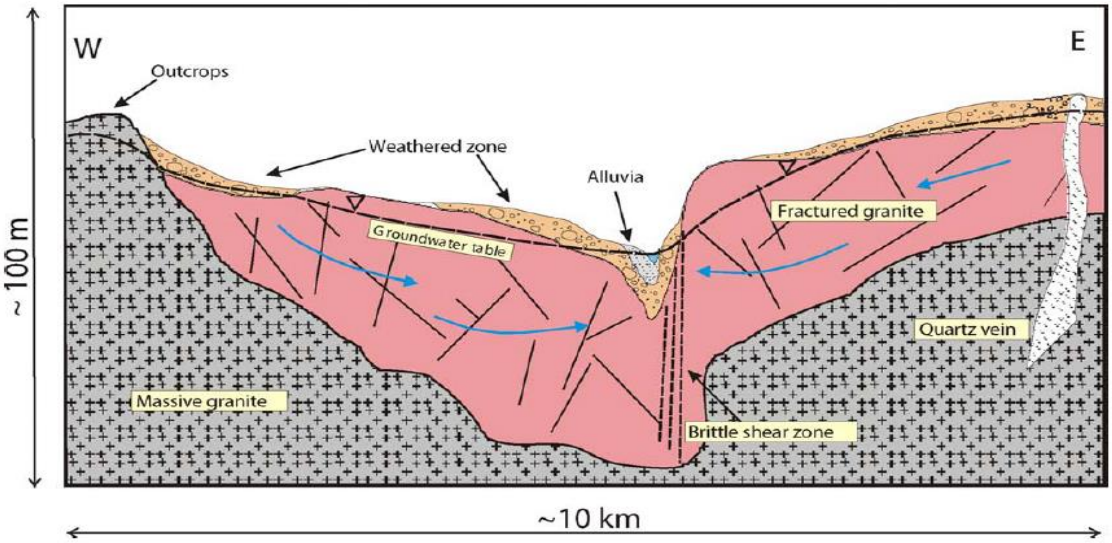

Figure 3: Schematic cross-section (Lubczynski & Gurwin, 2005).

The groundwater levels are typical for a granitic basin, shallow in the Sardon river's valleys in the range of 0-3 m depth below the ground surface (b.g.s), and deeper at the catchment divides, ranging from 1 to 12 m b.g.s (Lubczynski & Gurwin, 2005). The two layers had a similar potentiometric pattern, which follows the topography of the study area. Groundwater conditions are strongly influenced by the Sardon main fault and its drainage of the Sardon river with its tributaries (Hassan et al., 2014).

2.7. Monitoring Network

In the Sardon catchment, there are two ADAS (automated data acquisition system) stations that were implemented to monitor the desired hydrological variables. The first one is in the northern boundary (Trabadillo), while the other one (Muelledes) is in the southern boundary of the catchment, as shown in Figure 1. ADAS station is a system of different sensors with data loggers that record the data on hourly basis (Lubczynski & Gurwin, 2005). The recorded data are climatic variables, particularly the rainfall, air temperature, wind speed, relative humidity, incoming and outgoing radiation. All these climatic variables were used for estimating the system's driving forces. More details about the set-up of the ADAS stations can be found in Lubczynski & Gurwin (2005). Moreover, there is a spatially distributed groundwater monitoring network, which was established gradually since 1994 (Figure 1). This network includes several piezometers, boreholes and wells. The measurements are taken on an hourly basis, therefore a set of good time-series of the groundwater measurements is available. Additionally, the network includes measurements of the low flows at the catchment outlet point, at the northern boundary using a steel flume, with the maximum discharge capacity of 145 $l.s^{-1}$ for the period of 1997-2001. Next to the flume, there is a piezometer to monitor the groundwater levels. The water levels in the piezometers were closely linearly correlated to the flume levels. Thus, the regression curve that was created by Hassan et al. (2014) can be used to extrapolate the stream flows during the periods when the low flows were not measured in the flume.

3. RESEARCH OBJECTIVES AND QUESTIONS

3.1. Problem Statement

The Sardon catchment has been investigated by many previous studies, which went in different directions, as described in section 2.1. However, the research in this area is still on-going, and new challenges are coming out as still some problems are not solved yet. The Sardon catchment includes the characteristics of both HRSs and WLEs. The area has a complex structure with high heterogeneity, shallow groundwater with fast responses to recharge and is affected by preferential flow through the fractures. Additionally, the area has limited water resources, high temporal variability of precipitation and woody vegetation that affect streamflow and groundwater. These conditions lead to many challenges when studying the hydrology of the area. The problems that seem not to be solved yet are the following:

- The estimation of the effective precipitation (affected by interception) in the previous studies did not account for the spatial-temporal variability due to different landcover. The main land cover in the area is the grass which is dormant and seems from the first sight to have low rates of interception. However, this needs to be confirmed by a better estimation of grass interception instead of using arbitrary interception rates. Additionally, the area has two types of tree species which had different interception rates as described in Hassan et al. (2017). These rates were not implemented in the previous studies numerical groundwater models. Implementing spatial-temporal effective precipitation in a numerical groundwater model will lead to more representative water balance.
- The potential evapotranspiration was estimated in previous studies based on; either the modified Jensen-Haise formulation (Hassan et al., 2014), or the crop evapotranspiration with applying an average crop coefficient (K_c) (Weldemichael, et al., 2016). The estimation of the PET is expected to be improved with applying spatial-temporal K_c. Implementing spatial-temporal PET in a numerical groundwater model will lead to more representative water balance.
- The typical grid type which is used in the groundwater numerical models (including the related previous studies) is the rectangular grid. The rectangular grid has difficulty in representing the irregular features such as the

streams in the Sardon catchment. Using the unstructured grid approach will improve the representation of the Sardon streams and is expected to enhance the simulation of the surface-groundwater interaction and improve the hydrological knowledge of the Sardon catchment.

- Improving the conceptual model of the Sardon catchment with the use of new modelling techniques is expected to enrich the hydrological and ecological knowledge of the Sardon catchment. MODFLOW 6, which is the last version of MODFLOW, has the advantage of including most of the previous versions' functions in addition to new capabilities that can be useful for the Sardon model. For example, the calculations of the water balance components (rejected infiltration and groundwater exfiltration) are handled better and become more realistic in MODFLOW 6 comparing with the earlier versions.

The objectives of this research are based on solving those problems with making good use of the previous related studies in the area in addition to using new techniques in terms of conceptual and numerical modelling.

3.2. Objectives

The main objective of this research is to investigate surface-groundwater interaction in hard rock, water-limited environments applying new, MODFLOW-modelling developments and using Sardon catchment as a case example.

Sub-objectives

- Provide the most reliable unstructured grid type for the Sardon catchment model.
- Apply the latest version of MODFLOW (MODFLOW 6) with its new capabilities.
- Define the water balance of the Sardon catchment.
- Improve the knowledge of the Sardon catchment hydrology using the unstructured grid and MODFLOW 6 approach.

3.3. Research Questions

Main question:

How the use of new, MODFLOW-modelling developments can improve the hydrological knowledge of surface-groundwater interaction in hard rock, water-limited environments?

Specific questions

- What is the most reliable unstructured grid type for the Sardon catchment?
- What are the advantages of using MODFLOW 6 in hard rock, water-limited environment?
- What are the main hydrological components of the Sardon's catchment water balance?
- Can Sardon's catchment knowledge be improved using the unstructured grid and MODFLOW 6 approach?

4. RESEARCH DESIGN AND METHOD

4.1. Methodology Flowchart

The proposed methodology consists of four phases summarized in a flowchart (Figure 4)

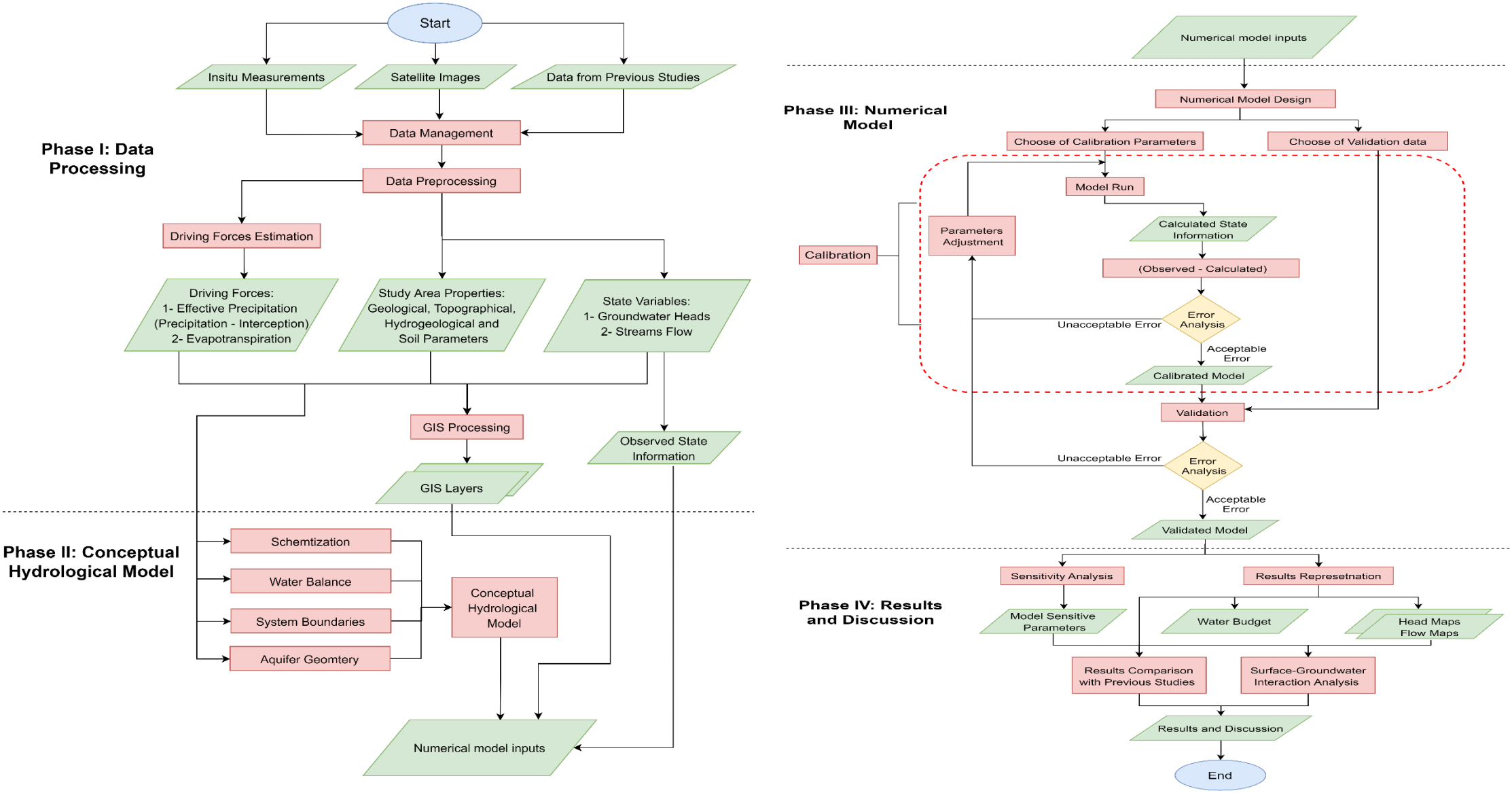

Figure 4: Methodology flowchart.

4.2. Data Preprocessing

The data has been collected from different sources, particularly in-situ measurements, satellite images and from previous studies and has different formats and types. Therefore, preprocessing steps were used to organize the data, change the binary format to readable ASCII format and store it in a feasible structure. The GIS (Geographic Information System) is the most powerful environment to manage and handle different types of geospatial data in one structure. It is quite common with hydrological models to use GIS for managing and processing the datasets. In GIS, the data with different types can be converted to layers (raster or vector layers). The following steps show the main general concept of data preprocessing that was used

- Raw data such as binary files, text files and sheets were converted to vector or raster layers.
- Same format and resolution were defined to all the rasters.
- One spatial reference (coordinate system) was defined to all the layers using projection tools.
- A geodatabase was built to store all the data feasibly.

Integrated hydrological models require information about three main components, the driving forces, the variables (state and rate), and the system parameters. The driving forces and the variables are changing spatially and temporally, while the system parameters are changing only with space. The system parameters are recognized by the system properties, particularly the topographical, geological, soil and hydrogeological properties. All these properties were discussed through sections 2.2 to 2.6 and their corresponding parameters were implemented in the conceptual and the numerical model (sections 4.4 and 4.5). The state and rate variables were retrieved from the monitoring network (section 2.7) and were implemented later in the numerical model (section 4.5). In this study, the main driving forces are the effective precipitation (influenced by the interception) and the evapotranspiration. Each driving force needs to be directly measured or estimated. The following section describes the procedure of getting the driving forces.

4.3. Driving Forces

4.3.1. Effective Precipitation (Infiltration)

The precipitation that can be used as recharge in the integrated hydrological models is the effective precipitation (precipitation – interception), and that's why interception is a significant process and needs to be estimated. Effective precipitation (later referred to as the infiltration in the numerical model, section 4.5.5.2) is the main, most important input data type used in the integrated hydrological models.

4.3.1.1. Precipitation

The precipitation is being monitored on hourly basis using the tipping buckets that are installed in the two ADAS stations (Figure 1). The hourly precipitation records were lumped to daily records to match the temporal discretization of the numerical model that was used (section 4.5.3). The Trabadillo ADAS station was selected to represent the precipitation in the area as the spatial difference of the measurements between the two stations was not significant (Lubczynski & Gurwin, 2005).

4.3.1.2. Interception

Interception is the amount of rainfall that is captured by the vegetation canopy and does not reach to the ground. Hassan et al. (2017) had estimated the interception rates for the two tree species (*Q.ilex* and *Q.pyrenaica*) for two years (2012

and 2013). Then, they temporally extrapolated the interception rates to cover the period (2009-2014) using Gash's revised analytical model (Gash et al., 1995). However, their study focused on the tree interception and did not study the grass interception in the area. Therefore, the same approach of Gash's revised analytical model is used hereafter, to derive the interception losses of the grass. The Gash's model (Eqs. (1), (2)) assumes rainfall to occur as a series of discrete events. Each event consists of three periods: (a) wetting up period, when rainfall P is less than the amount of rainfall required to fully saturate the canopy, $P`$ (Eq. (1)); (b) saturation period, when rainfall rates ≥ 0.5 mm hr^{-1} (Gash, 1979); and (c) drying out period, after rainfall ceases. Defining the rainfall events according to these periods is a time-consuming process which is out of the scope of this research. Therefore, for simplicity, the period of one day was assumed to be a discrete event, as Gash et al. (1995) already mentioned the validity of this assumption.

Gash's Formula

$$P` = -\frac{\overline{R} * S_c}{\overline{ET}_{oc}} * \ ln\left[1 - \frac{\overline{ET}_{oc}}{\overline{R}}\right] \quad (1)$$

$$E_{sf} = \begin{cases} c * \sum_{j=1}^{m} P & \text{for } m \text{ small storms}, P < P` \\ (ncP` - ncS_c) + \left[\left(c * \overline{ET}_{oc} \middle/ \overline{R}\right) \sum_{j=1}^{n} (P - P`)\right] + (ncS_c) & \text{for } n \text{ storms}, P \geq P` \end{cases} \quad (2)$$

$$S_c = S/c \quad (3)$$

$$\overline{ET}_{oc} = \overline{ET}_o/c \quad (4)$$

where:

		Notations used in Gash et al. (1995)	
$P`$	Amount of rainfall needed to saturate the canopy	P'_G	[mm.day^{-1}]
P	Rainfall	P_G	[mm.day^{-1}]
E_{sf}	Canopy Interception	-	[mm.day^{-1}]
$\overline{R}$	Mean rainfall intensity	$\overline{R}$	[mm.day^{-1}]
S	Canopy storage capacity	S	[mm.day^{-1}]
c	Fractional canopy cover	c	[m^2.m^{-2}]
ET_o	Reference evapotranspiration (calculated by Penman-Monteith method)	-	[mm.day^{-1}]
$\overline{ET}_o$	Mean reference evapotranspiration during the day = $ET_o/24$	$\overline{E}$	[mm.day^{-1}]
S_c	Canopy storage capacity per unit area of canopy cover	S_c	[mm.day^{-1}]
$\overline{ET}_{oc}$	Mean reference evapotranspiration per unit area of canopy cover	$\overline{E_c}$	[mm.day^{-1}]

The daily rates of rainfall and reference evapotranspiration were calculated in separate sections (4.3.1.1 and 4.3.2.1). In order to apply Gash's model, there are two main variables that are related to the canopy properties (canopy storage capacity (S) and canopy cover (c)). The c of the grass was assumed to be 0.5 of the total grass area and was later noticed that in this study area, it does not have a significant effect on the final interception rates. Considering S, the leaf area index (LAI) is a very good predictor as proved in many previous studies (Vegas Galdos et al., 2012; Gómez et al., 2001).

Many studies derived relationships between LAI and S for different kind of crops such as Menzel (1997) who derived a $LAI\&S$ formula for a grassland applied in this study (Eq. (5)), where the LAI for the grass was retrieved using a series of the multi-spectral Sentinel-2 images with the L2B biophysical processor of SNAP software. However, the climatic and soil conditions of the study area analysed by Menzel (1997) was different from the Sardon area (clay-sandy soil compared to hard rock for the Sardon area, cooler climate and higher average precipitation than the Sardon area). These different conditions can affect the validity of applying this formula in the Sardon area, and more investigations of a specific $LAI\&S$ formula for the Sardon area is recommended for future studies.

Menzel's formula $$S = 1.2 * \log(1 + LAI) \quad (5)$$

The LAI is a biophysical parameter which is not linearly related to the reflectance. LAI (actual LAI) is not directly accessible from remote sensing due to the heterogeneity in the leaf distribution within the canopy volume. Therefore, the LAI retrieved by remote sensing is the effective LAI, not the actual LAI (Weiss & Baret, 2016). Figure 5 shows the monthly LAI values for the year October 2017- September 2018. There was no option to retrieve the LAI from remote sensing in the same period of other input data of this study (October 2007 - September 2014), as the Sentinel-2 images are available only from 2015. Therefore, the retrieved LAI values at the period (October 2017- September 2018) were assumed to be valid for the period of other input data of this study.

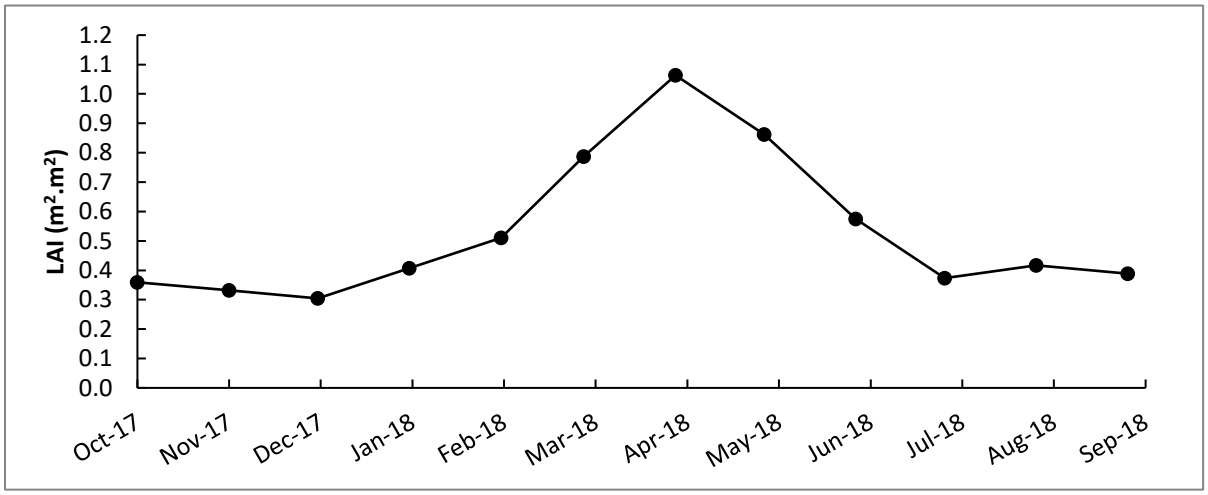

Figure 5: Monthly LAI for the grass.

By substituting the retrieved monthly LAI in Equation (5), the S were calculated monthly with the assumption that S is constant along every month. With these daily values of S next to the daily rainfall and potential evapotranspiration values (calculated in separate sections 4.3.1.1 and 4.3.2.1), the Gash's formula was applied to get the daily grass interception losses. These interception rates represented the interception rates of the landcover class (grass \ bare soil), as it was mentioned in section 2.4 that the grass is dominant only three months per year and the rest is bare soil where the grass acts as dormant but still can intercept water.

The daily interception rates of the two tree species were retrieved from Hassan et al. (2017). The differentiation between the trees whether they are grown on soil or outcrops does not have an impact on the interception rates and therefore the interception rates for the landcover classes *Q.ilex* on soil and *Q.ilex* on outcrops are equal and the same for *Q.pyrenaica* on soil and *Q.pyrenaica* on outcrops. The landcover class (outcrops) has zero interception rates. The final interception rates for the six land cover classes are shown in section 5.1.1 and were implemented in the numerical model (section 4.5.5.2).

4.3.2. Potential Evapotranspiration ($\boldsymbol{PET}$)

Evapotranspiration (ET) is the combination of two processes, the evaporation from the soil and the transpiration from the vegetation canopy. It is quite common in many hydrological studies to combine them together as ET because of the partitioning complexity. Potential evapotranspiration is the upper limit of the evapotranspiration from the vegetation canopy that can occur under infinite energy and water supply. McMahon et al. (2013) had defined the PET as *'' the rate at which evapotranspiration would occur from a large area completely and uniformly covered with growing vegetation which has access to an unlimited supply of soil water, and without advection or heating effects.*''. In IHMs, PET is a model input that is used to calculate the actual evapotranspiration through the UZF package. There are a lot of models which can be used to calculate PET (McMahon et al., 2013). Table 4 in McMahon et al. (2013) summarized the practical

application of each model according to the study purpose. In this study, PET was calculated using the general Penman-Monteith model with the FAO guidelines (Allen et al., 1998).

4.3.2.1. Reference Evapotranspiration ($\boldsymbol{ET_o}$)

ET_o is the potential evapotranspiration for a hypothetical grass reference crop with specific characteristics (height = 12 cm, surface resistance = 70 s m^{-1} and albedo = 0.23) (Allen et al., 1998). The FAO Penman-Monteith method requires only meteorological data, particularly the net radiation, wind speed, air temperature and relative humidity to calculate ET_o as shown in Equation (6).

$$ET_o = \frac{0.408\,\Delta\,(R_{net} - \mathrm{G}) + \gamma\,\frac{900}{T_{air} + 273}\,u_2\,(e_s - e_a)}{\Delta + \gamma\,(1 + 0.34\,u_2)} \qquad (6)$$

where:

ET_o	Reference evapotranspiration	[mm.day^{-1}]
R_{net}	Net radiation at crop surface	[MJ.m^{-2}.day^{-1}]
G	Soil heat flux density	[MJ.m^{-2}.day^{-1}]
T_{air}	Mean daily air temperature at 2m height	[°C]
u_2	Wind speed at 2m height	[m.s^{-1}]
e_s	Saturation vapour pressure	[KPa]
e_a	Actual vapour pressure	[KPa]
$e_s - e_a$	Saturation vapour deficit	[KPa]
Δ	Slope vapour pressure curve	[KPa °C^{-1}]
γ	Psychrometric constant	[KPa °C^{-1}]

All the needed metrological data were retrieved from the ADAS station hourly records and were lumped to get the daily ET_o. The soil heat flux is high in the daytime and low at night, so the total daily G is close to zero.

4.3.2.2. Crop Evapotranspiration ($\boldsymbol{ET_c}$)

ET_c is the evapotranspiration of crops from disease-free, well-fertilized, grow in large fields, under optimum soil water conditions and achieving full production under the given climatic conditions (Allen et al., 1998). The difference between the crop characteristics and the reference grass characteristics is integrated into the crop coefficient (Eq. (7)). In this study, PET = ET_c.

$$ET_c = ET_o * K_c \qquad (7)$$

$$PET = ET_o * K_c \qquad (8)$$

where:

ET_o	Reference evapotranspiration	[mm.day^{-1}]
ET_c	Crop evapotranspiration	[mm.day^{-1}]
K_c	Crop coefficient	[-]

The crop coefficient is different from one crop to another. The FAO guidelines include tables for K_c for different crops but not for natural vegetation as in this study area, so they are not included in these tables. Therefore, some investigations were done to estimate more representative values for K_c.

4.3.2.3. Crop Coefficient ($\boldsymbol{K_c}$)

There are two methods to define the crop coefficient (single crop coefficient and dual crop coefficient). The single crop coefficient (K_c) deals with the evapotranspiration process while the dual crop coefficient splits K_c into two separate

coefficients, one for evaporation process (K_e) and the other one for transpiration process (K_{cb}). In this study, the dual crop coefficient was estimated with some assumptions for the landcover classes defined in the study area (Figure 2).

$$K_c = K_e + K_{cb} \quad (9)$$
$$K_e = E/ET_o \quad (10)$$
$$K_{cb} = T/ET_o \quad (11)$$
$$PET = (K_e + K_{cb}) * ET_o \quad (12)$$

where:

K_c	Crop coefficient	[-]
K_e	Soil evaporation coefficient	[-]
K_{cb}	Basel crop coefficient	[-]
E	Potential evaporation	[mm.day^{-1}]
T	Potential transpiration	[mm.day^{-1}]

4.3.2.4. Soil Evaporation Coefficient (K_e)

K_e was estimated based on the results of the previous studies in the Sardon area. The evaporation from the soil was calculated for two years by Balugani et al. (2017). The first year started from October 2008 to September 2009 and named as the year 2009, while the second year began from October 2009 to September 2010 and named as the year 2010. The year 2009 is considered as a dry year with total rainfall of 320 mm.yr^{-1}, while the year 2010 had a total rainfall of 750 mm.yr^{-1} (wet year). The evaporation measurements that were done by Balugani et al. (2017) represent the actual evaporation, especially in the dry year, where the rainfall is limited. Therefore, the wet year 2010 is more closely to represent the potential evaporation where there is less or no water stress.

The 2010 time series of the soil evaporation values obtained by Balugani et al. (2017) was divided by the ET_o values to get the monthly values of K_e for the grass \ bare soil landcover (Eq. (10)). All other landcover classes were related to the grass \ bare soil class. The outcrops in the study area which represent the outcrops landcover class are fractured with detecting some portion of grass on them; therefore, it was an indicator that the outcrops still can store water and the evaporation process occurs but not with the same evaporation rates as the soil. Due to the difficulty of estimating the evaporation rates of the fractured outcrops, K_e values for the outcrops landcover class were assumed to be 0.5 of the grass \ bare soil landcover class (Eq. (13)).

For the two landcover classes (*Q.ilex* on soil and *Q.pyrenaica* on soil), K_e values of the soil under the two tree species were estimated as a percentage between the average evaporation rate of the grass \ bare soil (0.55 mm.day^{-1}) to the average transpiration rates (0.83 mm.day^{-1} for *Q.ilex* and 1.19 mm.day^{-1} for Q.*pyrenaica*) (Eqs. (14), (15)).

For the two landcover classes (*Q.ilex* on outcrops and *Q.pyrenaica* on outcrops), the same assumption was used again for the outcrops under the trees (K_e for outcrops under trees = 0.5 of K_e for soil under trees) (Eqs. (16), (17)).

As a result, the K_e for soil under *Q.ilex*, outcrops under Q.ilex, soil under *Q.pyrenaica* and outcrops under *Q.pyrenaica* were around (60%, 50%, 30%, 25% respectively) of the K_e of the grass \ bare soil.

$$K_{e2} = 0.5 * K_{e1} \quad (13)$$
$$K_{e3} = 0.55/0.83 * K_{e1} \quad (14)$$
$$K_{e4} = 0.55/1.19 * K_{e1} \quad (15)$$
$$K_{e5} = 0.5 * K_{e3} \quad (16)$$
$$K_{e6} = 0.5 * K_{e4} \quad (17)$$

where:

K_{e1}	Soil evaporation coefficient for the grass \ bare soil	[-]
K_{e2}	Soil evaporation coefficient for the outcrops	[-]
K_{e3}	Soil evaporation coefficient for the soil under *Q.ilex*	[-]
K_{e4}	Soil evaporation coefficient for the soil under *Q.pyrenaica*	[-]
K_{e5}	Soil evaporation coefficient for the outcrops under *Q.ilex*	[-]
K_{e6}	Soil evaporation coefficient for the outcrops under *Q.pyrenaica*	[-]

4.3.2.5. Basal Crop Coefficient (K_{cb})

For estimating K_{cb}, many studies relate the transpiration rates to the vegetation indices such as (normalized difference vegetation index (NDVI) and soil adjusted vegetation index (SAVI)). Choudhury et al. (1994) had derived a linear relationship between K_{cb} and NDVI for wheat, while Campos et al. (2010) did the same but for vineyard which was later used by Campos et al. (2013) for retrieving K_{cb} for *Q.ilex* in the Dehesa region. The same approach was used to get the monthly K_{cb} values for all the landcover classes using NDVI. The NDVI values were retrieved from a series of Landsat 7 TM images (from October 2009 to September 2010). Then, the two formulas derived by Choudhury et al. (1994) and Campos et al. (2010) were tested, and both give close K_{cb} values despite the fact that more accurate relationship can be obtained for the study area vegetations if there is enough data for the transpiration rates.

Choudhury's Formula	$K_{cb} = (1.46 * NDVI) - 0.26$	(18)
Campos' Formula	$K_{cb} = (1.44 * NDVI) - 0.1$	(19)

The K_{cb} for the grass grown between the fractured outcrops (outcrop landcover class) were assumed as 0.5 of the grass \ bare soil landcover (same ratio as K_e between outcrops to grass \ bare soil). Moreover, the K_{cb} retrieved for the trees on outcrops were almost the same as the trees on soil.
Finally, K_e and K_{cb} were added to get the final K_c values, as shown in Figure 13 and Table 7. These K_c values were assumed to be generic and applicable for every year. K_c values were used in Equation (12) to get the PET values for each landcover class which were implemented later in the numerical model (section 4.5.5.2).

4.4. Conceptual Hydrological Model

4.4.1. Schematization

In IHMs with applying MODFLOW 6, the hydrological processes that can be simulated are the ones that occurred in the subsurface zone. The effect of the land surface processes can also be added in terms of driving forces to the subsurface zone. Figure 6-a and b show two schematized representation of the system zones and components with different conditions (wet and dry seasons).

4.4.2. System Boundaries

The boundaries of the Sardon catchment were defined first by Lubczynski & Gurwin (2005). The catchment boundaries are characterized by a watershed divide that surrounds the whole catchment except at the Sardon river outlet at the northern boundary (Figure 1). The aquifer has three layers, as shown in Figure 3, where the third one is a massive granite impermeable layer. The only external recharge to the system is the precipitation, while the main outputs are the evapotranspiration, lateral groundwater flow and the runoff through the Sardon river and its tributaries through the catchment outlet at the northern boundary (Eq. (20)).

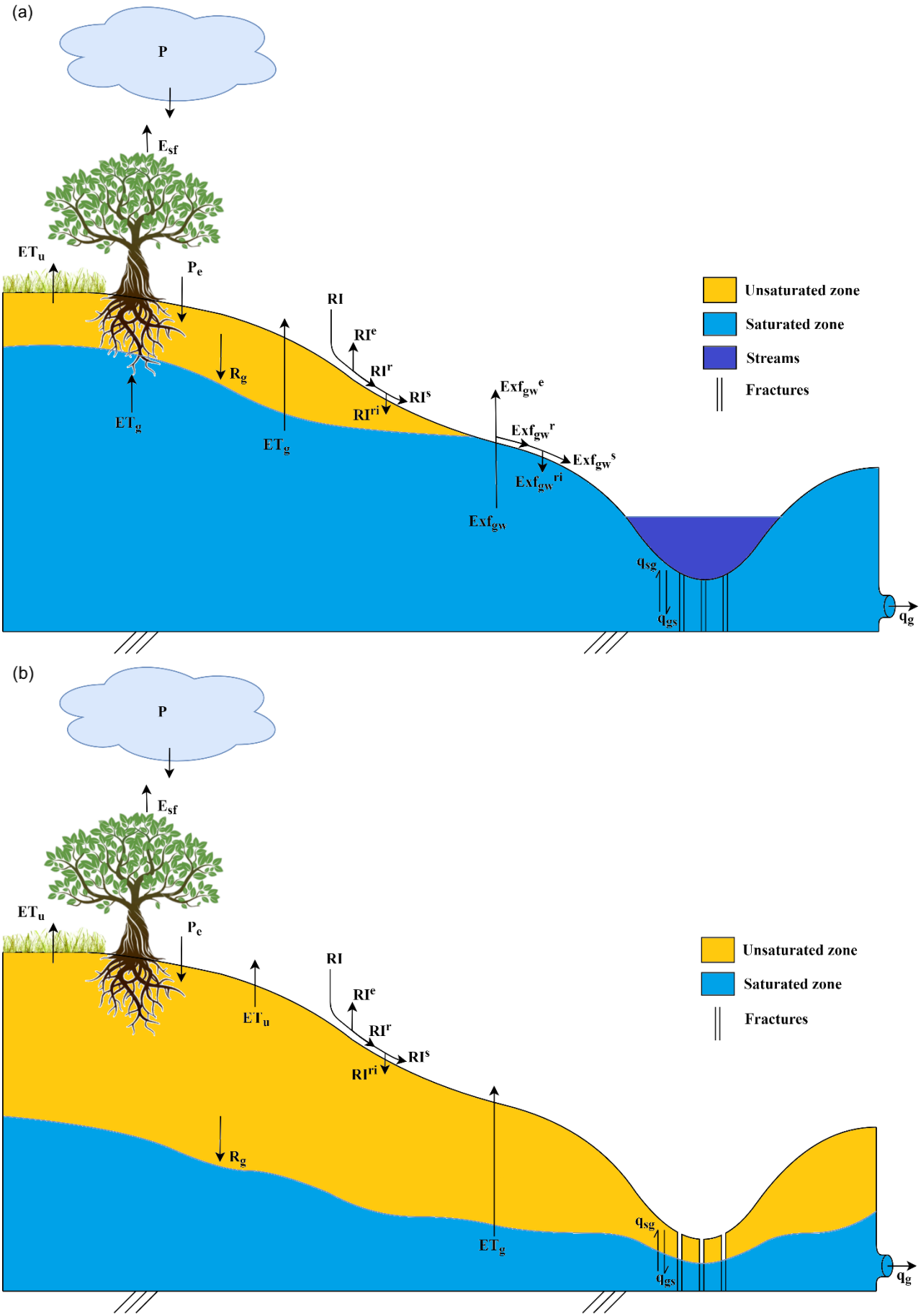

Figure 6: Schematization of the system zones and components: (a) wet season and (b) dry season.

4.4.3. Water Balance Zones and Components

The system consists of two zones, the unsaturated zone and the groundwater zone. The effect of the land surface forces was expressed as inputs to the unsaturated zone. The catchment total water balance can be represented as:

$$P = ET + q + q_g \pm \Delta S \quad (20)$$

where:

P	Precipitation
ET	Total evapotranspiration
q	Total streams discharge at the catchment outlet
q_g	Lateral groundwater outflow at the catchment outlet
ΔS	Total catchment storage = $\Delta S_u + \Delta S_g$

Total evapotranspiration and total streams discharge can be expressed as:

$$ET = E_{sf} + ET_u + ET_g + RI^e + Exf_{gw}^e \quad (21)$$

$$q = (RI^s + Exf_{gw}^s) + q_B \quad (22)$$

$$q_B = q_{gs} - q_{sg} \quad (23)$$

where:

E_{sf}	Evaporated canopy interception
ET_u	Unsaturated zone evapotranspiration
ET_g	Groundwater evapotranspiration
RI^e	Evaporated rejected infiltration
RI^s	Rejected infiltration routed to streams
Exf_{gw}^e	Evaporated groundwater exfiltration
Exf_{gw}^s	Groundwater exfiltration routed to streams
q_B	Base flow

The water balance of the land surface and the unsaturated zone can be represented as:

$$P_e + (RI^{ri} + Exf_{gw}^{ri}) = ET_u + R_g + RI \pm \Delta S_u \quad (24)$$

where:

P_e	Effective precipitation (infiltration) = $P - ET_{sf}$
RI	Rejected Infiltration = $RI^e + RI^r$
RI^r	Rejected infiltration routed either to downslope UZF cells or to streams = $RI^{ri} + RI^s$
RI^{ri}	Re-infiltrated rejected infiltration
Exf_{gw}^{ri}	Re-infiltrated groundwater exfiltration
R_g	Gross groundwater recharge
ΔS_u	Unsaturated zone storage

The water balance of the groundwater zone can be represented as:

$$R_g + q_{sg} = Exf_{gw} + ET_g + q_{gs} + q_g \pm \Delta S_g \quad (25)$$

where:

q_{sg}	Streams leakage to groundwater
q_{gs}	Groundwater leakage to streams
Exf_{gw}	Groundwater exfiltration = $Exf_{gw}^e + Exf_{gw}^r$
Exf_{gw}^r	Groundwater exfiltration routed either to downslope UZF cells or to streams = $Exf_{gw}^{ri} + Exf_{gw}^s$
ΔS_g	Groundwater zone storage

The net groundwater recharge R_n is defined as $R_n = R_g - Exf_{gw} - ET_g$ (26)

4.4.4. Aquifer Geometry

The definition of the aquifer layers by Francés et al. (2014) was applied in this study. They followed the general 3D geological conceptual model of granite aquifers to apply for the Sardon area. This general conceptual model defined from top to bottom the following layers: (1) the laterite layer; can be absent due to erosion, (2) the saprolite layer, (3) the fissured layer and (4) the fresh basement, more details about these layers can be found in Dewandel et al. (2006). They used a combination of different data sources to define a spatial distribution of these layers in the Sardon area. Their results showed two aquifer layers, the saprolite layer and the fissured layer, which match with the framework of Lubczynski & Gurwin (2005) (section 2.6 and Figure 3). Additionally, they defined six internal uniform zones in the saprolite and the fissured layers with the determination of their hydrological and storage parameters (Figure 7). Each layer represents a hydrostratigraphic unit with one value for each flow and storage parameter. Figure 8 shows a 3D spatial representation of the aquifer hydrostratigraphic units and the outcrop areas where the saprolite layer is absent.

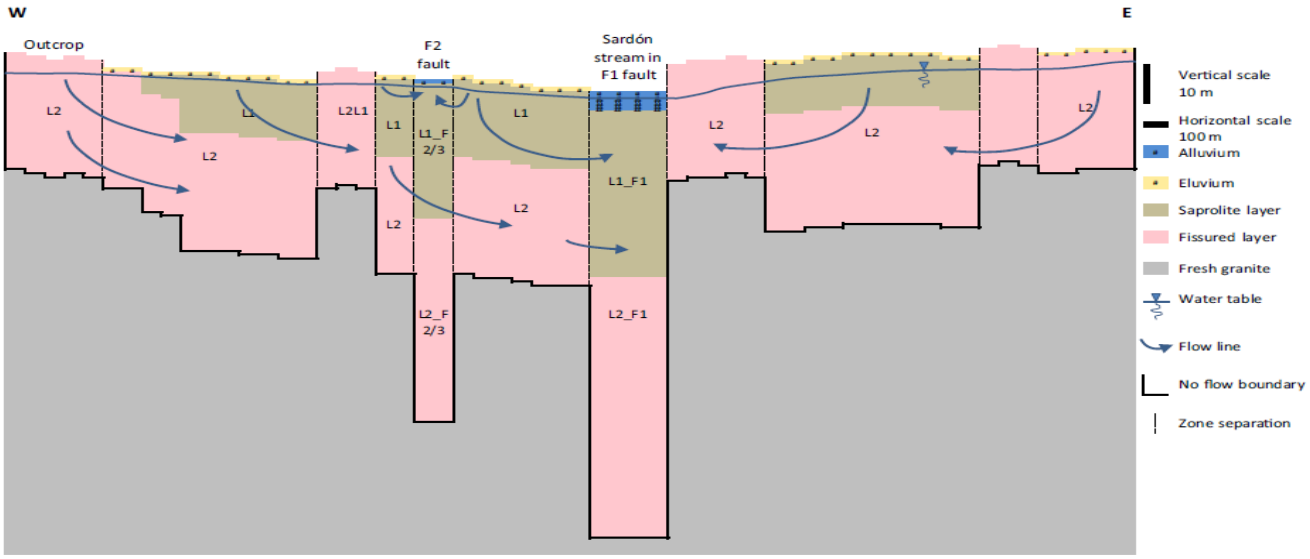

Figure 7: Schematic cross-section (Francés et al., 2014).

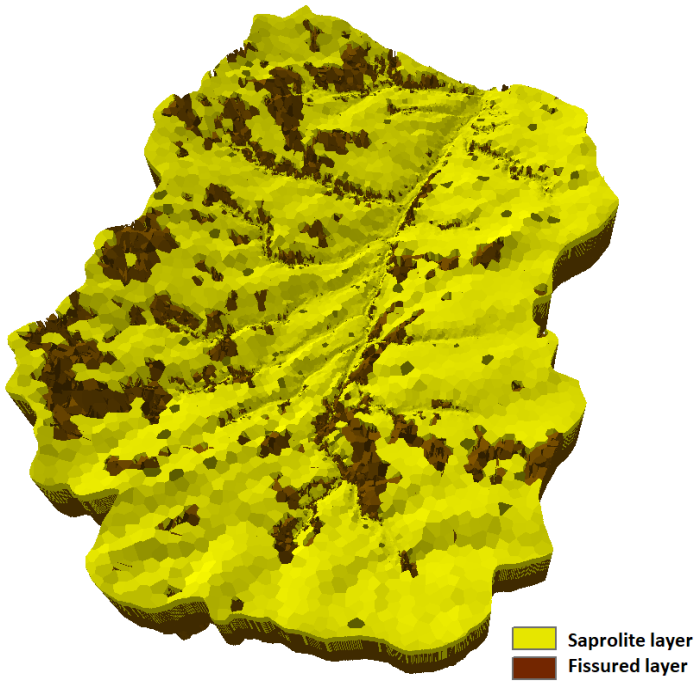

Figure 8: Aquifer hydrostratigraphic units.

4.5. Numerical Model

MODFLOW 6 is the latest version of the numerical code MODFLOW that is used in this research. The option of the Newton Raphson formulation which is the core of MODFLOW-NWT was activated to handle the system nonlinearity.

4.5.1. Software Interface Selection

For data preparation and manipulation, MODFLOW 6 is supported by the open source software, ModelMuse and FloPy. ModelMuse is a graphical user interface (GUI) for different versions of MODFLOW, including MODFLOW 6. A GUI provides a level of ease and intuitiveness that is much greater than direct manipulation of the input files and therefore became the standard for the construction of groundwater numerical models (Bakker et al., 2016). FloPy is the name of a Python script which was developed by Bakker et al. (2016) for groundwater models such as MODFLOW, MT3D, MODPATH and SEAWAT. FloPy has many packages to facilitate the model development including packages for plotting, array manipulation, optimization and data analysis. FloPy does not have a GUI which leads to more effort needed to set up a groundwater model. However, the main advantage of FloPy is that it supports all the MODFLOW capabilities, including the packages that are not implemented in the standard software versions with GUI. For example, the spatial discretization in MODFLOW 6 can be defined by one of three different packages, DIS (structured discretization), DISV (discretization by vertices) and DISU (unstructured discretization). The latter cannot be used in ModelMuse and only works within FloPy. Furthermore, ModelMuse supports only two types of DISV, namely the traditional rectangular and the rectangular quadtree-refined grid (Winston, 2019), unlike FloPy which supports any types of grid such as triangular, rectangular, rectangular quadtree and irregular grids. In this research, FloPy was used for setting up the numerical model.

4.5.2. Spatial Discretization

4.5.2.1. Grid Type Selection

The two discretization packages; DISV and DISU can be used for creating an unstructured grid (Langevin et al., 2017). The DISV package is layer-based which the user defines the grid using a list of (x, y) vertices and the number of layers. The list of the vertices is for creating the grid cells in the horizontal plan; then the cells are grouped into vertical layers. The DISU package is not layer-based, and the user needs to define for each cell the connected cells both in vertical and horizontal directions and the connection properties, and that's why the DISU is considered to be the most flexible of the three discretization packages. In this research, the DISU is not needed as the aquifer has only two layers with clear boundaries and connections, and therefore, the DISV package was used to create the model grid.

The DISV package can work with different types of unstructured grid such as triangular nested, rectangular quadtree, rectangular nested, Voronoi and irregular grids. Not all these grid types achieve the CVFD connection requirements where a line drawn between the centers of any two connected cells should first intersect the shared face at a right angle and second bisect the shared edge between these two cells (Panday et al., 2013; Langevin et al., 2017). The closer the grid honours the CVFD requirements, the smaller the loss in accuracy in the groundwater flow solution. Hesch (2014) had compared the Voronoi grid (VGrid) with the quadtree grid (QGrid), highlighting their similarities and differences as:

Similarities

- Both can handle complicated geometries and boundaries with ease.
- Both provide higher than rectangular grid resolution at the areas of interest such as wells, rivers or other features.
- Both provide higher accuracy for groundwater flow calculations and better model convergence than MODFLOW-2005.

Differences

- VGrid closely honours the CVFD requirements, especially if the difference between the area of the connected cells is small, while the QGrid does not achieve the CVFD requirements which result in errors in the simulated heads and flows.
- The need to use the Ghost Node Correction (GNC) package is essential with the QGrid to correct for simulation errors comparing to the VGrid.

In this study area, the hydrological features that need higher grid resolution are the Sardon streams. They are hydraulically connected with the groundwater and assigning smaller grid cells around those streams can provide better simulation for the surface-groundwater interaction and higher accuracy for the system solution. The streams are irregular, which adds difficulty to fully represent them with any grid type. The VGRID is more flexible to follow the curvature of the streams than any other unstructured grid, including the QGRID. Besides, the VGRID has the advantage of more closely honouring the CVFD requirements, as concluded by Hesch (2014). As a result, the VGrid is more reliable than other unstructured grid for this study area, and it was selected to build the model grid with considering small area difference between the connected cells in the grid implementation steps.

4.5.2.2. Grid Implementation

One of the well-known options to build a Voronoi grid is to use the Delaunay triangulation. A Delaunay triangle is created from a set of three points connected to make only one proper circle (Figure 9). The Voronoi grid is dual to the Delaunay triangulation, where each vertex of the triangles is a node generator for a Voronoi cell (Figure 10).

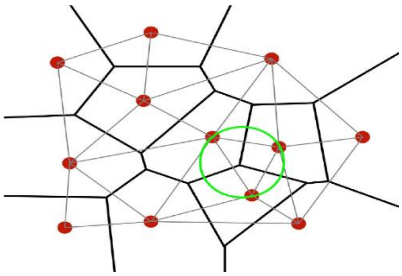

Figure 9: Delaunay triangles and Voronoi cells (https://stackoverflow.com/questions/42047077/voronoi-site-points-from-delaunay-triangulation)

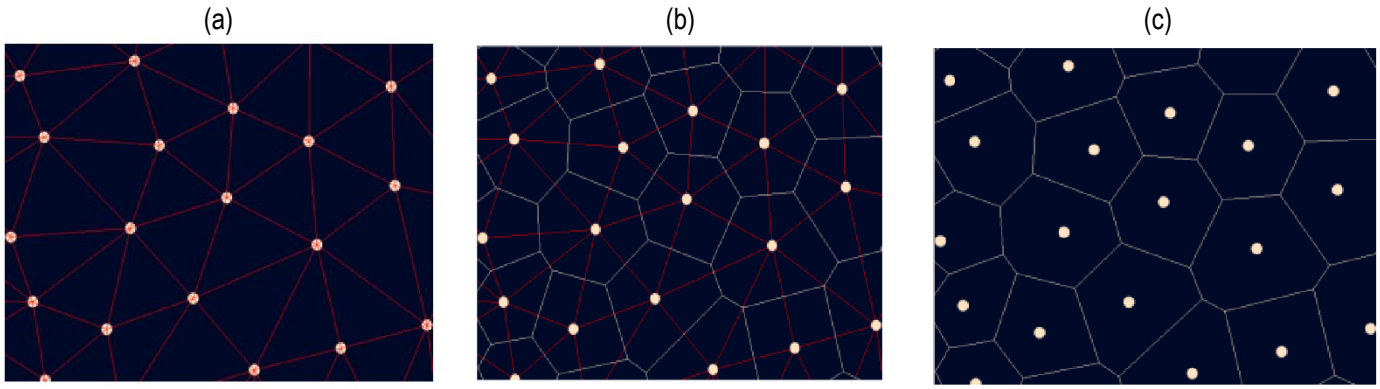

Figure 10: Concept of Voronoi grid creation: (a) Delaunay triangles mesh; (b) Relationship between Delaunay triangles and Voronoi cells (each triangle's vertex is a node for a Voronoi cell); and (c) Voronoi grid (Vandermolen, n.d.).

So, a Delaunay triangle mesh was needed first, which was converted to a Voronoi grid. FloPy provides a module to build a Delaunay triangle mesh while a well-known Python library named SciPy had a module to build the Voronoi grid. The whole process of the Voronoi grid implementation needs an algorithm which was developed using Python language. In this study, a combination of FloPy, Python and ArcGIS was used to build the Voronoi grid. The following steps summarize the main concept of building the Voronoi grid:

- First, a conceptual model needs to be defined, mainly to define the lateral grid boundary (catchment boundaries) and the grid cell locations representing the stream-sections interacting with groundwater; these cells should have substantially smaller size.
- A group of transition zones (buffer zones) were defined around the streams in such a way that the smallest cells are around the streams and further away from the streams, the grid cells become larger.
- The created conceptual model was introduced to the module named "triangle" in FloPy to create a Delaunay triangle mesh.
- The vertices of the created Delaunay triangles, which act as the node generators for the Voronoi cells were introduced to a module named "spatial" in the SciPy Python library to create the Voronoi grid (Figure 11)
- Further steps were accomplished (not discussed here) to mask the grid, define the grid properties (cells, vertices and their connections) and export the grid properties into a format that is readable by the DISV package in MODFLOW 6.
- The total cells number per layer is 23302, with smallest cell width ~15-20 m and biggest cell width ~200 m.

The grid was vertically discretized using the DISV package by defining the number of the model layers, the top and bottom elevations of each grid cell. For each grid cell in layer one, the top elevation (Top_1) was retrieved from the 5 m-resolution digital elevation model of the Spanish Centro Nacional de Informacíon Geográfica (www.cnig.es). Then, the bottom elevation Bot_1 was calculated by subtracting the top elevation from the layer thickness (th_1), ($Bot_1 = Top_1 - th_1$). The layer thickness of both layers was retrieved from Francés et al. (2014) as described in section 4.4.4. For grid cells in layer two, the top elevation (Top_2) is equal to the bottom elevation of the connected upper cell (Bot_1), and the layer thickness of layer two (th_2) was used to calculate the bottom elevation ($Bot_2 = Top_2 - th_2$).

For outcrops cells where layer 1 is absent (Figure 8), the option "IDOMAIN" in the DISV package was used to exclude these cells from the model solution.

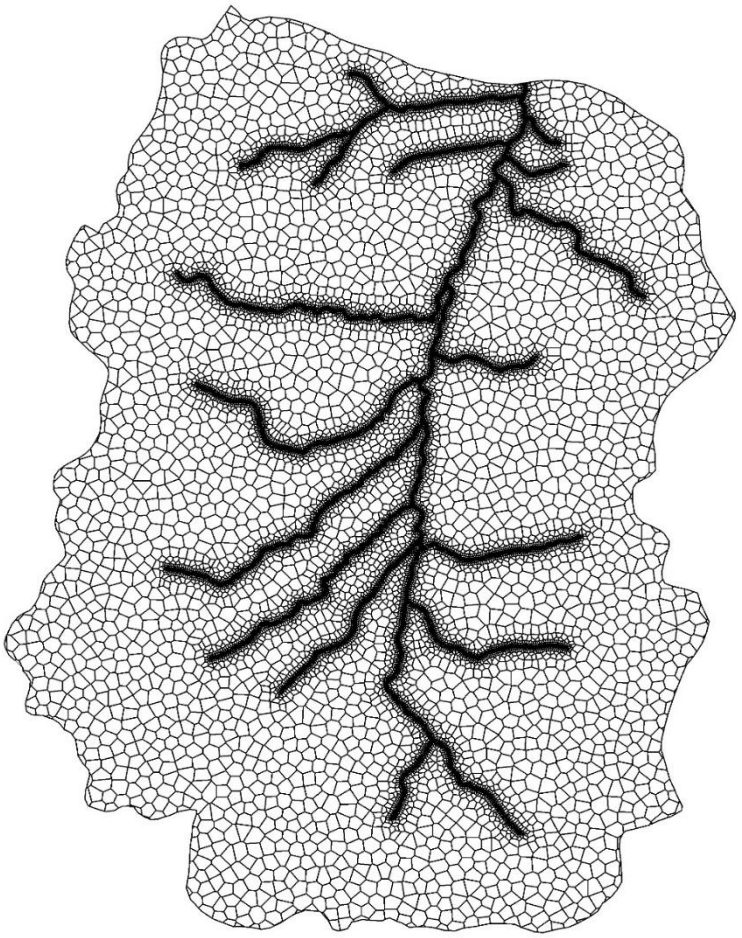

Figure 11: Model grid.

4.5.3. Temporal Discretization

A steady-state model and a transient model were created (sections 4.5.8.2 and 4.5.8.3). The steady-state model does not consider the time in the solution, and therefore, the temporal discretization is not needed. For the transient model, the actual simulated period was 7 years, with 2557 stress periods. The length of each stress period was 1 day to make

good use of the calculated daily driving forces and each stress period consists of only one time step. Prior to the actual period, one year was assigned as a spin-up period (section 4.5.8.3) with 365 stress periods; each stress period has a length of 1 day with only one time step. By summing the spin-up period to the actual period, the total simulation period becomes 8 years (1 spin-up year + 7 actual years) with a total number of 2922 of stress periods.

4.5.4. Hydraulic and Storage Parameters

In the model, the hydraulic parameters control the unsaturated and the saturated flow. The unsaturated hydraulic parameters are defined separately in the UZF package (section 4.5.5.2), while the saturated parameters, including the hydraulic conductivity of the aquifer layers, are defined in the node property flow package (NPF package). The hydraulic conductivity in the horizontal direction (K_h) for both layers were assumed as 0.5 m.day^{-1} as an initial value. For the vertical hydraulic conductivity (K_v), Maréchal et al. (2003) had concluded that K_h is 2 to 30 times higher than K_v based on pumping tests analysis in a fissured layer of a hard rock aquifer. K_v was assumed to be in the range of 10 of K_h and a value of 0.05 m.day^{-1} was used as an initial value. Both K_h and K_v were later adjusted during the calibration by using a group of K-zones for each layer separately.

The storage parameters including the specific storage (S_s) and the specific yield (S_y), are defined in the storage package (STO package), and were assumed as 10^{-5} m^{-1} and 0.05, respectively for both layers. Both S_s and S_y were later adjusted during the calibration by using a group of zones for each layer separately.

4.5.5. Boundary Conditions

The boundary conditions of the system are categorized into internal and external boundaries. The internal boundaries include the UZF, SFR and MVR packages which are responsible for the flow between the system components. The external boundaries describe how the flow goes in or out of the system.

4.5.5.1. External Boundaries

The watershed divide that surrounds the whole catchment except at the Sardon river outlet was assigned as no-flow boundary. The Sardon river outlet area located at the northern boundary acts as a lateral groundwater outflow and were represented in the model by a head-dependent boundary using the drain package (DRN). All the model cells that are located in the outlet area were assigned as drain cells. The DRN package removes the water from the aquifer based on the drain conductance and the difference between the drain elevation and the head in the aquifer as shown

$$Q_{out} = cond * (h_{aq} - h_{drn}) \quad (27)$$

$$cond = K_d * A_{\perp} / b_d \quad (28)$$

where:

Q_{out}	Flow from the aquifer to the drain	[m^3.day^{-1}]
h_{aq}	Aquifer head in the cell that contains the drain	[m]
h_{drn}	Drain elevation	[m]
$cond$	Drain conductance	[m^2.day^{-1}]
K_d	Hydraulic conductivity of the drain's bed	[m.day^{-1}]
$A_{\perp}$	Flow perpendicular area = cell thickness * cell width	[m^2]
b_d	Drain bed thickness	[m]

The h_{drn}, K_d and b were assigned as 733 m, 0.05 m.day^{-1} and 0.6 m, respectively. K_d were adjusted during the calibration as dependant on the K_v of the matching cells.

4.5.5.2. UZF Package

UZF package is the package used to simulate the flow through the unsaturated zone and add the simulated flow to the groundwater zone. The UZF package simulates only the vertical unsaturated flow using the kinematic wave approximation to Richard's equation and solved by the method of characteristics (Niswonger et al., 2006). The simplified form of Richard's equation with the kinematic wave approximation and neglecting the negative pressure gradients can be written in length (L) and time (T) units as

$$\frac{\delta\theta}{\delta t} + \frac{\delta K(\theta)}{\delta z} + i_{ET} = 0 \tag{29}$$

where:

θ	Volumetric water content	($L^3.L^{-3}$)
t	Time	(T)
$K(\theta)$	Vertical unsaturated hydraulic conductivity as a function of water content	($L.T^{-1}$)
z	Distance in the vertical direction	(L)
i_{ET}	Unsaturated evapotranspiration rate per unit depth	($L.T^{-1}.L^{-1}$)

The land surface driving forces are introduced to the UZF package as inputs (infiltration rate and potential evapotranspiration rate), and both applied at the surface. Infiltration rate is the amount of water per surface area per time that percolates into the soil. In the UZF package, the Brooks-Corey equation is used to relate the vertical hydraulic conductivity to the water content (Eq. (30)). Then, the Brooks-Corey equation is formulated to relate the infiltration rate to the water content (Eq. (31)). If the user-specified infiltration rate exceeds K_{sat}, the corresponding water content (θ_{qa}) is set to θ_{sat} and the difference ($q_a - K_{sat}$) is multiplied by the cell area and can be added to another package using the Mover package (section 4.5.5.4).

$$K(\theta) = K_{sat} * \left[\frac{\theta - \theta_{resid}}{\theta_{sat} - \theta_{resid}}\right]^{\varepsilon} \tag{30}$$

$$\begin{aligned} \theta_{qa} &= \left[\frac{q_a}{K_{sat}}\right]^{1/\varepsilon} * (\theta_{sat} - \theta_{resid}) + \theta_{resid} \qquad 0 < q_a \leq K_{sat} \\ \theta_{qa} &= \theta_{sat} \qquad\qquad\qquad\qquad\qquad\qquad\qquad\quad q_a > K_{sat} \end{aligned} \tag{31}$$

where:

K_{sat}	Saturated vertical hydraulic conductivity	($L.T^{-1}$)
θ_{qa}	Corresponding water content to the specified infiltration rate	($L^3.L^{-3}$)
θ_{sat}	Saturated water content	($L^3.L^{-3}$)
θ_{resid}	Residual water content	($L^3.L^{-3}$)
q_a	Infiltration rate	($L.T^{-1}$)
ε	Brooks-Corey exponent	(-)

For the potential evapotranspiration rate (PET), the UZF package first satisfies PET by removing the water from the unsaturated zone. If PET is not satisfied yet, and the water table level is above the extinction depth (d_{ext}), the residual PET will be taken from the groundwater. PET is specified as a rate of (length/time), then it is internally divided by the d_{ext} and added to Equation (29).

Furthermore, the groundwater exfiltration can be simulated within the UZF package by defining a depth called the surface depth (d_{surf}). d_{surf} is a user-specified depth relative to the land surface where the groundwater exfiltration starts. More details about the UZF package can be found in Langevin et al. (2017).

In this study, the infiltration rate is the effective precipitation (precipitation – interception), which was calculated before in section 4.3.1. The precipitation does not change spatially, while the interception changes with space according to the six

defined landcover classes (sections 2.4 and 4.3.1.2). Therefore, for each grid cell, the infiltration rate was calculated based on the concept of the area-weighted average as

$$q_a = P - [(E_{sf_1} * a_1) + (E_{sf_2} * a_2) + (E_{sf_3} * a_3) + (E_{sf_4} * a_4) + (E_{sf_5} * a_5) + (E_{sf_6} * a_6)] \quad (32)$$

where:

q_a	Infiltration rate	[m.day^{-1}]
P	Precipitation	[m.day^{-1}]
$E_{sf_1}, E_{sf_2}, E_{sf_3}, E_{sf_4}, E_{sf_5}, E_{sf_6}$	Interception rate for each landcover class respectively (grass \ bare soil, outcrops, *Q.ilex* on soil, *Q.pyrenaica* on soil, *Q.ilex* on outcrops and *Q.pyrenaica* on outcrops), note: $E_{sf_2} = 0,\ E_{sf_3} = E_{sf_5}\ and\ E_{sf_4} = E_{sf_6}$	[m.day^{-1}]
$a_1, a_2, a_3, a_4, a_5, a_6$	Percentage of the coverage area by each landcover class over the total cell area	[m^2.m^{-2}]

The soil parameters, $K_{sat}, \theta_{sat}, \theta_{resid}$ and ε were assumed as 0.05 m.day^{-1}, 0.4 m^3.m^{-3}, 0.05 m^3.m^{-3} and 3.5 respectively, and were later adjusted during the calibration. K_{sat} was adjusted as dependant on the K_v of the matching cells. For the initial conditions of the water content, the initial water content (θ_i) was assumed as 0.15 m^3.m^{-3}.

For the PET, the main inputs needed in the UZF package are PET rates, extinction depth (d_{ext}) and extinction water content (θ_{ext}). PET rates were calculated before in section 4.3.2 for each landcover class. The d_{ext} for the landcover classes (grass \ bare soil and outcrops) were assumed as 1 m and 0.5 m respectively, while the d_{ext} for the two tree species (*Q.ilex* and *Q.pyrenaica)* were assigned as 3.7 m based on the tables founded in Canadell et al. (1996). The concept of the area-weighted average was used again for each grid cell to have only one value for PET and d_{ext} (Eqs. (33), (34)). θ_{ext} were assigned as 0.05 m^3.m^{-3} and was later adjusted during the calibration, if needed. Equations (32) and (33) were used for each stress period to calculate the new rates for the infiltration and PET.

$$PET = [(PET_1 * a_1) + (PET_2 * a_2) + (PET_3 * a_3) + (PET_4 * a_4) + (PET_5 * a_5) + (PET_6 * a_6)] \quad (33)$$

$$d_{ext} = [(d_{ext1} * a_1) + (d_{ext2} * a_2) + (d_{ext3} * a_3) + (d_{ext4} * a_4) + (d_{ext5} * a_5) + (d_{ext6} * a_6)] \quad (34)$$

where:

$PET_1, PET_2, PET_3, PET_4, PET_5, PET_6$	PET rate for each landcover class respectively (grass \ bare soil, outcrops, *Q.ilex* on soil, *Q.pyrenaica* on soil, *Q.ilex* on outcrops and *Q.pyrenaica* on outcrops)	[m.day^{-1}]
$d_{ext1}, d_{ext2}, d_{ext3}, d_{ext4}, d_{ext5}, d_{ext6}$	Extinction depth for each landcover class respectively, note: $d_{ext} = 1,\ d_{ext2} = 0.5,\ d_{ext3} = d_{ext4} = d_{ext5} = d_{ext6} = 3.7m$	[m]
$a_1, a_2, a_3, a_4, a_5, a_6$	Percentage of the coverage area by each landcover class over the total cell area	[m^2.m^{-2}]

For the groundwater exfiltration, the d_{surf} were assumed as 0.25 m and later adjusted during the calibration.

4.5.5.3. SFR Package

SFR package is the streamflow routing package which simulates the flow interaction between the streams and the groundwater. In SFR package for MODFLOW 6 (SFR6), the flow is translated from the streams to the water table directly without delay and the leakage rate does not exceed the saturated hydraulic conductivity of the unsaturated zone beneath the streambed. SFR6 calculates the flow across the stream beds using one of two options, either by the active reaches option or the simple routing reaches option. The active reaches option use user-specified streamflow to calculate the stream depth using Manning's equation while the simple routing option calculates the stream depth based on a user-specified stream stage (Langevin et al., 2017). One major difference of the SFR6 than the previous version of SFR package (SFR2) is that the unsaturated zone beneath the stream reaches cannot be simulated (Langevin et al., 2017; Niswonger & Prudic, 2005). Hence, for cases of rejected infiltration rates in the UZF cells, these rejected infiltrations cannot be moved directly to the streams within the SFR6 package, and another package (MVR package) is used for this purpose (section 4.5.5.4).

In this study, the Sardon river and its tributaries were all defined as SFR reaches. As it was mentioned before (section 4.5.2.2), the grid cells that contain the streams have the smallest area in order to have more accuracy for the head and flow calculations around the streams. The Sardon river was split into reaches in such a way that only one reach is assigned to one grid cell and the same idea for the Sardon tributaries. The main information needed in the SFR6 package is the streams' properties, streams' connection and the option to calculate the stream depth (active option or simple routing option). More details about the SFR6 package can be found in Langevin et al. (2017).

The data needed for the streams' properties are the streams' length, width, slope, Manning coefficient, bed level and bed hydraulic conductivity. The streams' length and slope were calculated using ArcGIS software, while the streams' width was assumed as 10 m for the Sardon river and 5m for its tributaries based on the fieldwork observations. Manning coefficient was assumed as 0.035 for all the stream reaches. The bed level was calculated based on (bed level = top level of the grid cell that contains the stream reach – stream thickness). The streams' thickness was assumed as 2 m for the Sardon river and 1 m for the Sardon tributaries based on the fieldwork observations. The streams' bed hydraulic conductivity (K_b) was assumed as 0.05 m.day^{-1} as an initial value and was adjusted during the calibration as dependant on the K_v of the matching cells that contain the streams.

The connection of the streams was defined based on the elevations of the Sardon river and its tributaries. All the tributaries have a higher elevation than the Sardon river, and therefore, for each tributary, the end of the tributary was defined as upstream and the connecting point between the tributary and the Sardon river was downstream. For the Sardon river, the elevations are higher in the south than the north and therefore, the river was defined from the south as upstream till the outlet point in the northern boundary as downstream.

The flow between the stream reaches and the aquifer cells is computed by Darcy's law (Eq. (35)). For the streams' depth, the active reaches option which uses Manning's equation (with the assumption of wide rectangular reaches) was selected (Eqs. (37), (38)). The stream discharge for each reach (q) is calculated per stress period and equals to the sum of the UZF package's sources (rejected infiltration (RI^s) and groundwater exfiltration (Exf_{gw}^s) that are routed to streams) and the base flow ($q_{B} = q_{gs} - q_{sg}$) as shown in Equation (36). Then, the calculated (q) is substituted in Equation (38) to get the stream's depth for each reach per every stress period.

$$q_{gs} = \frac{K_b * W_b * L_b}{b_b} * (h_{aq} - h_b) \quad \text{if } h_{aq} > h_b$$
$$q_{sg} = \frac{K_b * W_b * L_b}{b_b} * (h_b - h_{aq}) \quad \text{if } h_{aq} < h_b \qquad (35)$$

$$q = RI^s + Exf_{gw}^s + q_{gs} - q_{sg} \qquad (36)$$

$$q = {C_u}/{n_b} * W_b * {d_b}^{5/3} * {S_o}^{1/2} \qquad (37)$$

$$d_b = \left[\frac{q * n_b}{C_u * W_s * {S_o}^{1/2}}\right]^{3/5} \qquad (38)$$

where:

q_{gs}	Groundwater leakage to stream reach	[m^3.day^{-1}]
q_{sg}	Stream reach leakage to groundwater	[m^3.day^{-1}]
q	Calculated stream discharge	[m^3.day^{-1}]
RI^s	Rejected infiltration routed to stream reach	[m^3.day^{-1}]
Exf_{gw}^s	Groundwater exfiltration routed to stream reach	[m^3.day^{-1}]
h_{aq}	Aquifer head in the cell that contains the stream reach	[m]
h_b	Stage of stream reach	[m]
K_b	Hydraulic conductivity of stream reach's bed	[m.day^{-1}]
W_b	Width of stream reach	[m]

L_b	Length of stream reach	[m]
b_b	Bed thickness of stream reach	[m]
d_b	Water depth of stream reach	[m]
n_b	Manning coefficient of stream reach	[day.m^{-3}]
S_o	Slope of stream reach	[m^1.m^{-1}]
C_u	Conversion coefficient = 86400 for flow units of m^3.day^{-1}	[-]

4.5.5.4. MVR Package

MVR is a new water mover package designed in MODFLOW 6 to move the water from a feature in one package as a provider to a feature in another package as a receiver. The available water is moved from the provider package to the MVR package and from the MVR package to the receiver package based on the user request. All the stress packages (WEL, DRN, RIV and GHB) and the advanced stress packages (MAW, SFR, LAKE and UZF) can be providers, but only the advanced stress packages which solve the continuity equation can be receivers. The MVR package provides four options to define how much available water will be moved from the provider package to the receiver package. More details about how the MVR package works can be found in Langevin et al. (2017).

In this study, the MVR was used to simulate the overland flow and to apply the re-infiltration concept. The MVR package allowed the transferring of the available water (rejected infiltration and groundwater exfiltration rates) from the provider (upslope UZF cells) to the receivers (either to the downslope neighbouring UZF cells representing re-infiltrated water (RI^{ri} and Exf_{gw}^{ri}), or to the SFR reaches representing overland flow (RI^{s} and Exf_{gw}^{s})).

The re-infiltration concept is to add the rejected components ($RI + Exf_{gw}$) from the fully saturated zones to the unsaturated zones, where the soil is not saturated yet. This re-infiltration concept is applied by cascading the rejected components of a particular UZF cell (UZF provider feature) among its down-slope neighbouring UZF cells (UZF receiver features) using the FACTOR option in the MVR package. However, there is no automatic way in MODFLOW 6 to define the mover fractions (FACTORs) between the UZF provider to the UZF receivers. In principle, the mover fractions should be calculated based on the slopes between the cells and the land surface characteristics (surface roughness) of the cells, the latter is not considered in any of the following described concepts. The multi-flow direction (MFD) is a raster-based algorithm, which partitions the flow among the downslope neighbouring pixels based on the land surface gradient (Quinn et al., 1991). The MVD concept is used in many hydrological models and applied in many GIS applications such as the “flow direction” tool in ArcGIS software (based on the MFD adaptive approach introduced by Qin et al. (2007)). Additionally, similar concepts of the MFD were applied for grid-based models such as the cascade routing tool (CRT) of the numerical code (GSFLOW), but with a slight difference between the two concepts’ equations. The CRT defines cascading flow for surface and shallow subsurface flow paths and is applied to rectangular grid, ignoring the cascading to the diagonal, irregular grid cells (Henson et al., 2013). In contrast, the cascade routing concept (CR) applied in this study, allows for irregular Voronoi grid cells, as shown in Equation (39), but it does not have shallow subsurface flow. However, the applied d_{surf} in the UZF package, allows for subsurface groundwater exfiltration (Exf_{gw}) and therefore, the combination use of (CR + d_{surf}) allows for shallow subsurface flow originated from subsurface Exf_{gw} (only one component of total shallow subsurface flow).

$$\alpha_{i,j} = \frac{S_{i,j}}{\sum_{j=1}^{m} S_{i,j}} \quad (39)$$

$$S_{i,j} = \frac{elv_{i-}\, elv_j}{d_{ij}} \quad (40)$$

where:

$\alpha_{i,j}$	Fraction of flow from the cell i to the neighbouring j cell (ranges from 0 to 1)	[-]
$S_{i,j}$	Slope gradient between cell i and j	[-]
$elv_{i,}\ elv_j$	Land surface elevation of cells i and j respectively	[m]
d_{ij}	Distance between the centres of the connected i and j cells	[m]
m	Number of connected j cells to the cell i	[-]

The fraction between cell i and the connected j cell equals to the slope gradient between the two cells divided by the sum of the slope gradient between cell i and all its jth connected cells (Eq. (39)). The slope gradient equals to the difference between the land surface elevations of cell i and the connected j cell divided by the distance between the centres of the two cells (Eq. (40)). The land surface elevations of the cells were obtained from the 5 m-resolution DEM of the Spanish Centro Nacional de Informacíon Geográfica (www.cnig.es), while the distances between the cell centres were calculated using the ArcGIS software. For any $S_{i,j}$ with a negative value, which means the cell i has lower elevation than the cell j, the $\alpha_{i,j}$ was assigned as zero, no flow occurred between this i- j connection. The maximum $\alpha_{i,j}$ is 1, which occurred when the elevation of the cell i is higher than the elevation of only one connected j cell, representing the single flow direction (SFD). If the sum of $\alpha_{i,j}$ between the cell i and all its jth connected cells is zero, which means that the cell i is a sink cell, no water were moved and this amount of water was considered as evapotranspired water (RI^e and Exf_{gw}^e) and were added to the total evapotranspiration (Eq. (21)).

The $\alpha_{i,j}$ values were assigned in the MVR package using the option FACTOR as shown in Equation (41). A main limitation within the MVR package is that there is no way to separate the rejected infiltration and the groundwater exfiltration when moving to the receivers by assigning different factors.

$$Q_R = \alpha_{i,j} * Q_P \qquad (41)$$
$$Q_R = \alpha_{i,j} * (RI + Exf_{gw})$$

where:

Q_R	Available rate for the receiver package (received rate)	[m^3.day^{-1}]
Q_p	Provided rate: sum of rejected infiltration (RI) and groundwater exfiltration (Exf_{gw})	[m^3.day^{-1}]
$\alpha_{i,j}$	Mover factor = flow fraction between cells i and j	[-]

4.5.6. Observation Package

In IHMs, the state and rate variables are the observations measured in the field so, they are with a relatively high degree of confidence, and therefore can be used for the model calibration and validation. The monitoring network described in section 2.7 includes 14 observation points for groundwater levels (head variables) and one observation for the streamflow at the catchment outlet (flow variable). These observations were introduced to the observation package (OBS) by defining the grid cell that contains the observation point and the type of observation, either head or flow or drawdown. The OBS package for MODFLOW 6 does not require the input of observed values and does not calculate the residual values (difference between observed and calculated values), unlike the previous versions of MODFLOW. The OBS outputs were calculated for each time step and were exported to an external text file for further processing.

4.5.7. Ghost Node Package

Ghost node package (GNC) is the package needed to correct for errors in simulated heads and flow in cases of using a grid that violate the CVFD connection requirements (Panday et al., 2013). As it was mentioned in section 4.5.2.1, the VGrid was selected in this study because it closely honours the CVFD requirements, especially if the difference between the area of the connected cells is small and this was already considered in the grid implementation steps. However, in the solution, there might be still minor errors generated as the VGrid does not fully achieve the CVFD requirements. In order to ensure higher accuracy for the groundwater solution, the GNC package was activated. Later, the GNC was deactivated to test whether the solution is sensitive to it or not (section 4.5.10).

All the grid cells were assigned in the GNC package. For each grid cell (c_n), the needed data are: the connected cell (c_m), the contribution fraction of c_m (α_n), all other neighbouring cells ($\sum c_j$), and their contributing fractions ($\sum \alpha_j = 1 - \alpha_n$), as the example shown in Figure 12. The contributing fractions should be defined based on the distance weighted average between the cell and its neighbours and should be computed by linear interpolation. For simplicity, α_n was assumed as 0.5, so $\sum \alpha_j = 0.5$ and for each c_j, $\alpha_j = \sum \alpha_j / \sum c_j = 0.5 / \sum c_j$. More details about the GNC can be found in Panday et al. (2013) and Langevin et al. (2017).

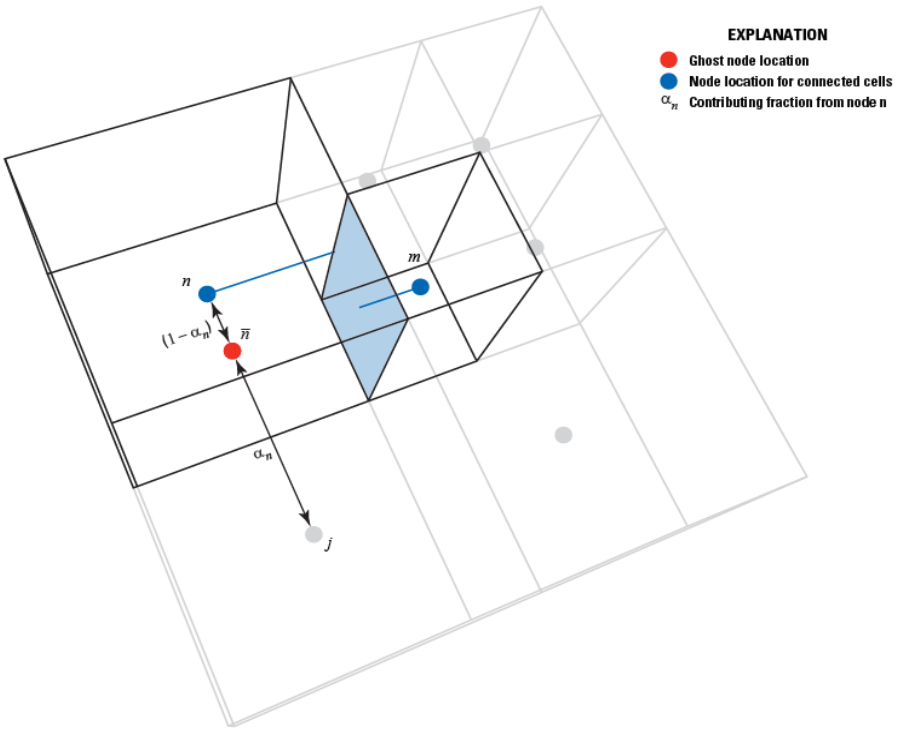

Figure 12: Ghost node example for a nested grid (Langevin et al., 2017).

4.5.8. Model Calibration

Model calibration is to find the optimum system parameters that will produce a satisfactory match between a historical time series of measured values and the model simulated values. The calibration process consists of the following steps:

- Choose calibration targets from available state and rate variables
- Choose calibration parameters
- Run the model using best estimates of model parameters
- Compare the simulated values to the observed values
- Errors' assessment
- Adjust model parameters to best fit the simulated to the observed values based on the errors' assessment.

The calibration targets are the head and flow observations, as described in sections 2.7 and 4.5.6. The calibration parameters can be any model parameters such as horizontal or vertical hydraulic conductivity, storage parameters, boundary conditions, and recharge rates (Anderson et al., 2015). However, the model solution is not equally sensitive to all the model parameters, and the user needs to identify the most valuable parameters for the calibration process. It is quite common in groundwater models to select the horizontal and vertical hydraulic conductivity as the most sensitive parameters that have a large effect on the model solution. In addition, the hydraulic conductivity has a high level of uncertainty and difficulty to measure in the field, In this study, with the use of the advanced stress packages (UZF and SFR), the parameters that highly control the solution were selected as calibration parameters as shown in Table 1.

Table 1: Calibration Parameters

Parameter		Dependency	Initial values		Model package	Described in section
K_h	Horizontal hydraulic conductivity		0.5	[m.day^{-1}]	NPF	4.5.4
K_v	Vertical hydraulic conductivity		0.05	[m.day^{-1}]	NPF	4.5.4

Parameter		Dependency	Initial values		Model package	Described in section
K_{sat}	Vertical saturated hydraulic conductivity	equal to K_v	0.05	[m.day^{-1}]	UZF	4.5.5.2
K_b	Streams' bed hydraulic conductivity	equal to K_v	0.05	[m.day^{-1}]	SFR	4.5.5.3
K_d	Drain's bed hydraulic conductivity	equal to K_v	0.05	[m.day^{-1}]	DRN	4.5.5.1
$cond$	Drain conductance		100	[m^2.day^{-1}]	DRN	4.5.5.1
S_y	Specific yield		0.05	[-]	STO	4.5.4
S_s	Specific storage		10^{-5}	[m^{-1}]	STO	4.5.4
θ_{resid}	Residual water content		0.05	[m^3.m^{-3}]	UZF	4.5.5.2
θ_{sat}	Saturated water content		0.4	[m^3.m^{-3}]	UZF	4.5.5.2
θ_i	Initial water content		0.15	[m^3.m^{-3}]	UZF	4.5.5.2
θ_{ext}	Extinction water content		0.05	[m^3.m^{-3}]	UZF	4.5.5.2
d_{surf}	Surface depth		0.25	[m]	UZF	4.5.5.2

4.5.8.1. Error Assessment

During calibration, the model is assessed based on the graphical and statistical comparison between the simulated values and the observed values to achieve the best fit between them. The graphical comparison can be made by the scatter plots and the residual errors plots. The scatter plot shows observed values versus the simulated values, allows for a quick assessment, and also shows the bias in the calibration (Anderson et al., 2015). The residual error is the difference between the observed value and the simulated value. Residual errors graph is vital in transient models to show the calibration fitting and reflect the system dynamics. The statistical comparison is also necessary to measure the goodness of fit by calculating quantitative summary statistics. The model will have the best fit by finding the optimum parameters that minimize the examples of summary statistics shown in Equations (42), (43), (44), and (45).

$$MAE = \frac{1}{n}\sum_{i=1}^{n}\left|(h_m - h_s)\right|_i \quad (42)$$

$$RMSE = \left[\frac{1}{n}\sum_{i=1}^{n}(h_m - h_s)_i^2\right]^{0.5} \quad (43)$$

$$NSE = 1 - \frac{\sum_{i=1}^{n}\left|(h_m - h_s)\right|_i^2}{\sum_{i=1}^{n}\left|(h_m - \overline{h}_m)\right|_i^2} \quad (44)$$

$$VE = 1 - \frac{\sum_{i=1}^{n}\left|(Q_m - Q_s)\right|_i}{\sum_{i=1}^{n} Q_m} \quad (45)$$

where:

MAE	Mean absolute error
$RMSE$	Root mean square error
NSE	Nash-Sutcliffe coefficient
VE	Volumetric efficiency
h_s	Simulated head
h_m	Observed head
$\overline{h}_m$	Mean of observed head
Q_s	Simulated flow
Q_m	Observed flow
n	Number of records

The criteria to consider whether the model is sufficiently calibrated or not depends on the modelling objective and remains subjective. In this study, for head observations, the model is considered sufficiently calibrated if $MAE \leq 0.8$ m and $RMSE \leq 1$ m. For flow observations, the calibration was evaluated using the VE, a metric for flow observations with a range from 0 for poor fit to 1 for good fit. It is formulated from NSE to overcome the NSE failure to represent useful evaluation when $NSE < 0$ (Criss & Winston, 2008). The model is considered sufficiently calibrated if $VE \geq 0.5$.

4.5.8.2. Steady-State Calibration

A steady-state model represents the average state of an analysed system. Therefore, the Sardon steady-state model was created using the averages of 7 years data, including infiltration rate, PET, streams stage and observed variables. A calibrated steady-state model can be helpful for two purposes: (a) can give the first indication of the calibration parameters for the transient model, and (b) can be used as initial conditions for the spin-up period. In this study, the steady-state calibration was performed for these two purposes.

4.5.8.3. Transient Calibration

A spin-up period is a period assigned prior to the transient model to remove the influence of the initial conditions on the transient simulation. The spin-up period is recommended in cases of transient initial conditions known as dynamic cyclic equilibrium conditions when the system (heads and flows) has a certain cycle that is repeated over time. The spin-up period is to create these transient initial conditions by assigning arbitrary starting heads and running a model with a set of cyclic stresses (e.g., daily or weekly stresses) until the resulting heads come to cyclic equilibrium (Anderson et al., 2015). Then the spin-up period heads are used as initial conditions for the transient model. In this study, the daily stresses of the first year of the transient model (1 October 2007 to 30 September 2008) were duplicated and assigned as an arbitrary spin-up period (number of stress periods = 365 and stress period length = 1 day). The steady-state solution heads were used as starting heads for the spin-up period.

Transient model is created by introducing the temporally variable system stresses to examine the system responses over time. In this study, the transient model has a total period of 8 years, (1 arbitrary spin-up year + 7 actual years from 1 October 2007 to 30 September 2014). The temporal discretization of the transient model was discussed in section 4.5.3. The values of the calibration parameters retrieved from the steady-state calibration were used as first indicators for the transient calibration then were changed manually (trial and error) to minimize the summary statistics and get the best fit of the model.

4.5.9. Model Validation

Model validation is a post-calibration process to verify that the calibrated model is representative of the system and to increase the confidence in the model performance. There are three options to validate the model, either by: (a) using a different set of observation data, (b) using different time periods, or (c) using another dependant variable such as concentrations or temperature (Anderson et al., 2015). However, recently, some groundwater modellers pointed out that the data used in the validation is more valuable to be incorporated into the calibration to reduce non-uniqueness and uncertainty of the calibration (Doherty & Hunt, 2010; Anderson et al., 2015) than to use for validation. They argued that different set of data or different time periods may contain information with different aspects of the modelled system and using this information for validation will not increase the confidence of the model's performance. This opinion was followed in this study, all the data were used in the calibration, and no validation was performed.

4.5.10. Sensitivity Analysis

Sensitivity analysis is to test how the model solution is sensitive to changes in one or more of the calibration parameters. It is determined by selecting one calibration parameter and changing its value incrementally while fixing all other calibration parameters. Then the model runs to show how much it will be out of calibration by changes in the selected parameter. All the calibration parameters mentioned in Table 1 were tested. Additionally, the GNC package was deactivated to show its effect on the model calibration.

5. RESULTS

5.1. Driving Forces

5.1.1. Interception

Table 2 shows the yearly interception rates per landcover class, while Table 3 shows the coverage of each landcover class over the total catchment area. The interception rates of Table 2 were multiplied by the coverage percentages of Table 3, respectively, to get the final yearly interception rates per landcover class (Table 4). It was noticed that the dry years, such as 2009, had higher final interception rate (7.59%) than the wet years, such as 2010 and 2014 (4.70% and 5.22% respectively). This is due to the fact that in dry conditions, the canopy is less saturated and will capture more rainfall compared to wet conditions. The overall final interception rate of the total period (2008-2014) is ~ 6%, relatively low due to the high coverage of the landcover class (grass \ bare soil) which had low interception rates (4.5 to 8.5%).

Table 2: Yearly rates of interception per landcover class

	Estimated as described in section 4.3.1.2		Retrieved from Hassan et al. (2017)			
Year	Grass \ bare soil	Outcrops	*Q.ilex* on soil	*Q.pyrenaica* on soil	*Q.ilex* on outcrops	*Q.pyrenaica* on outcrops
2008	5.73%	0.00%	53.75%	12.66%	53.75%	12.66%
2009	8.40%	0.00%	59.19%	9.23%	59.19%	9.23%
2010	4.55%	0.00%	52.50%	9.01%	52.50%	9.01%
2011	5.72%	0.00%	55.67%	6.43%	55.67%	6.43%
2012	6.84%	0.00%	50.88%	15.97%	50.88%	15.97%
2013	6.19%	0.00%	45.77%	9.76%	45.77%	9.76%
2014	5.23%	0.00%	53.50%	9.56%	53.50%	9.56%

Table 3: Coverage of the landcover classes over the total catchment area

Landcover class	Grass \ bare soil	Outcrops	*Q.ilex* on soil	*Q.pyrenaica* on soil	*Q.ilex* on outcrops	*Q.pyrenaica* on outcrops
Coverage over total catchment area	71.58%	21.50%	1.57%	3.51%	0.34%	1.29%

Table 4: Final yearly interception rates per landcover class over the total catchment area

Year	Precipitation ($mm.yr^{-1}$)	Grass \ bare soil	Outcrops	*Q.ilex* on soil	*Q.pyrenaica* on soil	*Q.ilex* on outcrops	*Q.pyrenaica* on outcrops	Overall rate	Interception ($mm.yr^{-1}$)
2008	542.31	4.10%	0.00%	0.84%	0.44%	0.18%	0.16%	5.74%	31.12
2009	317.22	6.01%	0.00%	0.93%	0.32%	0.20%	0.12%	7.59%	24.07
2010	744.14	3.26%	0.00%	0.82%	0.32%	0.18%	0.12%	4.70%	34.94
2011	440.83	4.09%	0.00%	0.87%	0.23%	0.19%	0.08%	5.47%	24.10
2012	336.54	4.89%	0.00%	0.80%	0.56%	0.17%	0.21%	6.63%	22.19
2013	671.52	4.43%	0.00%	0.72%	0.34%	0.16%	0.13%	5.77%	38.77
2014	725.92	3.74%	0.00%	0.84%	0.34%	0.18%	0.12%	5.22%	37.92

5.1.2. Potential Evapotranspiration ($\boldsymbol{PET}$)

5.1.2.1. Crop Coefficient ($\boldsymbol{K_c}$)

The K_e and K_{cb} were calculated as described in sections 4.3.2.4 and 4.3.2.5. Table 5 and Table 6 show the monthly K_e and K_{cb} values for all the landcover classes, respectively. It was noticed that the K_{cb} values for the Q.ilex were higher than the Q.pyrenaica from November to March as in this period, the Q.pyrenaica is leafless which will transpire less, while from June to September, K_{cb} for Q.pyrenaica is higher than Q.ilex, which match with the results of Reyes-Acosta & Lubczynski (2013). They concluded that in the dry season, the average transpiration rates for Q.pyrenaica (1.19 $mm.day^{-1}$) is larger than Q.ilex (0.83 $mm.day^{-1}$). Finally, K_e and K_{cb} were summed to get the final K_c values for each landcover class, as shown in Table 7 and Figure 13.

Table 5: Monthly K_e values of the landcover classes

Month	Grass \ bare soil	Outcrops	*Q.ilex* on soil	*Q.pyrenaica* on soil	*Q.ilex* on outcrops	*Q.pyrenaica* on outcrops
October 2009	0.14	0.07	0.08	0.07	0.04	0.03
November 2009	0.04	0.02	0.02	0.02	0.01	0.01
December 2009	0.07	0.03	0.04	0.03	0.02	0.02
January 2010	0.06	0.03	0.04	0.03	0.02	0.01
February 2010	0.10	0.05	0.06	0.05	0.03	0.03
March 2010	0.39	0.20	0.24	0.20	0.12	0.10
April 2010	0.39	0.20	0.23	0.20	0.12	0.10
May 2010	0.29	0.14	0.17	0.14	0.09	0.07
June 2010	0.35	0.17	0.21	0.17	0.10	0.09
July 2010	0.33	0.16	0.20	0.16	0.10	0.08
August 2010	0.05	0.03	0.03	0.03	0.02	0.01
September 2010	0.21	0.10	0.12	0.10	0.06	0.05

Table 6: Monthly K_{cb} values of the landcover classes

Month	Grass \ bare soil	Outcrops	*Q.ilex* on soil	*Q.pyrenaica* on soil	*Q.ilex* on outcrops	*Q.pyrenaica* on outcrops
October 2009	0.11	0.06	0.35	0.27	0.35	0.27
November 2009	0.33	0.16	0.60	0.44	0.60	0.44
December 2009	0.41	0.21	0.77	0.54	0.77	0.54
January 2010	0.36	0.18	0.67	0.52	0.67	0.52

Month	Grass \ bare soil	Outcrops	*Q.ilex* on soil	*Q.pyrenaica* on soil	*Q.ilex* on outcrops	*Q.pyrenaica* on outcrops
February 2010	0.52	0.26	0.69	0.61	0.69	0.61
March 2010	0.63	0.31	0.87	0.82	0.87	0.82
April 2010	0.71	0.36	1.04	1.00	1.04	1.00
May 2010	0.64	0.32	0.95	0.95	0.95	0.95
June 2010	0.46	0.23	0.80	0.85	0.80	0.85
July 2010	0.24	0.12	0.54	0.62	0.54	0.62
August 2010	0.02	0.01	0.27	0.38	0.27	0.38
September 2010	0.07	0.03	0.31	0.33	0.31	0.33

Table 7: Monthly K_c values of the landcover classes

Month	Grass \ bare soil	Outcrops	*Q.ilex* on soil	*Q.pyrenaica* on soil	*Q.ilex* on outcrops	*Q.pyrenaica* on outcrops
October 2009	0.25	0.13	0.43	0.34	0.39	0.31
November 2009	0.36	0.18	0.62	0.46	0.61	0.45
December 2009	0.48	0.24	0.81	0.57	0.79	0.56
January 2010	0.42	0.21	0.70	0.55	0.68	0.53
February 2010	0.62	0.31	0.75	0.67	0.72	0.64
March 2010	1.02	0.51	1.11	1.01	0.99	0.92
April 2010	1.10	0.55	1.28	1.20	1.16	1.10
May 2010	0.93	0.46	1.12	1.09	1.04	1.02
June 2010	0.81	0.41	1.01	1.02	0.90	0.94
July 2010	0.57	0.28	0.73	0.78	0.63	0.70
August 2010	0.07	0.04	0.31	0.41	0.29	0.39
September 2010	0.27	0.14	0.43	0.43	0.37	0.38

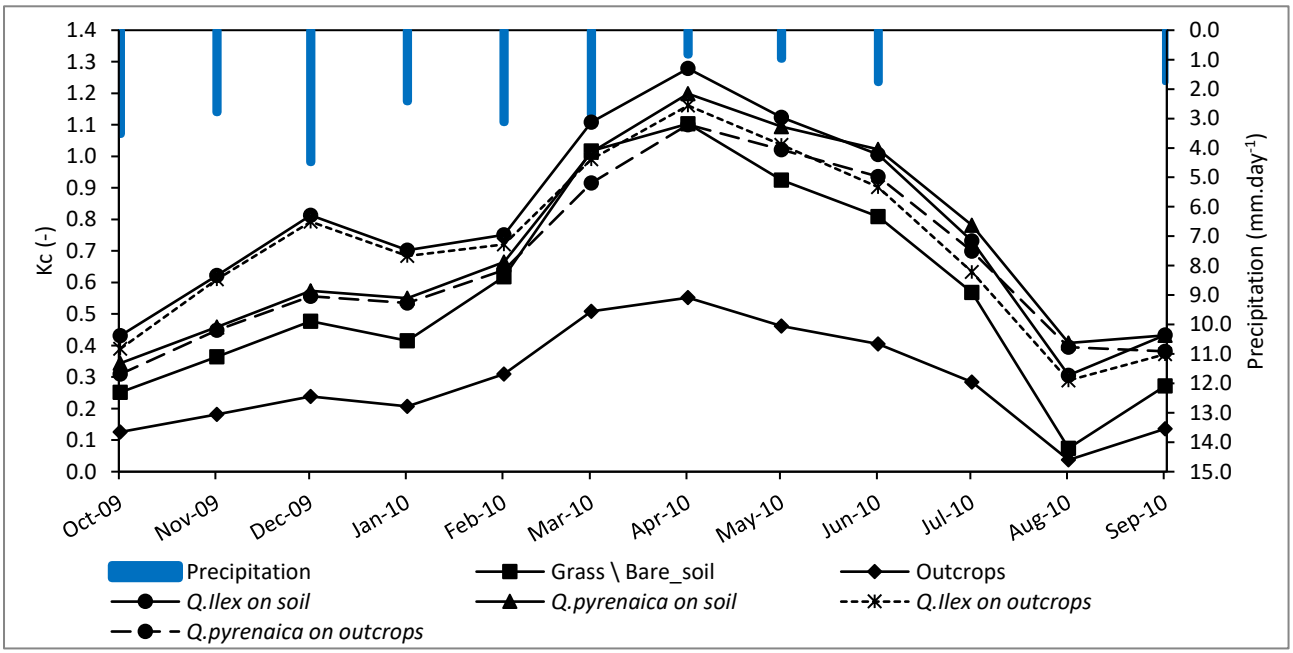

Figure 13: Monthly K_c for different landcover classes.

5.2. Calibration Results

5.2.1. Steady-State Calibration

The distribution of the flow parameters, including the K_h, K_v and K_{sat} were exported from the steady-state calibrated model. These parameters distributions were used as starting values for calibrating the transient model. Also, the steady-state model gave the final values of the unsaturated flow parameters (θ_{resid}, θ_{sat}, θ_{ext} and d_{surf}) which were used in the transient model. However, for cases with complex surface-groundwater interaction or high temporal variability of system dynamics such as this study case, the steady-state solution cannot reflect any useful conclusions, regarding the representation of the system dynamics as it was confirmed by similar studies such as El-Zehairy et al. (2018). The results of the steady-state calibration were not presented herein, due to the text size limitation and limited relevance of the modelling step to present all the results.

5.2.2. Transient Calibration

The transient calibration was the most time-consuming step in this study. For example, one run of the 8-years model took around 12-14 hrs, using a powerful laptop (intel core i7-8th generation processor and 16-gigabit memory). The entire calibration process (waiting for the model run to be finished, comparing the simulated values to the observed values, and checking the errors' assessment) was challenging and time-consuming in this study. Additionally, there was a problem in the current version of MODFLOW (v-mf6.0) to run long transient models due to a UZF memory leakage bug. After contacting the USGS team of MODFLOW 6, they confirmed this problem, and then they provided a new version (v-mf6.1), which fixed this bug and the model ran successfully. The new version is the one expected to be released for public use by the end of 2020, but it was provided to me earlier to be able to run the model and finish this study on time. The results of the transient model calibration are presented in the following sections (5.2.3 to 5.2.5).

5.2.3. Calibrated Parameters

Table 8 shows the range of the calibrated parameters, while Figure 14, Figure 15 and Figure 16 show the spatial distribution of K_h, K_v, S_y and S_s for both layers.

Table 8: Calibrated parameters values

Parameter		Range	Model package	
K_h	Horizontal hydraulic conductivity	0.005 – 0.1	NPF	[m.day^{-1}]
K_v	Vertical hydraulic conductivity	0.0005 – 0.06	NPF	[m.day^{-1}]
K_{sat}	Vertical saturated hydraulic conductivity	0.0005 – 0.06	UZF	[m.day^{-1}]
K_b	Streams' bed hydraulic conductivity	0.0005 – 0.06	SFR	[m.day^{-1}]
K_d	Drain's bed hydraulic conductivity	0.01 – 0.06	DRN	[m.day^{-1}]
$cond$	Drain conductance	1.5 – 460	DRN	[m^2.day^{-1}]
S_y	Specific yield	0.01 – 0.06	STO	[-]
S_s	Specific storage	10^{-6} – 10^{-5}	STO	[m^{-1}]
θ_{resid}	Residual water content	0.05	UZF	[m^3.m^{-3}]
θ_{sat}	Saturated water content	0.4	UZF	[m^3.m^{-3}]
θ_i	Initial water content	0.15	UZF	[m^3.m^{-3}]
θ_{ext}	Extinction water content	0.05	UZF	[m^3.m^{-3}]
d_{surf}	Surface depth	0.25	UZF	[m]

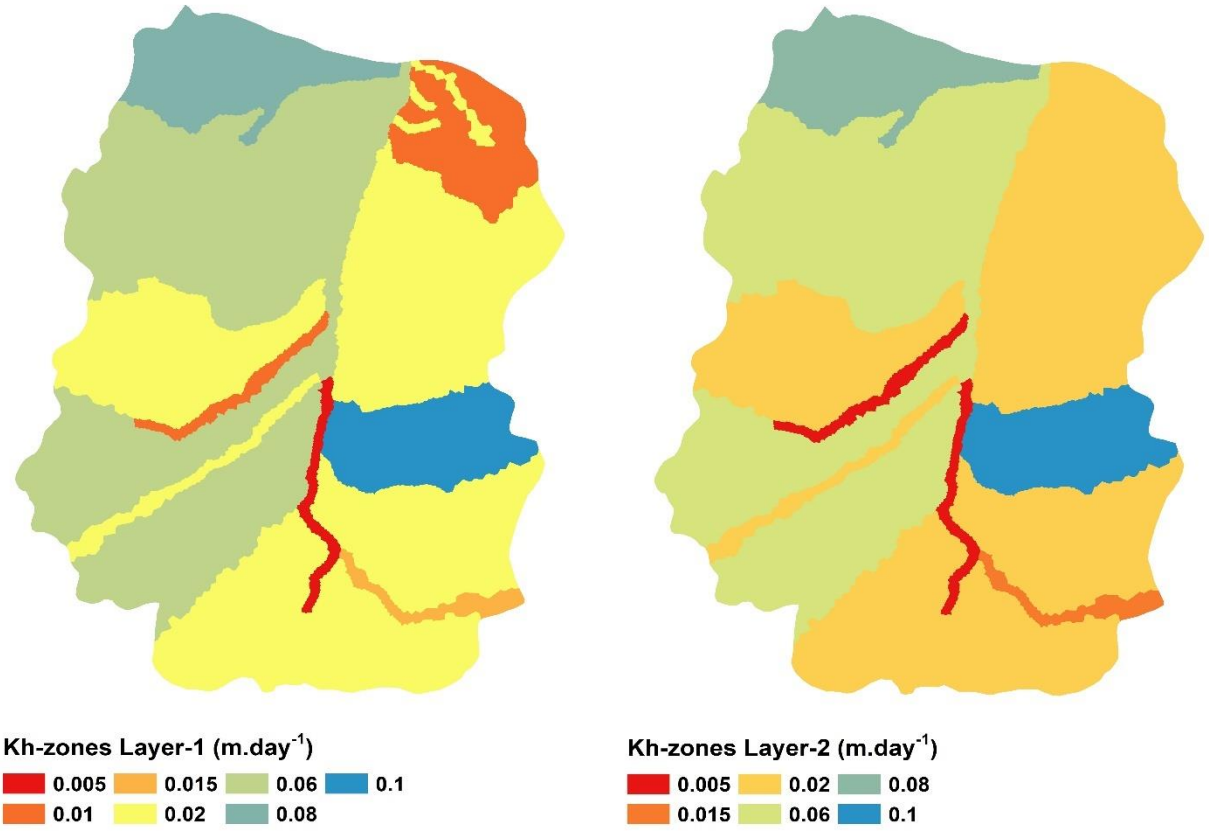

Figure 14: K_h of both layers.

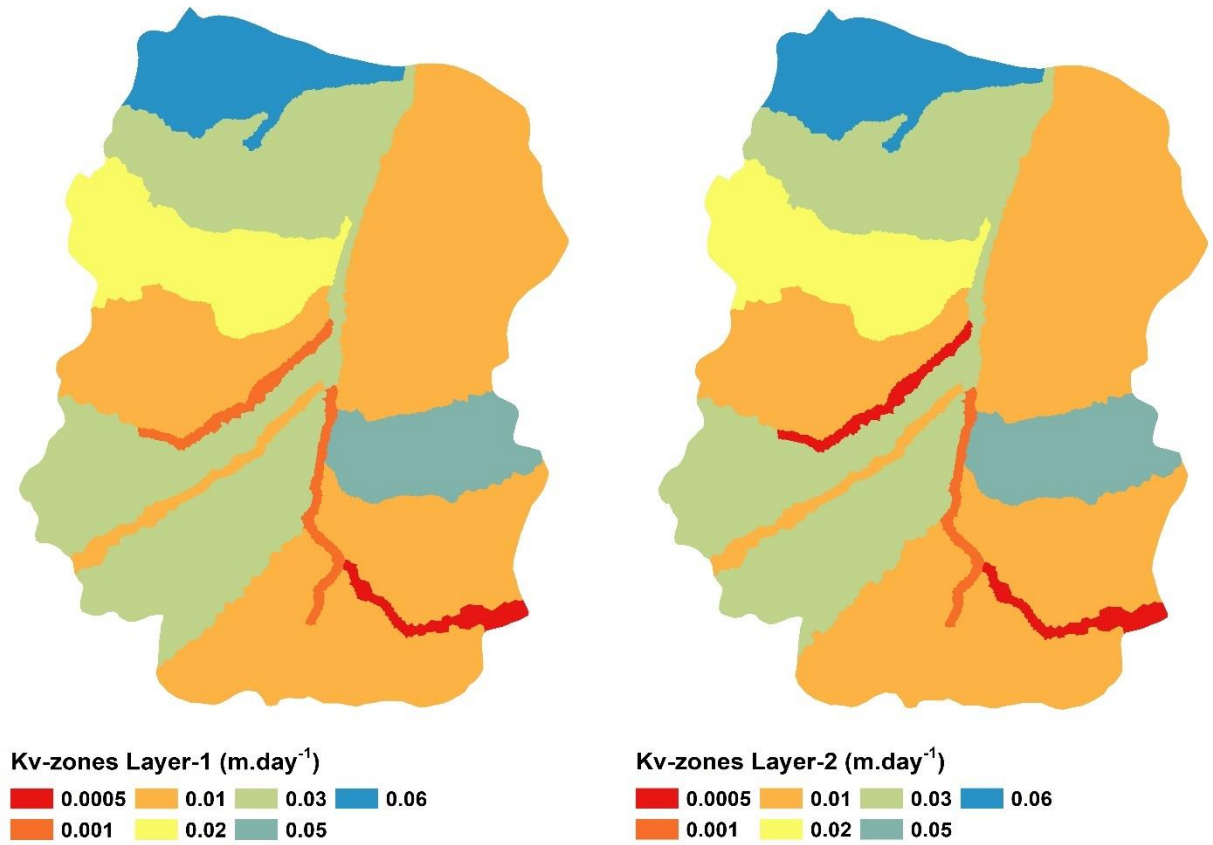

Figure 15: K_v of both layers.

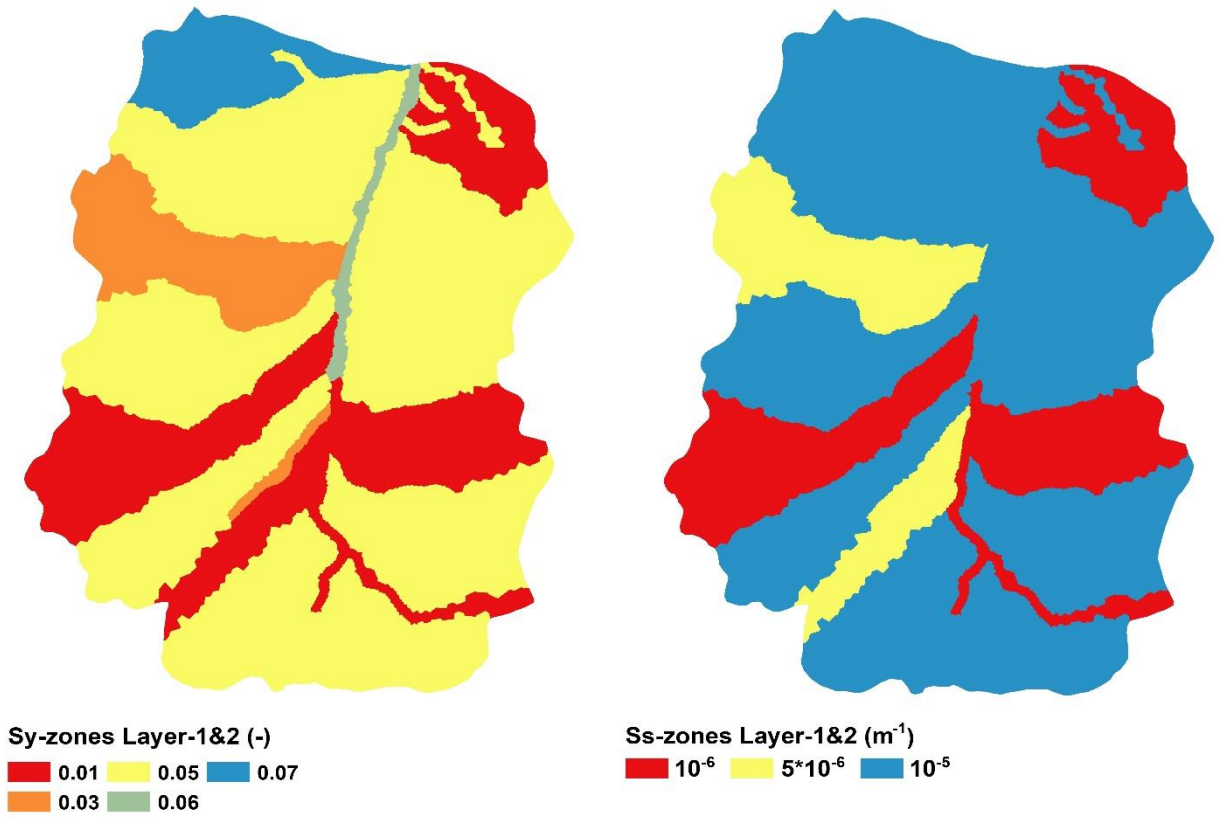

Figure 16: S_y and S_s of both layers.

5.2.4. Calibrated Groundwater Heads

Figure 17 and Figure 18 show the graphical comparison (a scatter plot and the residual errors plots respectively) between the simulated and observed heads of the 14 observation points during the entire model period. Table 9 shows the ranges of the summary statistics for each observation individually and the overall statistics for the entire model.

Table 9: Summary statistics ranges

Observation	MAE (m)	$RMSE$ (m)	Number of records
PGBO	0.68	0.82	1501
PGJO	0.62	0.91	2169
PGJTMO	0.23	0.32	297
PMU1	0.80	0.98	2502
PPNO	0.38	0.46	870
PSDO	0.63	0.80	1841
PTB2	0.51	0.60	703
PTM1	0.39	0.46	741
PTM2	0.51	0.66	1020
W1_PCL7	0.68	0.79	1461
W1_PN	0.39	0.52	1461
W1_SD	0.80	0.91	1466
W1_TB	0.16	0.19	1465
W2_PCL7	0.31	0.38	1462
Entire model	0.51	0.63	18959

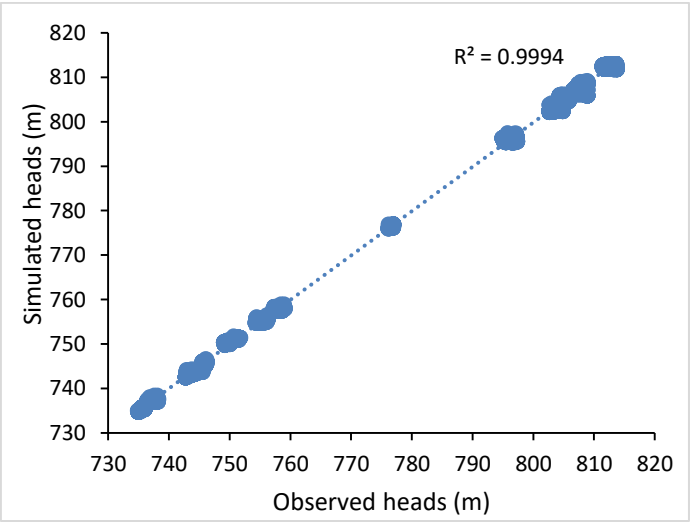

Figure 17: Scatter plot between observed and simulated heads for the entire model period.

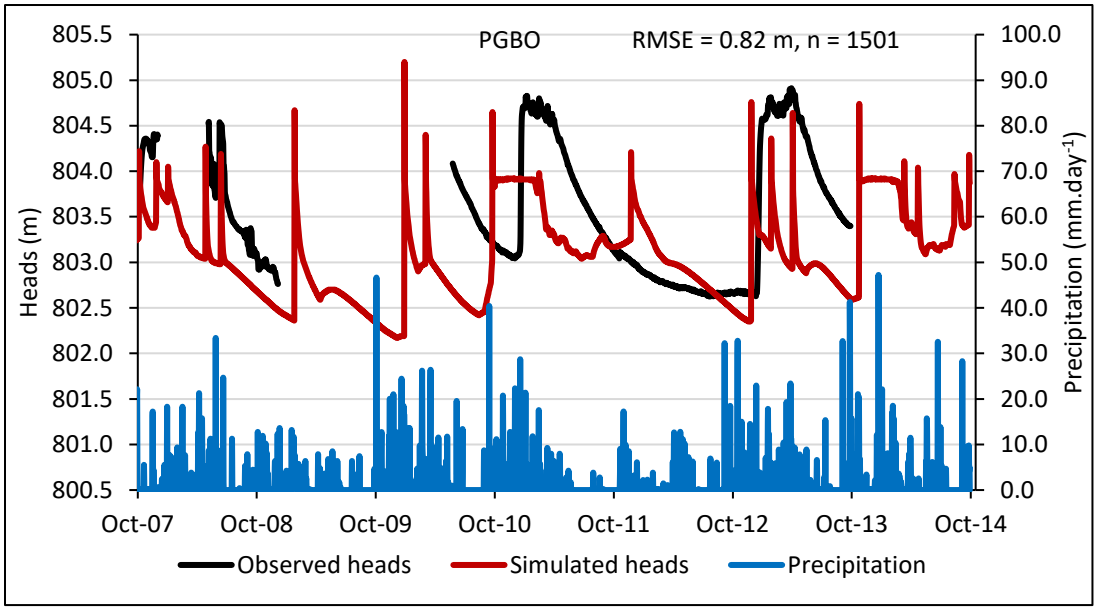
PGBO
RMSE = 0.82 m, n = 1501
Heads (m)
Precipitation (mm.day-1)
Observed heads
Simulated heads
Precipitation

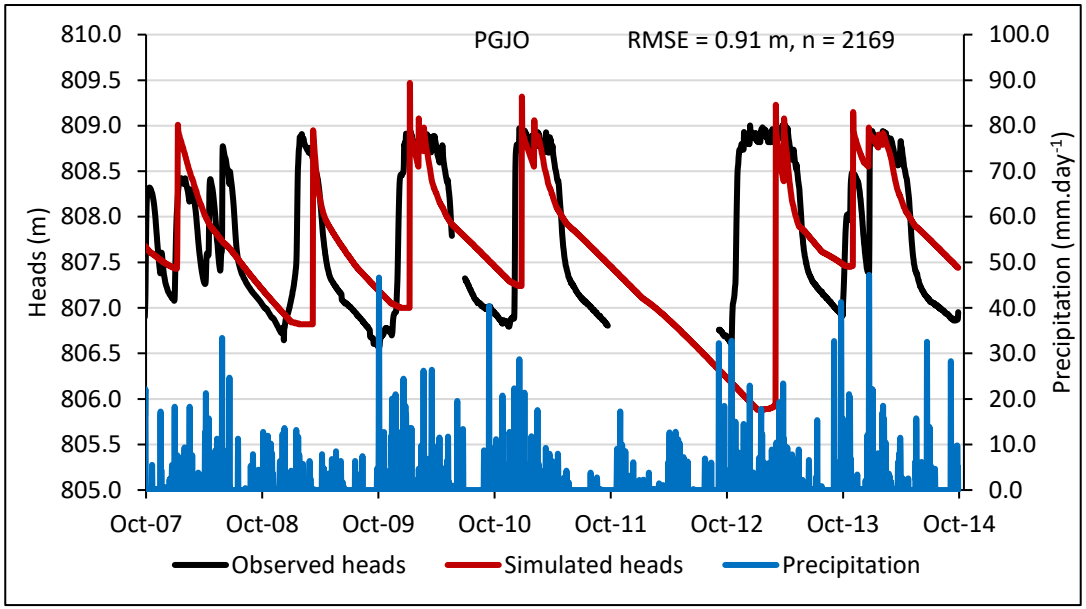
PGJO
RMSE = 0.91 m, n = 2169
Heads (m)
Precipitation (mm.day-1)
Observed heads
Simulated heads
Precipitation

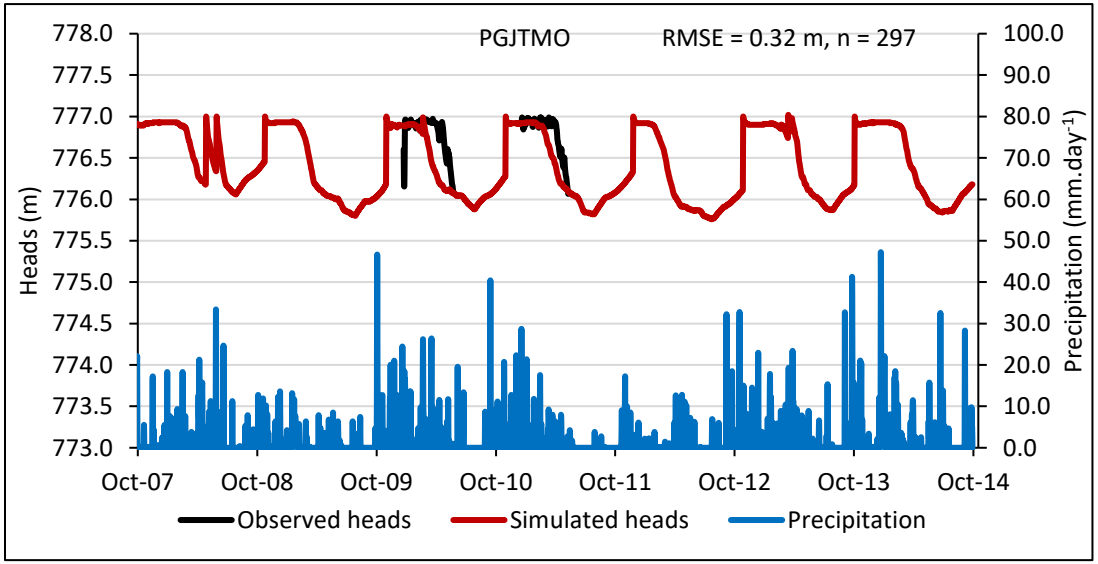
PGJTMO
RMSE = 0.32 m, n = 297
Heads (m)
Precipitation (mm.day-1)
Observed heads
Simulated heads
Precipitation

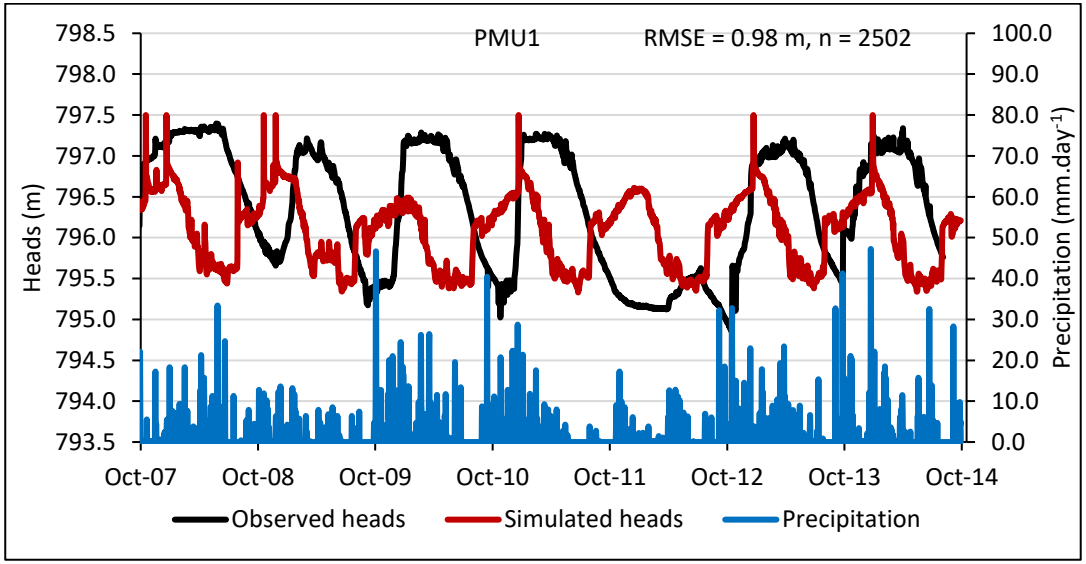
PMU1
RMSE = 0.98 m, n = 2502
Heads (m)
Precipitation (mm.day-1)
Observed heads
Simulated heads
Precipitation

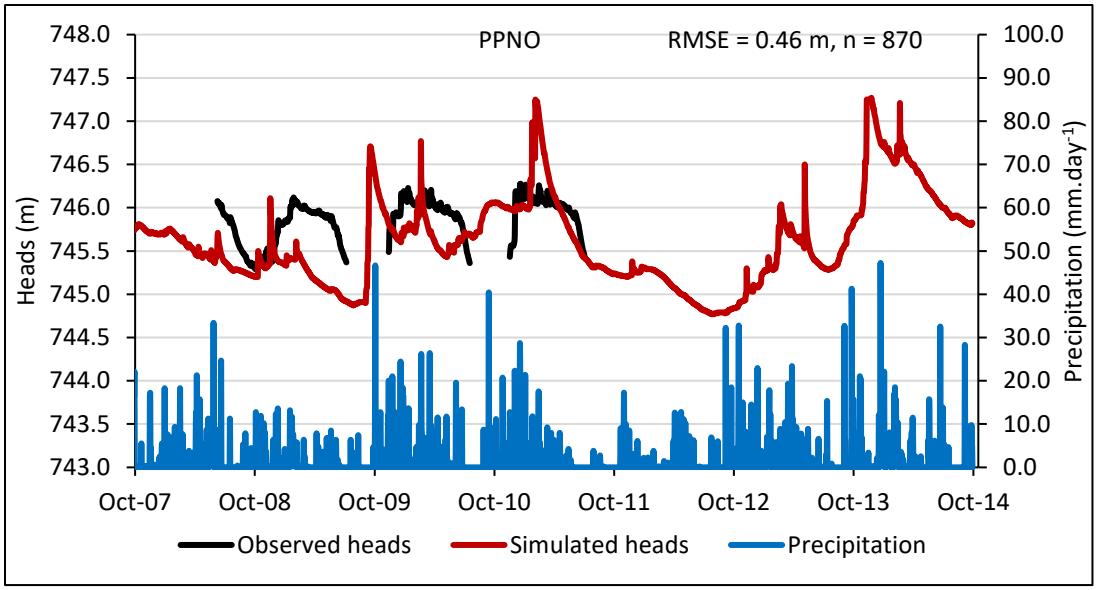
PPNO
RMSE = 0.46 m, n = 870
Heads (m)
Precipitation (mm.day-1)
Observed heads
Simulated heads
Precipitation

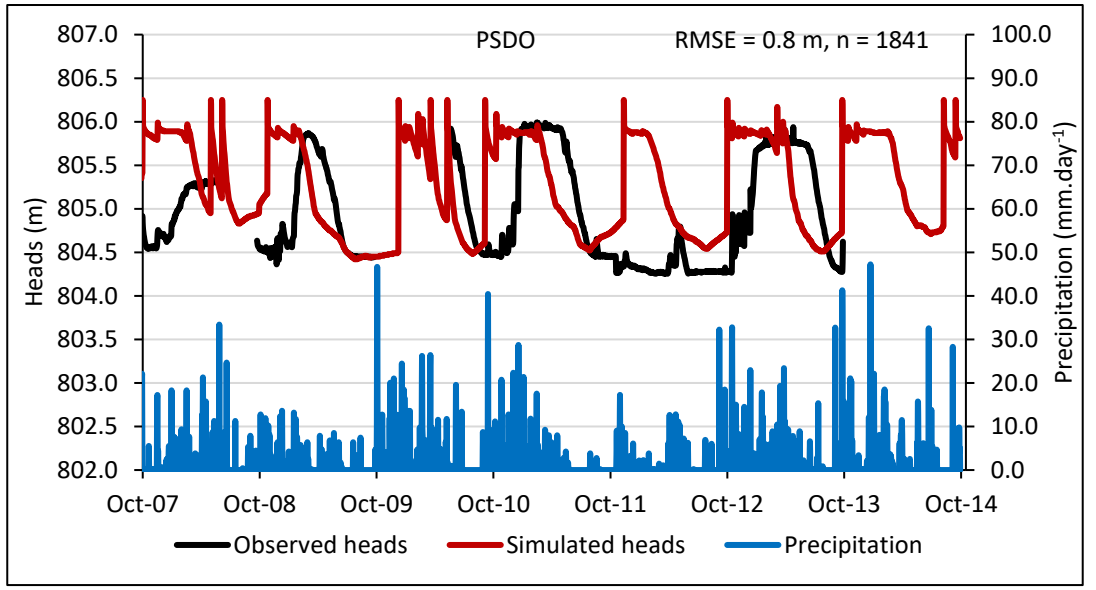
PSDO
RMSE = 0.8 m, n = 1841
Heads (m)
Precipitation (mm.day-1)
Observed heads
Simulated heads
Precipitation

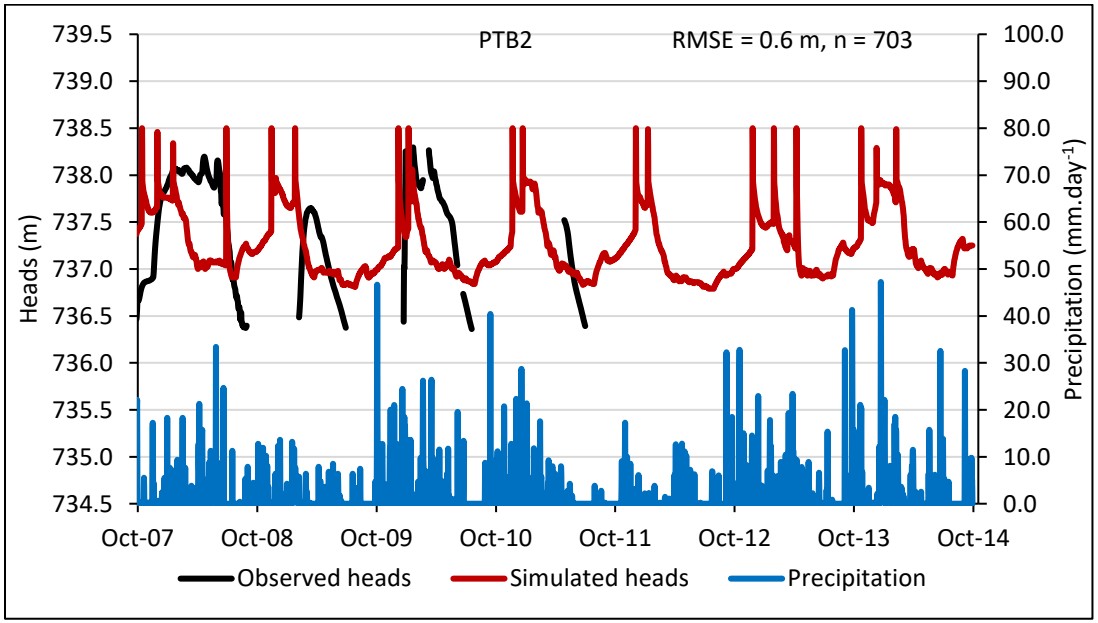
PTB2
RMSE = 0.6 m, n = 703
Heads (m)
Precipitation (mm.day-1)
Observed heads
Simulated heads
Precipitation

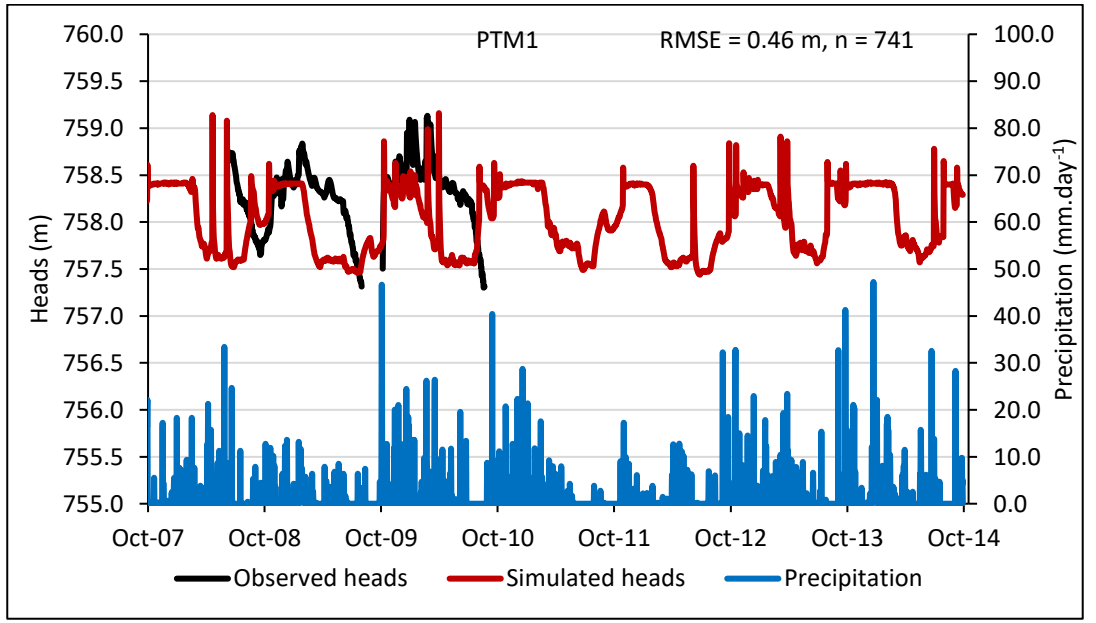
PTM1
RMSE = 0.46 m, n = 741
Heads (m)
Precipitation (mm.day-1)
Observed heads
Simulated heads
Precipitation

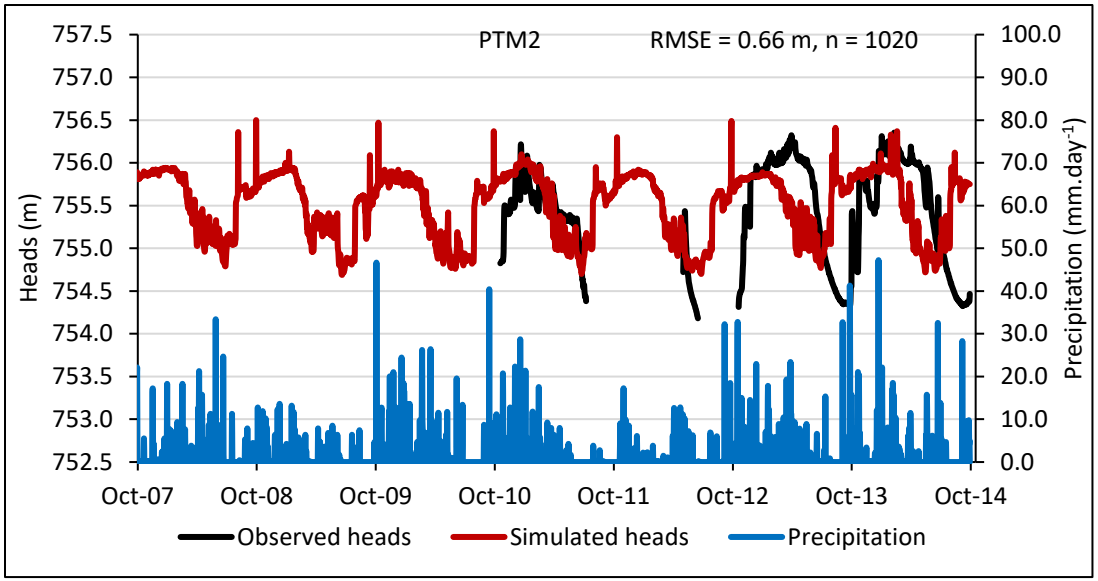
PTM2
RMSE = 0.66 m, n = 1020
Heads (m)
Precipitation (mm.day-1)
Oct-07
Oct-08
Oct-09
Oct-10
Oct-11
Oct-12
Oct-13
Oct-14
Observed heads
Simulated heads
Precipitation

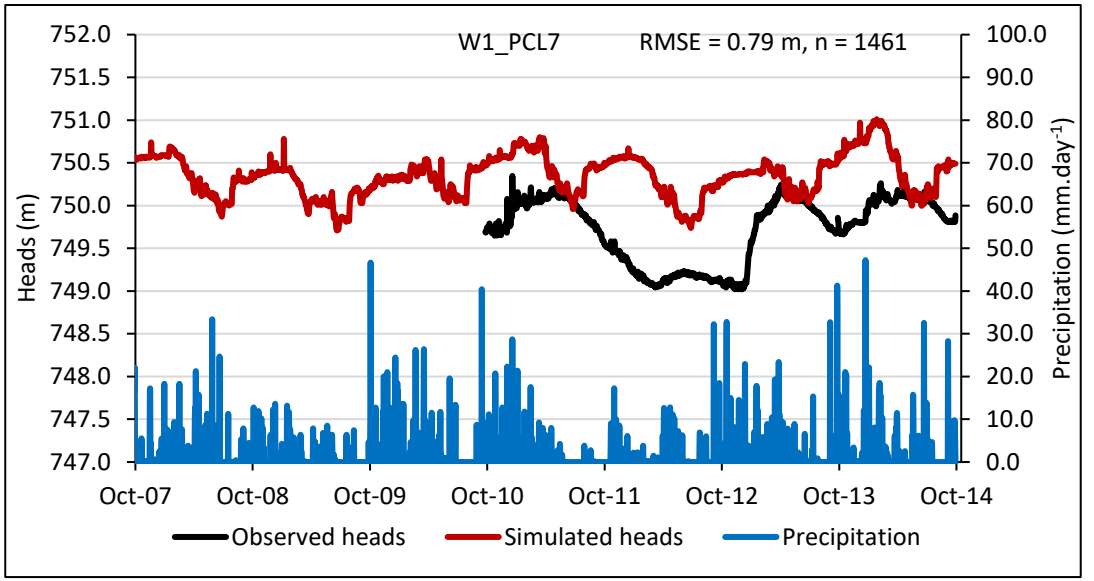
W1_PCL7
RMSE = 0.79 m, n = 1461
Heads (m)
Precipitation (mm.day-1)
Oct-07
Oct-08
Oct-09
Oct-10
Oct-11
Oct-12
Oct-13
Oct-14
Observed heads
Simulated heads
Precipitation

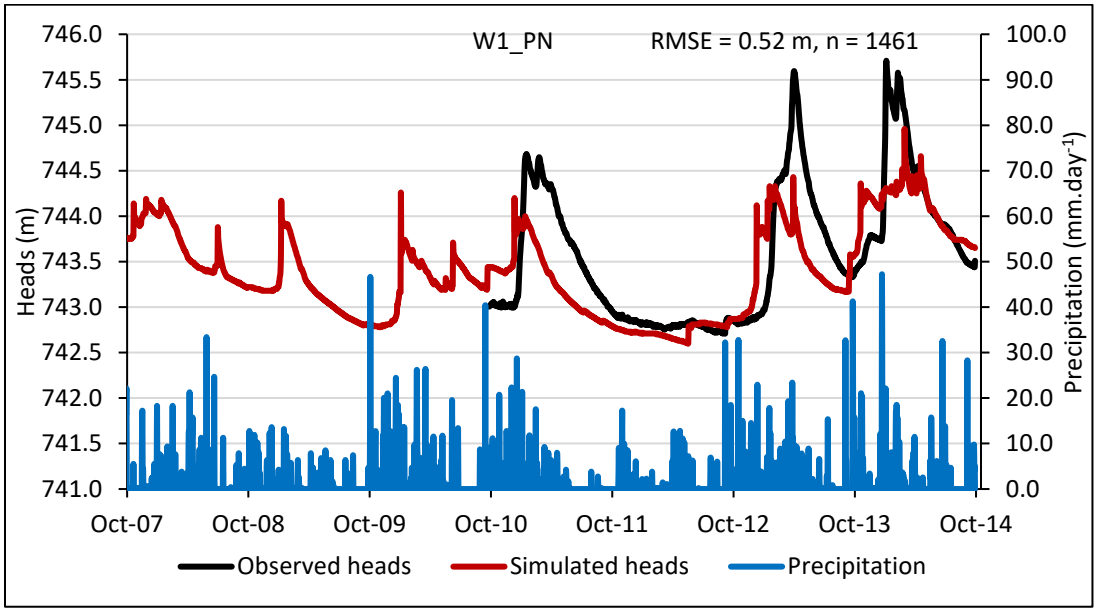
W1_PN
RMSE = 0.52 m, n = 1461
Heads (m)
Precipitation (mm.day-1)
Oct-07
Oct-08
Oct-09
Oct-10
Oct-11
Oct-12
Oct-13
Oct-14
Observed heads
Simulated heads
Precipitation

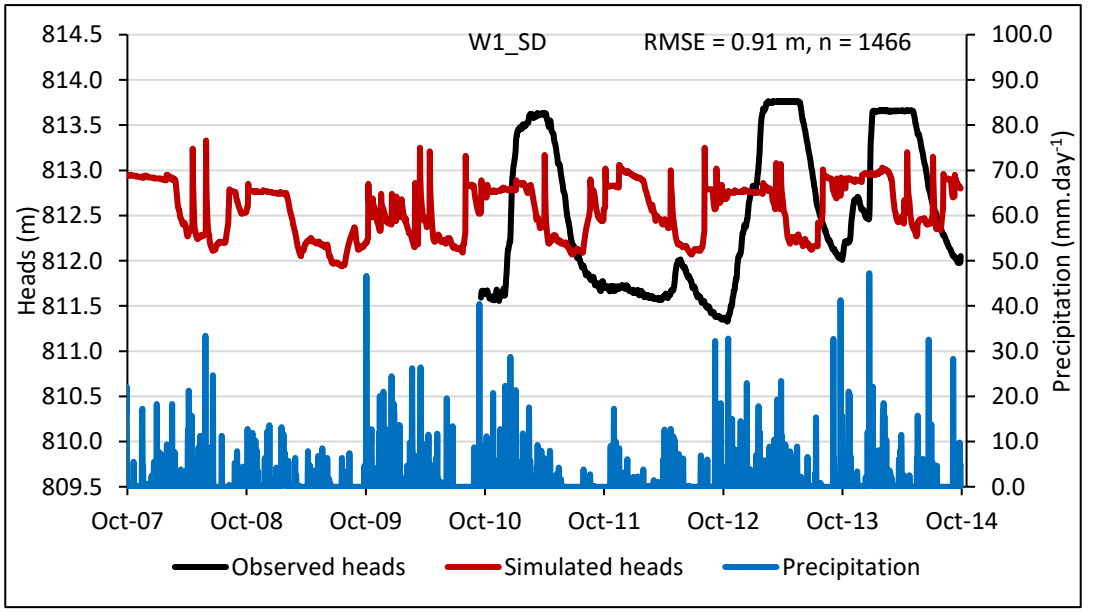
W1_SD
RMSE = 0.91 m, n = 1466
Heads (m)
Precipitation (mm.day-1)
Oct-07
Oct-08
Oct-09
Oct-10
Oct-11
Oct-12
Oct-13
Oct-14
Observed heads
Simulated heads
Precipitation

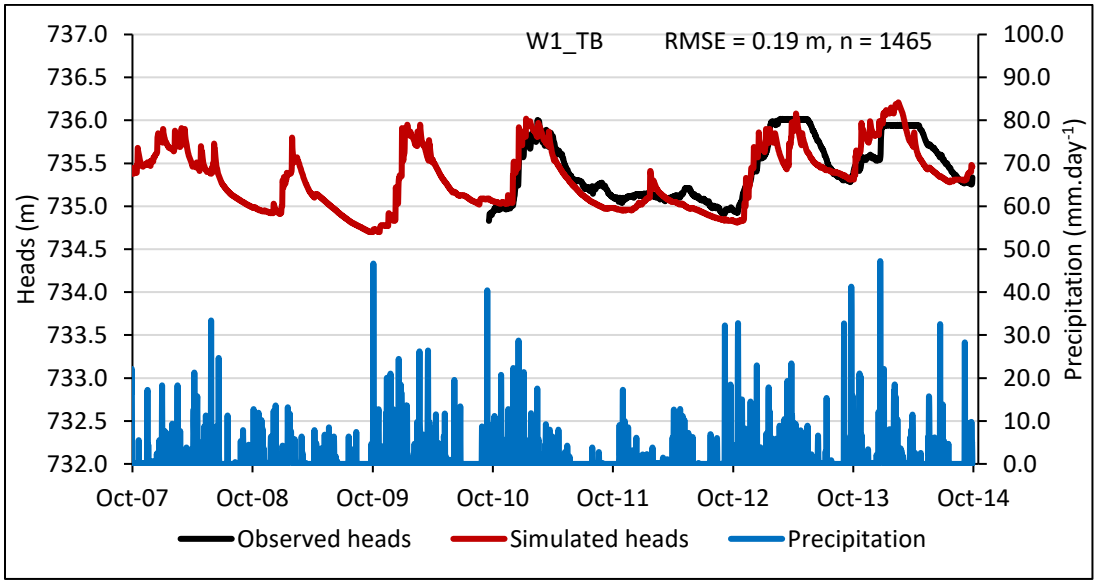

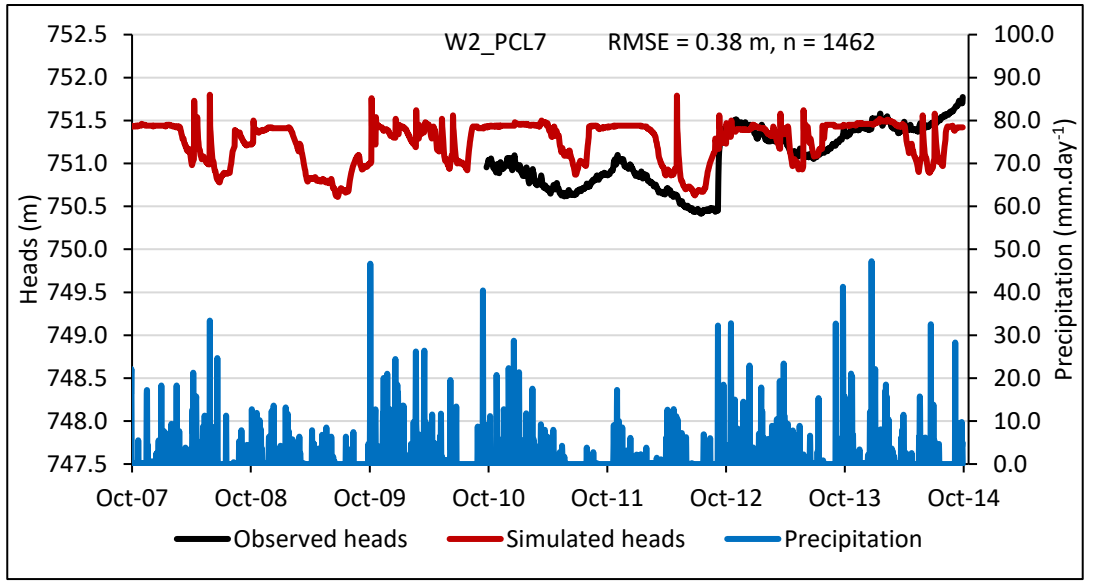

Figure 18: Simulated heads versus observed heads for the 14 observation points, showing the residual errors, the locations of the observation points in the study area are shown in Figure 1.

In general, there is a good match between the observed heads and the simulated heads, overall $RMSE$ of the entire model is 0.63 m, where the individual $RMSE$ is in the range of 0.19 to 0.98 m. Also, Figure 17 shows a high coefficient of determination (R^2 = 0.99) which indicates good calibration.

5.2.5. Calibrated Streamflow

The calibration of the streamflow at the catchment outlet was restricted to low flow conditions (< 145 l.s^{-1}, < 12528 m^3.day^{-1}), mainly because the flume capacity was 145 l.s^{-1} and the records higher than 145 l.s^{-1} are with high uncertainty as described by Hassan et al. (2014). Figure 19 shows the graphical comparison between the observed and the simulated streamflow at the catchment outlet. It was also noticed that the minimum simulated streamflow during the entire model is around 1400 m^3.day^{-1} (~16 l.s^{-1}) acts as baseflow (Figure 19-b). The VE between simulated and observed streamflow is 0.48 (almost acceptable ~0.5).

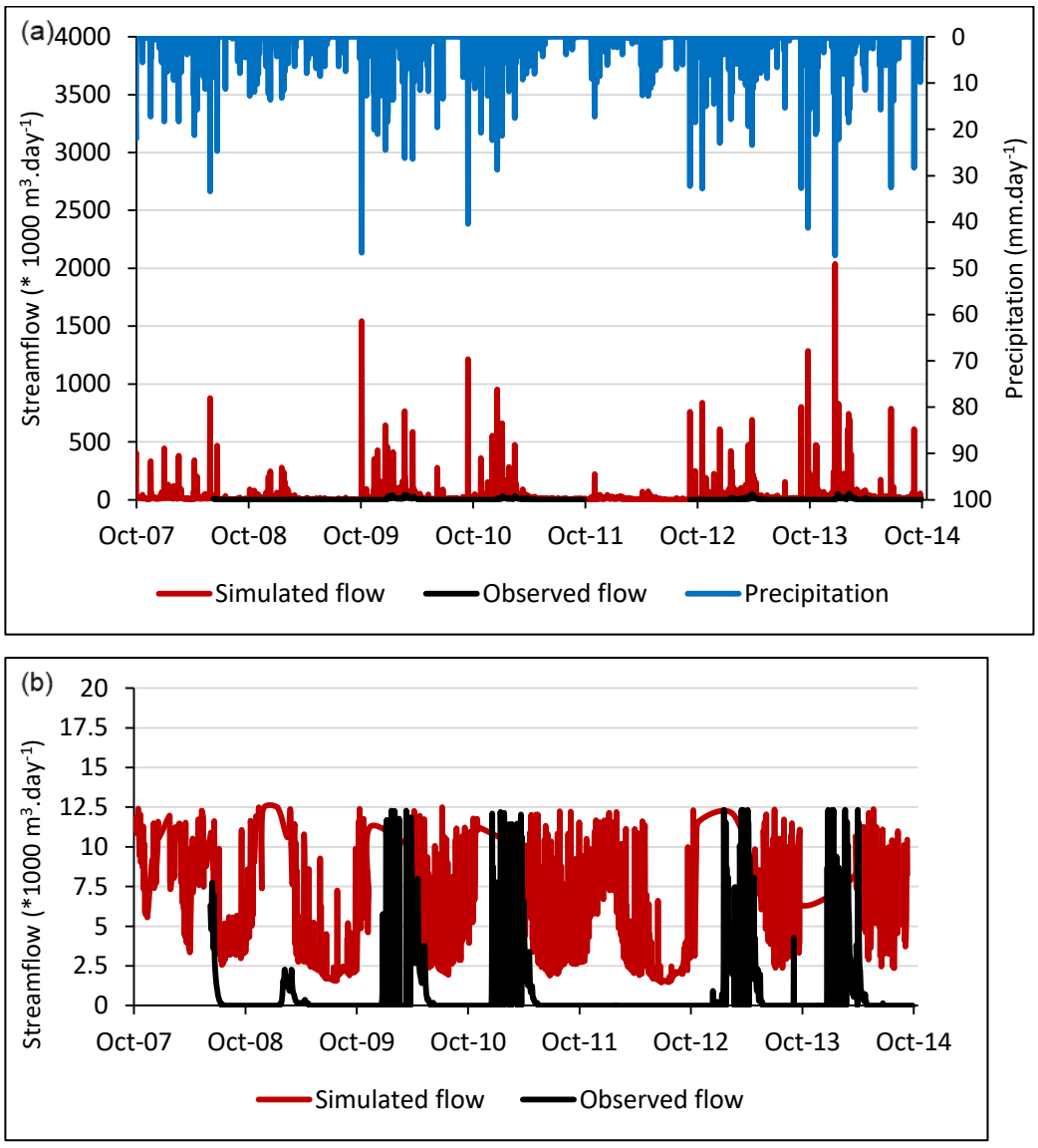

Figure 19: Simulated versus observed streamflow at the catchment outlet: (a) showing all simulated flow values including high and low flows, and (b) showing only low simulated flows (< 12.528 * 1000 m^3.day^{-1}, for calibration purposes).

5.3. Water Balance

The daily water balance of both: the land surface and the unsaturated zone, as well as the groundwater zone, were exported from the MODFLOW 6 output files. These daily rates were averaged to yearly rates, as shown in Table 10, representing the contribution of each component of the system in the water balance. Then, they were substituted in the water balance equations as described in section 4.4.3. Table 11 and Figure 20 show the mean water balance over the total model simulation period (2008-2014) of each zone separately: the land surface and the unsaturated zone (Eq. (24)), the groundwater zone (Eq. (25)), and the entire catchment (Eq. (20)).

The main input to the catchment is P = 539.5 mm.yr^{-1}, while the outputs are: ET = 66.2% of P, q = 31.5% of P, and negligible q_g = 0.1% of P. It was noticed that the main output is ET, substantially larger than q which was expected as the streamflow is intermittent in WLEs such as the Sardon catchment. The ET consists of five components, two surface components: E_{sf} = 8.5% of ET, RI^e = 10.4% of ET ,and three subsurface components: ET_u = 66.5% of ET, ET_g = 14% of ET, and Exf_{gw}^e = 0.1% of ET. It was noticed that the subsurface components contribute more to total ET (80.5% of ET) than the surface components. The q consists of three components: ($RI^s + Exf_{gw}^s$) = 92% of q, and q_B = 8% of q. The RI^s and Exf_{gw}^s, both together represents the overland flow, higher than the base flow (q_B), which was expected as the main source of the stream flow in WLEs such as the Sardon catchment is the overland flow.

For the unsaturated zone, the main input is P_e (94.4% of P), significantly high due to the low values of E_{sf} (5.6% of P). The reason for such low E_{sf} rate is due to the high coverage of the landcover class (grass \ bare soil, 94% of total catchment area) which had low E_{sf} rates, as shown in section 5.1.1. Additionally, the unsaturated zone received more water from the $RI^{ri} + Exf_{gw}^{ri}$ (10.3% of P and 22.4% of $RI + Exf_{gw}$), which eliminate the rejected infiltration as an output from the unsaturated zone. The ET_u highly contributed to the total ET (66.5% of ET) which shows the advantage of the IHMs over the standalone models to better simulate the surface-groundwater interaction, considering the unsaturated zone fluxes which highly affect the total water balance and the recharge/discharge conditions of the groundwater zone, especially in WLEs.

For the groundwater zone, it was noticed that the aquifer had different responses according to the dry/wet years. For example, in 2009 and 2012, when P was relatively low (317.2 and 334.5 mm.yr^{-1} respectively), the aquifer represented discharge conditions (R_n had negative values), while in 2010 and 2014 when P was high (744.1 and 725.9 mm.yr^{-1} respectively), the aquifer represented recharge conditions (R_n had positive values). Additionally, these recharge rates in the wet years were not high (8.8% of R_g) which indicates that the water resources to the aquifer are limited. The main output from the groundwater zone is Exf_{gw} (69% of R_g), which indicate the significance of this process.

Table 10: Yearly water balance of each system component as described in section 4.4.3, each hydrological year starts from 1 October of the previous year and ends at 30 September of that year, positive and negative signs are according to Equations (20)-(25), all values are in mm.yr^{-1}

Year	P	E_{sf}	P_e	ET	ET_u	RI	RI^e	Exf_{gw}^e	RI^r	Exf_{gw}^r	$RI^{ri} + Exf_{gw}^{ri}$	q_g	q_{sg}	q_{gs}	q_B	$RI^s + Exf_{gw}^s$	q	R_g	ET_g	Exf_{gw}	R_n	ΔS_u	ΔS_g	ΔS
2008	542.31	31.07	511.24	415.08	301.41	88.61	25.91	0.46	62.70	89.67	42.93	0.54	0.68	15.66	14.98	109.44	124.42	140.90	56.22	90.13	-5.46	-21.59	21.14	-0.46
2009	317.22	24.03	293.18	267.46	187.52	38.16	15.04	0.34	23.13	66.28	27.38	0.45	0.86	13.06	12.20	62.04	74.24	100.80	40.53	66.63	-6.35	7.20	19.17	26.36
2010	744.14	34.91	709.23	446.85	294.20	167.80	55.29	0.60	112.51	191.97	77.34	0.49	0.84	14.96	14.13	227.15	241.28	276.55	61.84	192.58	22.13	-46.51	-7.56	-54.06
2011	440.83	24.07	416.75	301.03	184.13	89.67	37.29	0.56	52.38	176.57	70.76	0.45	0.67	15.42	14.75	158.20	172.95	248.62	54.98	177.13	16.51	35.50	-1.23	34.27
2012	334.54	22.18	312.36	274.73	217.82	29.20	7.75	0.29	21.44	36.04	17.45	0.41	0.86	11.16	10.29	40.15	50.45	56.35	26.69	36.33	-6.67	-25.81	17.31	-8.50
2013	671.52	38.77	632.76	379.98	237.39	145.50	47.61	0.61	97.89	165.73	63.76	0.51	0.79	15.79	15.00	199.87	214.86	249.18	55.60	166.34	27.25	-62.91	-11.8	-74.77
2014	725.92	37.86	688.05	412.94	238.20	207.88	71.25	0.69	136.64	248.46	91.17	0.61	0.60	17.34	16.73	294.00	310.73	347.65	64.94	249.15	33.57	15.92	-16.2	-0.26
Mean	539.50	30.41	509.08	356.87	237.24	109.55	37.16	0.51	72.38	139.25	55.83	0.5	0.76	14.77	14.01	155.84	169.85	202.87	51.54	139.76	11.57	-14.03	2.97	-11.06
Min	317.22	22.18	293.18	267.46	184.13	29.20	7.75	0.29	21.44	36.04	17.45	0.41	0.60	11.16	10.29	40.15	50.45	56.35	26.69	36.33	-6.67	-62.91	-16.2	-74.77
Max	744.14	38.77	709.23	446.85	301.41	207.88	71.25	0.69	136.64	248.46	91.17	0.61	0.86	17.34	16.73	294.00	310.73	347.65	64.94	249.15	33.57	35.50	21.14	34.27

Table 11: Mean water balance over the total model simulation period (2008-2014) of each system zone separately, positive values indicate inputs to the zone and negative values indicate outputs from the zone, all values are in mm.yr^{-1}

Zone	P	P_e	ET	ET_u	RI	$RI^{ri} + Exf_{gw}^{ri}$	q_g	q_{sg}	q_{gs}	q	R_g	ET_g	Exf_{gw}	ΔS_u	ΔS_g	ΔS	In	Out	In-out	Discrepancy
Land surface and unsaturated zone		509.1		-237.24	-109.55	55.83					-202.87			-14.03			564.91	-563.68	1.23	0.22%
Groundwater zone							-0.50	0.76	-14.77		202.87	-51.54	-139.76		2.97		202.87	-202.84	0.03	0.01%
Entire catchment	539.5		-356.87				-0.50			-169.85						-11.06	539.5	-538.27	1.23	0.23%

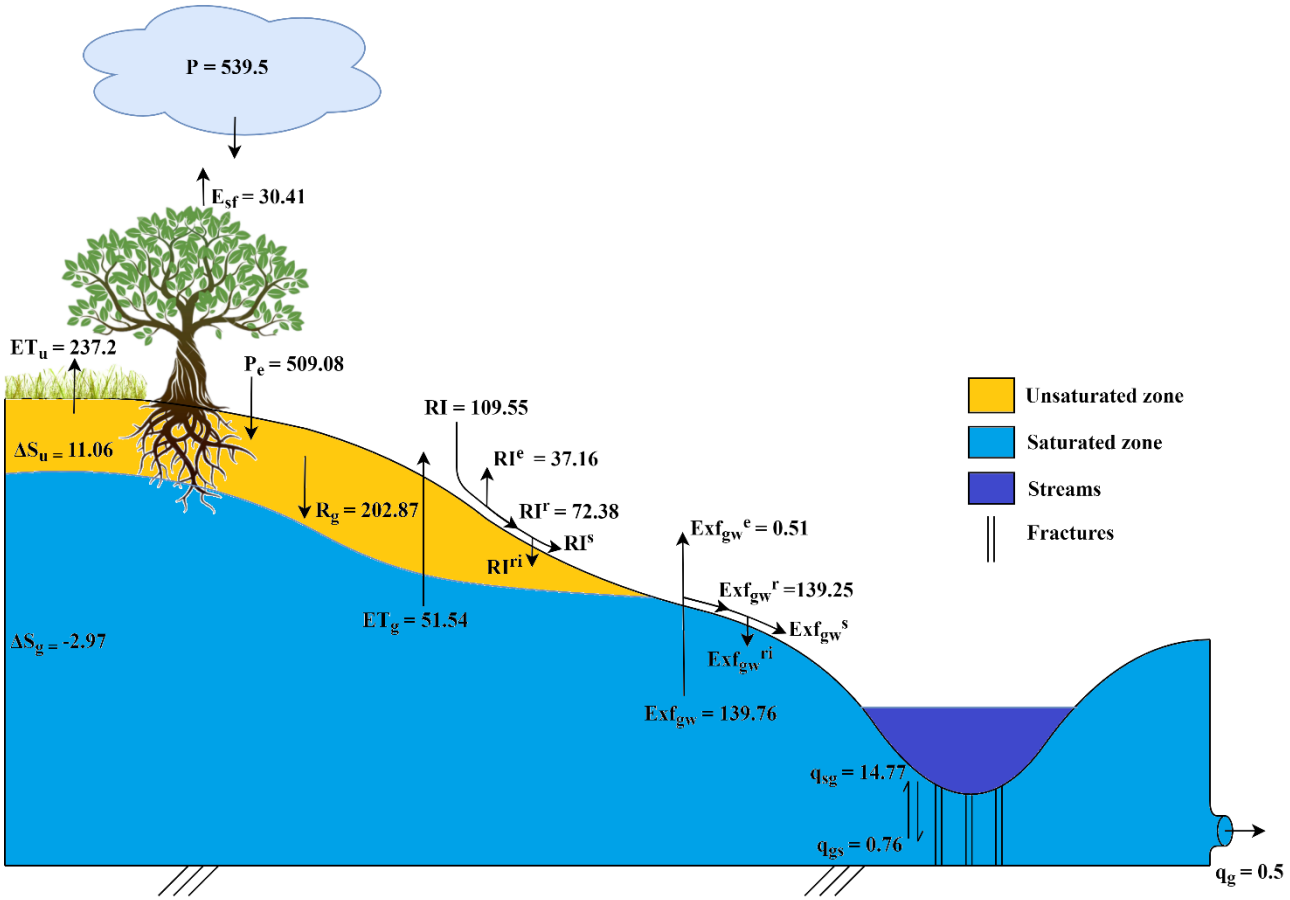

Figure 20: Mean water balance of the entire catchment over the total model simulation period in mm.yr^{-1}.

5.4. Spatial Distribution of Water Fluxes

The spatial distribution of the water balance components (water fluxes) was extracted from the model outputs for two hydrological years: 2009 (dry year with P = 317.2), and 2010 (wet year with P = 744.1). Only the groundwater zone fluxes (R_g, Exf_{gw}, ET_g and R_n) are shown in Figure 21 and Figure 22 due to their importance and text size limitation to show all other figures. It was observed that the R_g were high (>200 mm.yr^{-1}) in the drainage areas (along the Sardon river and its tributaries) due to shallow water table conditions and the faults network in those areas. Also, the north-western and south-eastern parts of the catchment had significantly high R_g fluxes, most likely due to their flat slopes. The low R_g fluxes were spread in the entire catchment, mainly in the areas characterized by hilly slopes or the existence of the outcrops which are impermeable. R_g in 2010 was higher than R_g in 2009, which was expected as 2010 is a wet year, so the groundwater zone received more water.

Considering the Exf_{gw}, it was noticed that it almost followed the same pattern as R_g, high fluxes at the north-western and south-eastern parts of the catchment, and in the drainage areas where the water table is shallow. ET_g were high in the drainage areas due to shallow water table conditions and relatively high extinction depth (existence of the two tree species, with extinction depth = 3.7 m).

The spatial distribution of R_n is affected by the spatial distribution of R_g, Exf_{gw} and ET_g. R_n was observed with positive values (recharge areas) in the north-western part of the catchment, while it had negative values (discharge areas) in the southern part of the catchment, and in the drainage areas where Exf_{gw} and ET_g are relatively high. R_n in 2009 was lower than R_n in 2010, which was expected as 2009 is a dry year, with high fluxes of Exf_{gw} and ET_g, relative to low fluxes of R_g, and therefore, the discharge areas (R_n< 0) in 2009 are more than in 2010.

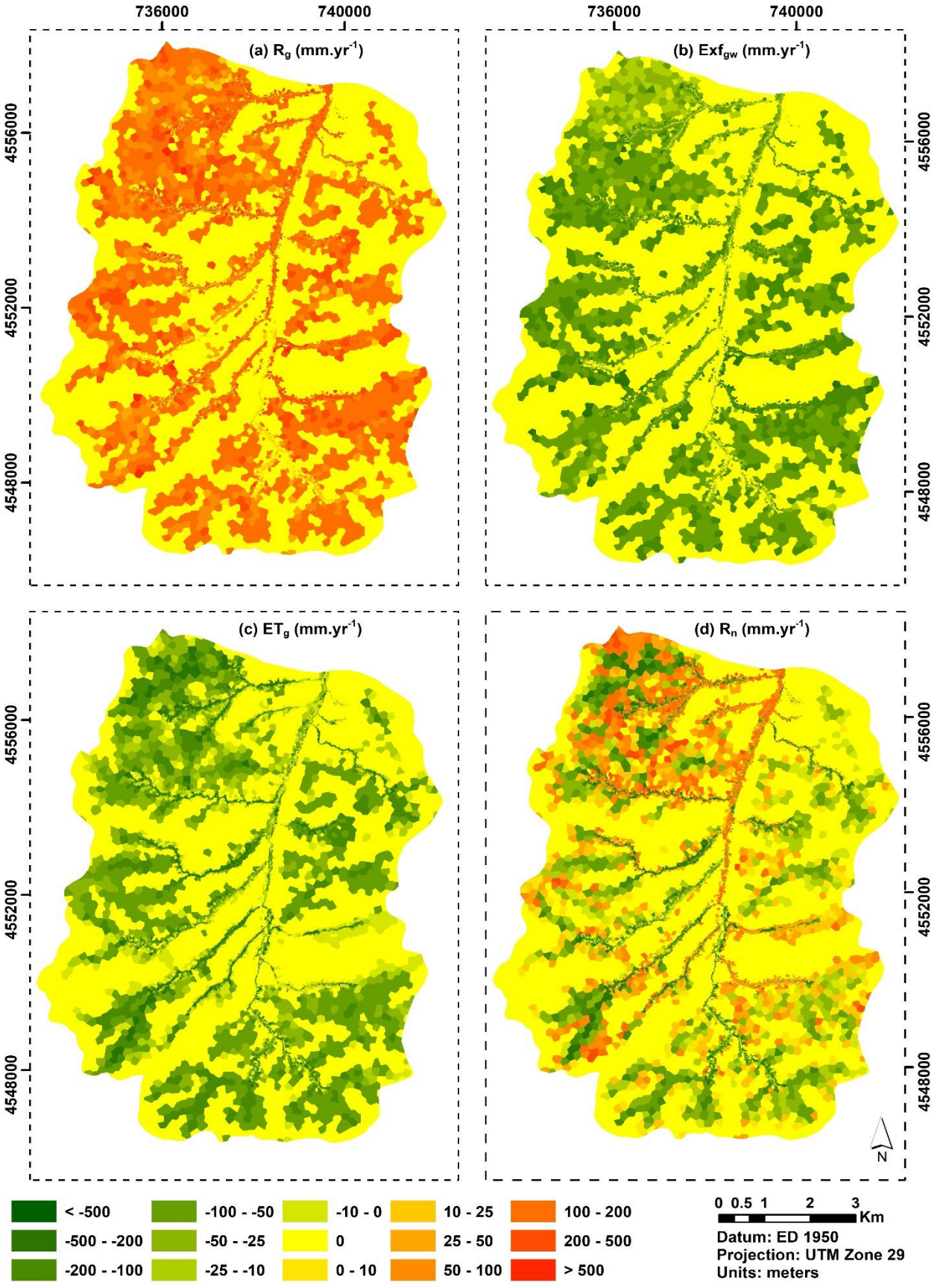

Figure 21: Spatial distribution of the groundwater zone fluxes (model output) for the hydrological year 2009: (a) R_g, (b) Exf_{gw}, (c) ET_g, and (d) R_n.

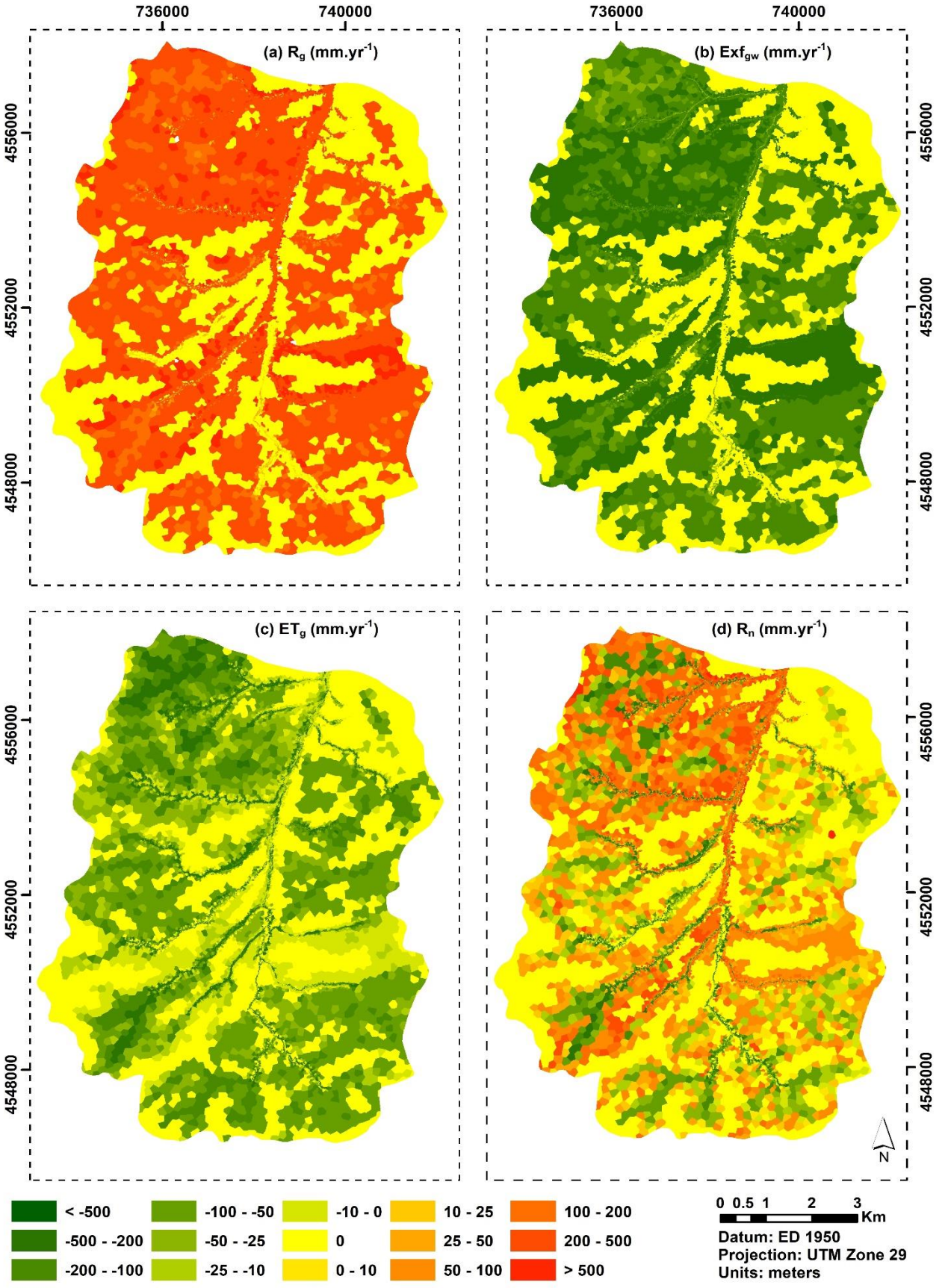

Figure 22: Spatial distribution of the groundwater zone fluxes (model output) for the hydrological year 2010: (a) R_g, (b) Exf_{gw}, (c) ET_g, and (d) R_n.

5.5. Temporal Variability of Water Fluxes

The temporal variability of all the water fluxes was observed significantly. The high temporal variability of the precipitation (P), ranged from 317.22 mm.yr^{-1} in 2009 to 744.14 mm.yr^{-1} in 2010, had affected the temporal variability of the groundwater heads (Figure 18), the streamflow (Figure 19), and all other water fluxes. Figure 23 shows the yearly temporal variability of all the water fluxes during the entire model period. The most correlated fluxes with the P were P_e, RI, ET, and q, while the least correlated fluxes with P were ET_u, as it was also affected by the temporal variability of the PET (Figure 25).

The Sardon area is a WLE with typical showers that occurred many times along the 7-year simulation period (2008-2014). These showers can be categorized into two types: normal showers, occurred 100 times in the 7 years with 10 < P < 30 mm.day^{-1}, and extreme showers, occurred 8 times in the 7 years with P > 30 mm.day^{-1}. This kind of high daily variability of P, in addition to the low storage of the unsaturated and saturated zones, was reflected in the daily variability of the surface and subsurface water fluxes.

For the groundwater zone fluxes, it was observed that, during the dry years such as 2009, the daily average values of R_g and Exf_{gw} were low (0.27 and 0.18 mm.day^{-1} respectively), low average ET_g (0.11 mm.day^{-1}), resulting in a very low daily average R_n (-0.02 mm.day^{-1}), with negative values representing discharge conditions (Figure 24-b). During the wet years such as 2010, the average daily of R_g and Exf_{gw} were high (0.77 and 0.52 mm.day^{-1} respectively), average ET_g (0.16 mm.day^{-1}) resulting in a relatively high average R_n (0.1 mm.day^{-1}) representing recharge conditions (Figure 24-c). Additionally, the maximum daily values of R_g, Exf_{gw} and R_n were observed in the winter period (December to February) of each year, when P was high, in contrast to very low R_g, Exf_{gw} and R_n during the summer period (June to August) of each year due to very low or no P (Figure 24-a). Figure 25-a illustrates the correlation between the groundwater zone fluxes versus P. It showed that R_g and ET_g had high correlation with P (0.71 and 0.74 respectively), Exf_{gw} with substantial lower correlation (0.67), resulting in R_n with lower correlation (0.66).

The temporal variability of ET depended on its contributions (E_{sf}, RI^e, ET_u, ET_g and Exf_{gw}^e). The temporal variability of ET_u depended mainly on the PET and the water availability in the unsaturated zone. During the dry years such as 2009, ET_u was high (peak = 2.6 mm.day^{-1}) in the late spring period (April to June) due to high PET, although the soil moisture was relatively moderate due to moderate P (Figure 24-e). During the wet seasons such as 2010, ET_u was relatively higher (peak = 3.37 mm.day^{-1}) in the late spring period (April to June) due to high soil moisture and high PET (Figure 24-f). In the periods (from August to October and from December to February) of every year, including the dry and wet years, ET_u become low (0.05 mm.day^{-1}) due to either, low PET or low soil moisture (Figure 24-d).

The temporal variability of ET_g and Exf_{gw}^e depended mainly on the groundwater table. During the dry years such as 2009, the groundwater table was deep, resulting in low daily average ET_g and Exf_{gw}^e (0.11 mm.day^{-1} and 0.18 mm.day^{-1} respectively) (Figure 24-e), while during the wet years such as 2010, the groundwater table was shallow, resulting in higher daily average ET_g and Exf_{gw}^e (0.16 and 0.52 mm.day^{-1} respectively) (Figure 24-f). The maximum values of ET_g were observed in the spring period (March to May) of each year, while the maximum values of Exf_{gw}^e were observed in the winter period (December to February) of each year (Figure 24-d, e, and f). The minimum values of ET_g were observed in the autumn period (September to November) of each year, while the minimum values of Exf_{gw}^e were observed in the summer period (June to August) of each year (Figure 24-d, e, and f).

The temporal variability of RI^e followed the temporal variability of P in each year (Figure 24-d), which is expected as RI^e is originated from P, and the correlation between them is forced. RI^e was observed with extreme and intermittent peaks in the late autumn and winter periods (November to February) of each year and very low or zero values in the summer period (June to August) of each year, when P was very low or zero.

The temporal variability of ET followed significantly the temporal variability of ET_u, as ET_u was the largest contribution to ET (66.5%), observed with few extreme and intermittent peaks that were originated from RI^e during the extreme rainfall days.

The temporal variability of q depended on its contributions ($RI^s + Exf_{gw}^s$ and q_B). $RI^s + Exf_{gw}^s$ were observed with extreme and intermittent peaks in the late autumn and winter periods (November to February) of each year and very low or zero values in the summer period (June to August) of each year, when P was very low or zero (Figure 24-g, h, and i).

The temporal variability of q_B was more gentle than $RI^s + Exf_{gw}^s$, almost average daily values (0.035 mm.day^{-1}) along the entire year, with relatively higher values (0.07 mm.day^{-1}) in the winter period (December to February) of each year and lower values (0.01 mm.day^{-1}) in the summer period (June to August) of each year (Figure 24-g). In wet years as 2010, the daily average q_B was 0.039 mm.day^{-1}, higher than the daily average in dry years (0.033 mm.day^{-1}) such as 2009 (Figure 24-h and Figure 24-i).

The temporal variability of q followed significantly the temporal variability of $RI^s + Exf_{gw}^s$, as $RI^s + Exf_{gw}^s$ were the largest contribution to q (92%), observed with extreme and intermittent peaks in the late autumn and winter periods (October to February) of each year. In addition, q had continuous low values along the entire simulation period, following the distribution of q_B (Figure 24-g).

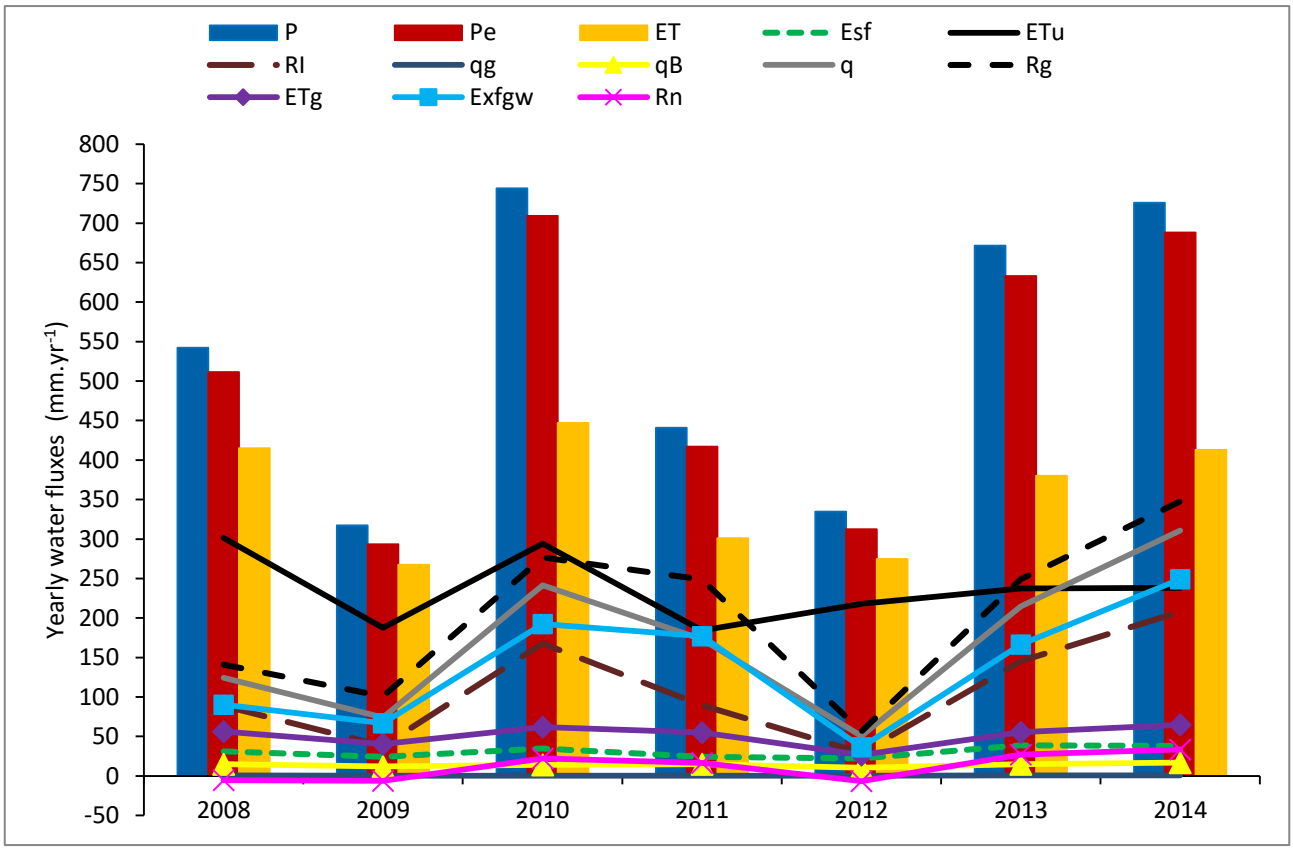

Figure 23: Yearly temporal variability of the water fluxes.

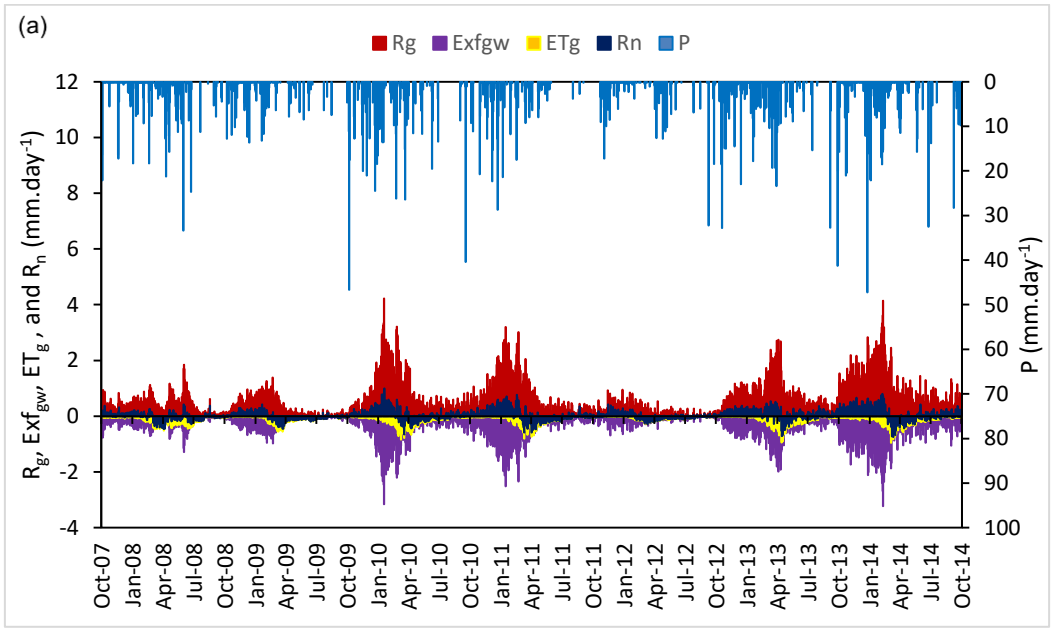
(a)
Rg
Exfgw
ETg
Rn
P
R_g, Exf_{gw}, ET_g, and R_n (mm.day^{-1})
P (mm.day^{-1})
Oct-07
Jan-08
Apr-08
Jul-08
Oct-08
Jan-09
Apr-09
Jul-09
Oct-09
Jan-10
Apr-10
Jul-10
Oct-10
Jan-11
Apr-11
Jul-11
Oct-11
Jan-12
Apr-12
Jul-12
Oct-12
Jan-13
Apr-13
Jul-13
Oct-13
Jan-14
Apr-14
Jul-14
Oct-14

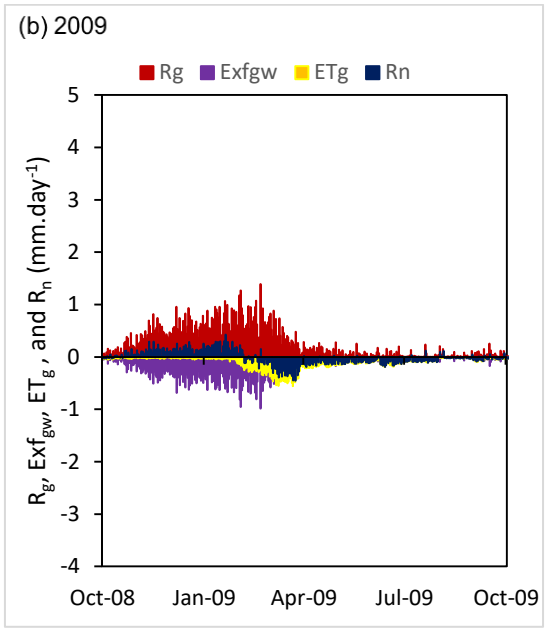
(b) 2009
Rg
Exfgw
ETg
Rn
R_g, Exf_{gw}, ET_g, and R_n (mm.day^{-1})
Oct-08
Jan-09
Apr-09
Jul-09
Oct-09

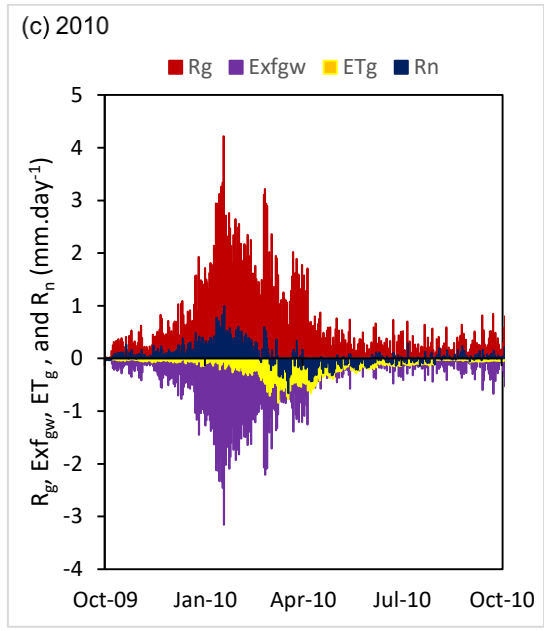
(c) 2010
Rg
Exfgw
ETg
Rn
R_g, Exf_{gw}, ET_g, and R_n (mm.day^{-1})
Oct-09
Jan-10
Apr-10
Jul-10
Oct-10

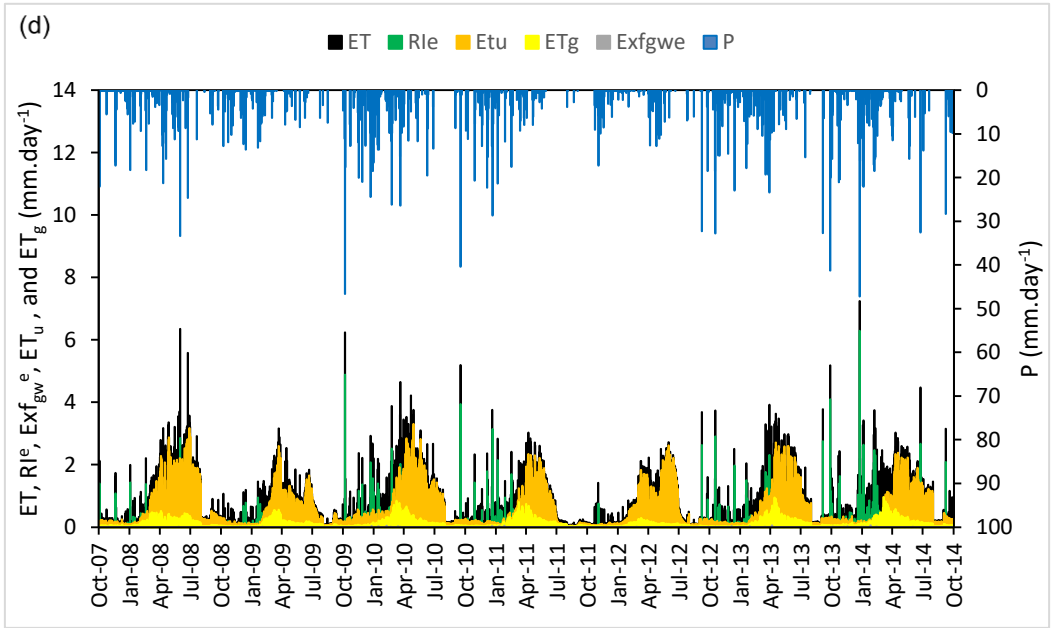
(d)
ET
RIe
Etu
ETg
Exfgwe
P
ET, RI^e, Exf_{gw}^e, ET_u, and ET_g (mm.day^{-1})
P (mm.day^{-1})
Oct-07
Jan-08
Apr-08
Jul-08
Oct-08
Jan-09
Apr-09
Jul-09
Oct-09
Jan-10
Apr-10
Jul-10
Oct-10
Jan-11
Apr-11
Jul-11
Oct-11
Jan-12
Apr-12
Jul-12
Oct-12
Jan-13
Apr-13
Jul-13
Oct-13
Jan-14
Apr-14
Jul-14
Oct-14

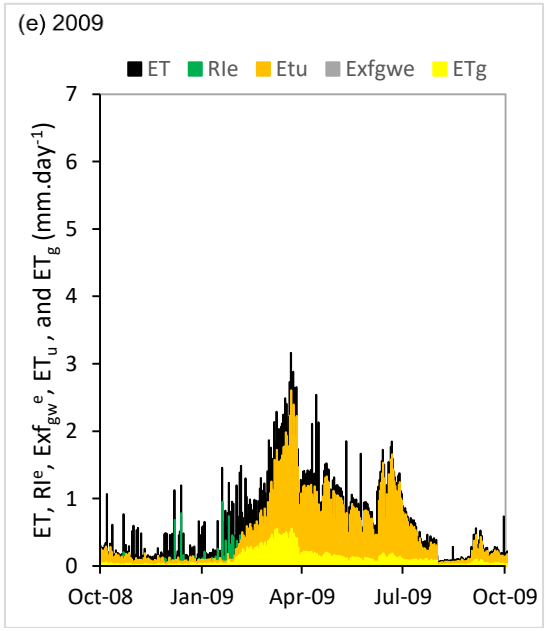
(e) 2009
ET
RIe
Etu
Exfgwe
ETg
ET, RI^e, Exf_{gw}^e, ET_u, and ET_g (mm.day^{-1})
Oct-08
Jan-09
Apr-09
Jul-09
Oct-09

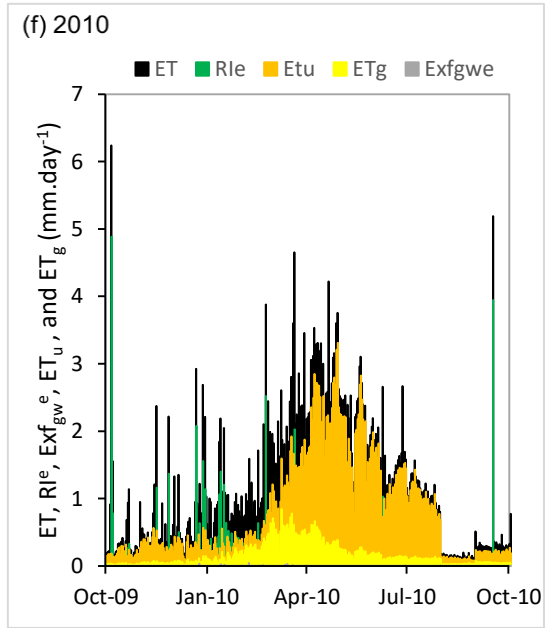
(f) 2010
ET
RIe
Etu
ETg
Exfgwe
ET, RI^e, Exf_{gw}^e, ET_u, and ET_g (mm.day^{-1})
Oct-09
Jan-10
Apr-10
Jul-10
Oct-10

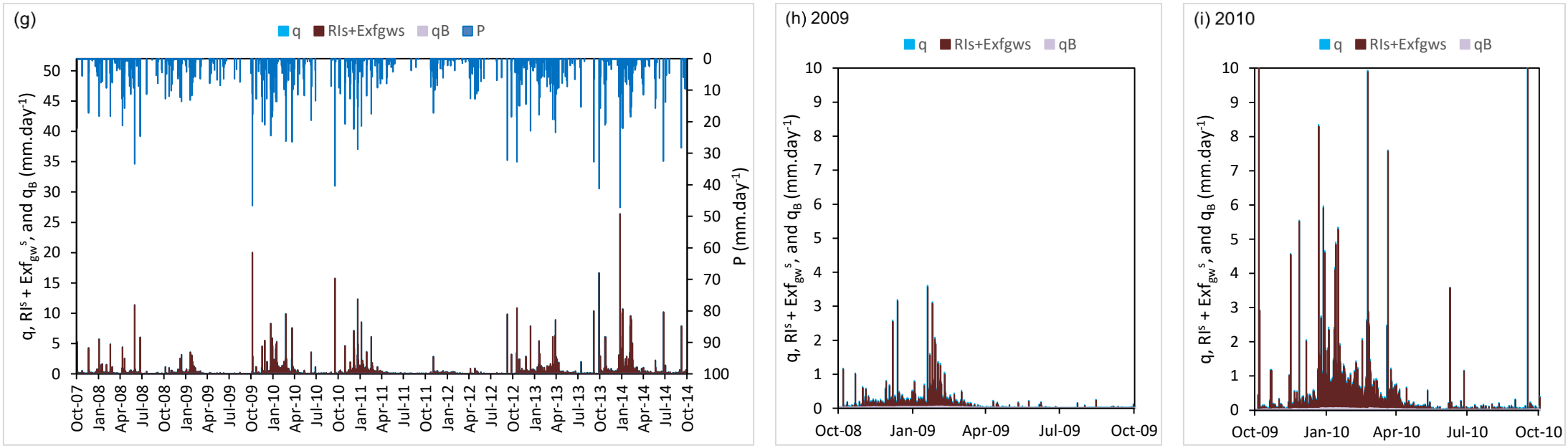

Figure 24: Daily variability of different water fluxes: (a) groundwater zone fluxes over the 7-year simulation period, (b) groundwater zone fluxes in 2009 (dry year), (c) groundwater zone fluxes in 2010 (wet year), (d) evapotranspiration fluxes over the 7-year simulation period, (e) evapotranspiration fluxes in 2009 (dry year), (f) evapotranspiration fluxes in 2010 (wet year), (g) streamflow fluxes over the 7-year simulation period, (h) streamflow fluxes in 2009 (dry year), and (i) streamflow fluxes in 2010 (wet year).

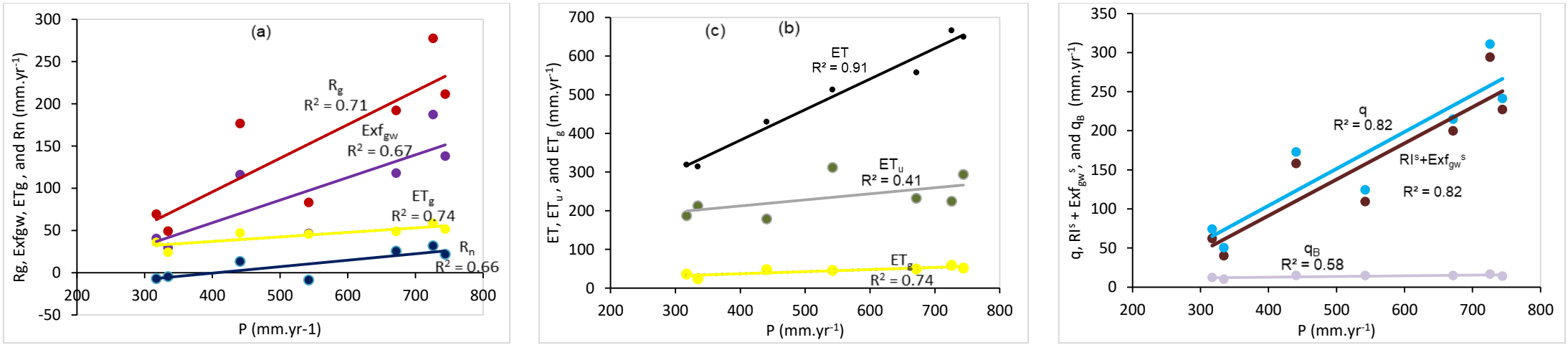

Figure 25: Correlation of yearly water fluxes between: (a) groundwater fluxes versus precipitation, (b) evapotranspiration fluxes versus precipitation, and (c) streamflow fluxes versus precipitation.

5.6. Sensitivity Analysis

The results of the sensitivity analysis were limited to the statistical calibration results of the model solution, particularly the effect of changing the model parameters on the overall $RMSE$ of the simulated heads and the VE of the simulated streamflow. The model solution was tested against the changes in the calibration parameters shown in Table 1 in addition to the GNC package activation. The deactivation of the GNC package showed a low change in the overall heads $RMSE$ (11%). This confirmed the advantage of the Voronoi grid to closely honour the CVFD connection requirements without the need of the GNC package. Only the figures of 6 parameters (most important parameters according to previous studies and personal judgement) among all other parameters were shown herein (Figure 26) due to the text size limitation to show all the figures. Changes in all the 6 parameters including unsaturated zone (θ_{resid} and θ_{sat}) and groundwater zone parameters (K_h, K_v, S_s and S_y) had significant changes on the model solution.

It was observed that the model solution was significantly sensitive to: (a) increasing S_y by 150% lead to increasing the overall $RMSE$ by 86% and the VE by 56%, (b) decreasing S_y by 50% lead to increasing the overall $RMSE$ by 77%, (c) increasing K_h by 150% lead to increasing the overall $RMSE$ by 47% and the VE by 56%, and (d) decreasing K_v by 50% lead to increasing the overall $RMSE$ by 42% and the VE by 50%.

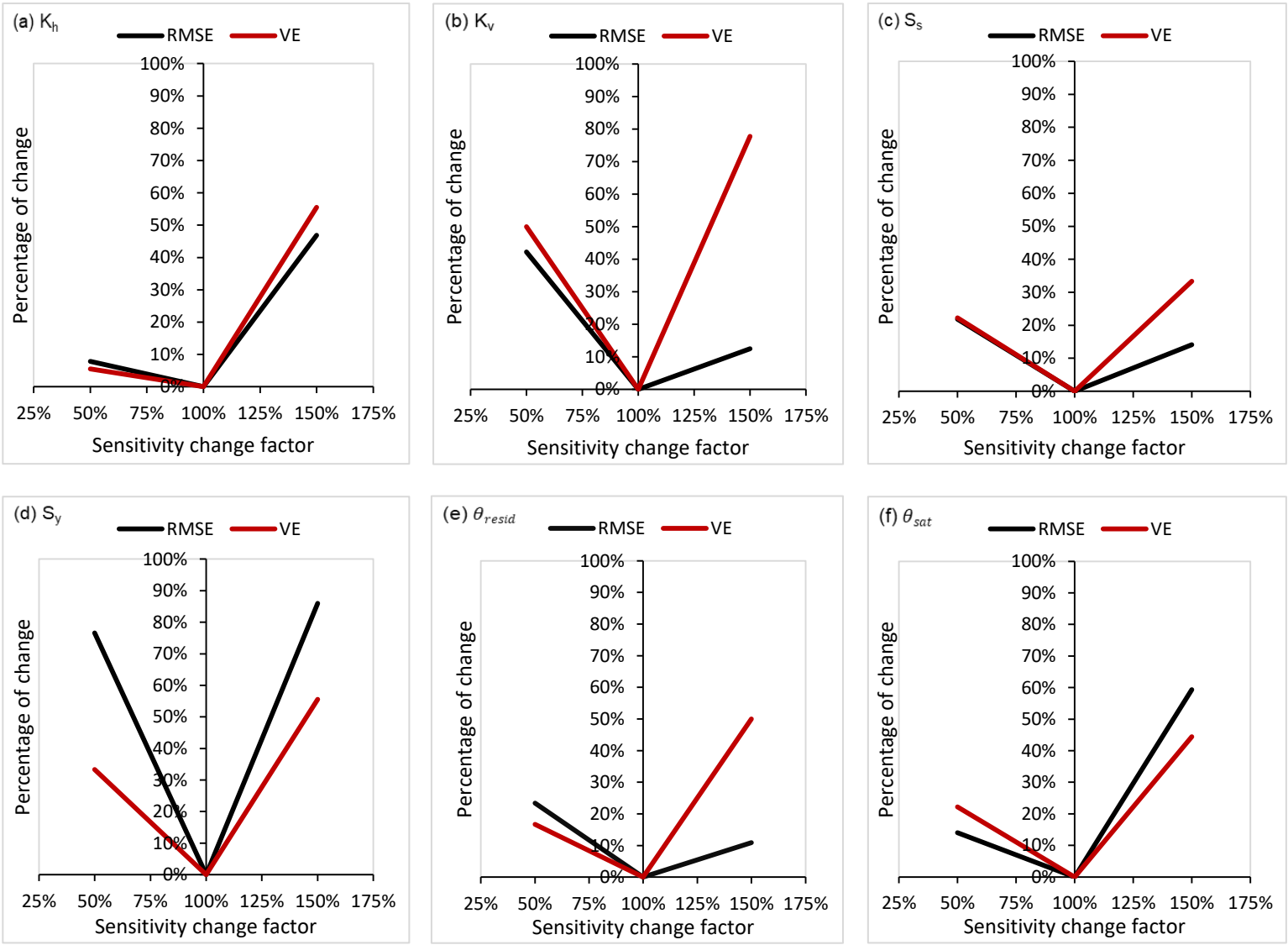

Figure 26: Sensitivity analysis of the model parameters: (a) K_h, (b) K_v, (c) S_s, (d) S_y, (e) θ_{resid}, and (f) θ_{sat}.

The lowest changes in the model solution were observed in: (a) decreasing K_h by 50% lead to increasing the overall $RMSE$ by 8% and the VE by 6%, (b) decreasing S_s by 50% lead to increasing the overall $RMSE$ by 22% and the VE by 22%. Some contradictory changes were also observed between $RMSE$ and VE such as: (a) increasing θ_{resid} by 150% lead to increasing the overall $RMSE$ by 11% but the VE by 50%, and (b) increasing K_v by 150% lead to increasing the overall $RMSE$ by only 13% but the VE by 78%. Such difference response between the $RMSE$ of the groundwater heads and the VE of the streamflow confirmed the difficulty of modelling surface-groundwater interaction, with different response to changes in some of the model parameters.

6. DISCUSSION

6.1. Surface-groundwater interactions in the Sardon catchment

The Sardon catchment includes the characteristics of both hard rock systems (HRSs) and water-limited environments (WLEs). Applying the integrated hydrological model (IHM) in such area is more reliable than the standalone model (Hassan et al. 2014). This is because IHM provides better, more detailed and more realistic possibility of system conceptualization, more realistic system discretization, more appropriate numerical solution resulting in more detailed and more realistic water balance. For example, in this study, the unsaturated zone processes, governing surface-groundwater interactions, had large impacts on the groundwater zone and the total water balance.

The transient calibration showed a good match between the observed and the simulated variables (groundwater heads and streamflow), but still, there are some discrepancies. Considering groundwater heads, the reasons for discrepancies can be due to: (a) errors in model conceptualization, (b) errors in model parameterization, (c) uncertainty in the observed head records, and (d) the effect of the grid-scale variability that affect the simulated groundwater depth relative to the elevation of the observed points. Considering the streamflow, the reasons for discrepancies can be due to: (a) errors in model conceptualization, (b) errors in model parameterization, and (c) inaccuracy in the flume discharge measurements.

The water balance of the Sardon catchment showed the significance of simulating the unsaturated zone and its impact on the variability of groundwater fluxes and the total water balance. The unsaturated zone fluxes (P_e, ET_u) were substantially higher than the groundwater zone fluxes (R_g , ET_g and Exf_{gw}), most likely due to: (a) the high losses occurred in the unsaturated zone (as ET_u was the main contribution to the total ET (66.5%)) which restricted the R_g, (b) PET was almost satisfied by ET_u, so ET_g was low and (c) the low storage of the groundwater zone minimized the R_g but enhanced the Exf_{gw}.

The two applied concepts, re-infiltration and cascade routing (CR), were reflected in the water balance, as 22.4% of the rejected components ($RI + Exf_{gw}$) were re-infiltrated ($RI^{ri} + Exf_{gw}^{ri}$) but in different zones where the soil was not saturated yet, and 62.5% of the ($RI + Exf_{gw}$) were routed to streams ($RI^{s} + Exf_{gw}^{s}$). As a result, the two concepts changed the: (a) R_g (from 28% to 37% of P), (b) Exf_{gw} (from 18% to 26% of P), (c) ET (from 91% to 66.2% of P), and (d) q (from 6% to 31.5% of P).

The characteristics of the Sardon catchment is reflected by specific aquifer dynamics (recharge/discharge conditions) in response to different climatic conditions. In 2009, considered as a dry year with P = 317.22 mm.yr^{-1}, more discharge areas were observed with average yearly R_n= -6.35 mm.yr^{-1}, while in 2010, considered as a wet year with P = 744.14 mm.yr^{-1}, more recharge areas were observed with average yearly R_n= 22.13 mm.yr^{-1}. The Sardon catchment characteristics (shallow water tables) was also reflected in the large Exf_{gw}, as Exf_{gw} was the main output from the groundwater zone (69% of R_g), which confirms the relevance of Exf_{gw} in the Sardon catchment and generally in any HRSs-WLEs with shallow water table condition. Considering that relevance and also very little scientific information on that water balance component, the Exf_{gw} needs to be further explored in future studies (also experimentally with field observations) to better understand this process and increase confidence in its quantification through the numerical hydrological models' such as the one proposed in this study.

The spatial distribution of Exf_{gw} almost followed the pattern of the spatial distribution of R_g, most likely due to the Sardon catchment characteristics (shallow water tables and fast responses to recharge). In shallow water table condition, when in a layer with low storage, during (and/or shortly after) large showers, water table rises spontaneously towards the ground surface reaching the level when Exf_{gw} starts. Consequently, R_g and Exf_{gw} are observed in the same zones at the same time as can be observed in Figure 21 and Figure 22 and confirmed by the high correlation (0.99) between R_g and Exf_{gw}. The spatial distribution of ET_g showed a partially similar pattern of the spatial distribution of Exf_{gw}, as both fluxes depend on the water table position. ET_g was high in the drainage areas (along the streams) due to shallow water table conditions and relatively large extinction depth (d_{ext}) (existence of the two tree species, with d_{ext} = 3.7 m).

The spatial distribution of R_n showed a mosaic pattern where the recharge and discharge areas are close to each other, as shown in Figure 21 and Figure 22. This mosaic pattern does not follow the standard flownet concept of Tóth (1963) which indicates that the boundaries between recharge and discharge areas are well defined (recharge areas in elevated areas and discharge areas in depressions) and do not signify an abrupt change. However, the observed mosaic pattern is characteristic of HRSs and was already acknowledged by the former study of Hassan et al. (2014) in the Sardon catchment. In general, the spatial distribution for all the fluxes in both dry and wet years is significant. The reasons for this spatial distribution are most likely due to: (a) hilly topography, (b) land cover changes, (c) existence of faults, fractures and outcrops, and (d) shallow water table conditions with dense drainage network.

The observed significant temporal variability of the R_g and Exf_{gw} was due to the high temporal variability of P, which is typical for the Sardon catchment. During the wet period (December to February), R_g and Exf_{gw} peaks were extremely high (up to 4 and -3 mm.day^{-1} respectively), in contrast to low values or zero in the dry periods (June to August). Also, the temporal variability of ET_g was observed as the ET_g depends on: (a) the position of the groundwater table, which was highly temporally variable as dependant on the temporal variability of P, and (b) the temporal variability of PET. Therefore, ET_g was observed with high values in the spring period (March to May) due to moderately high PET and shallow groundwater table, comparing to low values in the autumn period (September to November) due to moderately low PET and deep groundwater table.

The temporal variability of R_n was affected by the temporal variability of the R_g, ET_g and Exf_{gw}. The R_n had positive peaks (recharge conditions) during the winter period (December to February), when R_g was high (due to high P), Exf_{gw} was high (due to shallow groundwater table) but ET_g was low (due to low PET). During the spring period (March to May), R_n had negative peak values (discharge conditions) due to moderately high R_g (moderately high P), moderately high Exf_{gw} (shallow groundwater table), but high ET_g (high PET and shallow groundwater table). During the summer period (June to August), R_n was low or zero due to low or zero R_g (low or zero P), low or zero Exf_{gw} (deep groundwater table), and low ET_g (high PET but deep groundwater table).

6.2. Experience MODFLOW 6

Applying MODFLOW 6 in the Sardon catchment had many advantages. MODFLOW 6 has the advantage of using any kind of structured or unstructured grid for the model. In this study, the most flexible, Voronoi grid, was selected among other types of grids, benefiting from its ability to realistically represent the most important hydrogeological features, such as the curvatures of the Sardon streams, faults and sharp boundaries of block heterogeneities. For example, the Sardon streams were represented by minimal grid cells width (~15-20 m), almost close to the real width of those streams (~10 m), which enhanced the quality and accuracy of the simulation. Another advantage of the Voronoi grid was its honour to follow the CVFD connection requirements, which reduced the need to use the GNC package for simulation corrections (errors in simulated heads and flow due to violation of the CVFD). This was confirmed in this study by activating and deactivating the GNC package, where the GNC deactivation showed low sensitivity effect on the model solution (11% change in overall groundwater heads $RMSE$).

Furthermore, MODFLOW 6 introduced new concepts in the UZF package, which improve the simulation of the unsaturated zone. For example, the Exf_{gw} has more reliable simulation in MODFLOW 6 than in previous MODFLOW

versions because of the newly introduced d_{surf} option, allowing the Exf_{gw} to start from below the land surface. Besides, MODFLOW 6 better represents the parameter θ_{resid} (residual water content) of the unsaturated zone than the previous MODFLOW versions, where θ_{resid} was approximated to specific retention (S_r); in reality, the θ_{resid} is much smaller than S_r (volume of water per unit volume of rock retained in that rock against gravity drainage. As such in MODFLOW 6, the θ_{resid} represents the truly residual water content.

MODFLOW 6 had shown new concepts related to RI and Exf_{gw} through the use of the MVR package. The MVR package was used in this study to control the RI and Exf_{gw} where each of them could be either evapotranspired or moved downslope; the latter in turn could be either re-infiltrated in the downward cell (UZF Package) or discharged in adjacent streams (SFR Package). Transferring the RI and Exf_{gw} from the providers (UZF upslope cells) to the receivers (UZF downslope cells or SFR reaches) was done by defining the mover fractions using the FACTOR option in the MVR package. However, the MVR package does not have an automatic way (e.g. local land surface gradient) to define these mover fractions. The mover fractions were determined in a preliminary step using the CR concept based on the land surface gradient, as explained in section 4.5.5.4. The applied CR concept allowed for proper routing of the surface flow, in a closer way to the surface-runoff models or the fully coupled IHMs such as GSFLOW. The effect of applying the CR concept was observed significantly in the water balance components ET and q, as without the CR, ET and q = 91% and 6% of P respectively, while with the CR, ET and q = 66.2% and 31.5% of P respectively. The results of the (with CR) case showed more realistic ET and q values, closer to the ET and q values (ET and q = 73% and 27.3% of P respectively) of the former, GSFLOW modelling study of Hassan et al. (2014). This way of using the MVR package with applying the CR concept shows the advantage of MODFLOW 6 to enhance the simulation of the surface-groundwater interaction systems.

However, the same MVR FACTOR was applied for both RI and Exf_{gw} with no way to assign separate fractions to each of them, which is the MODFLOW 6 software limitation. Since RI and Exf_{gw} are different processes, there is a need to split them when moving these amounts of water to other features, especially from a transport perspective. For example, for cases of irrigated agriculture systems, the RI could be driven from an intense rainfall event with essentially no TDS, while the Exf_{gw} would carry with it the TDS of the groundwater. Moreover, impossibility to split RI and Exf_{gw} has water balance implication as they had to be counted together as ($RI^{ri} + Exf_{gw}^{ri}$) and ($RI^{s} + Exf_{gw}^{s}$). After reporting this problem to the USGS team of MODFLOW 6, they confirmed that the 'splitting-problem' will be handled in the coming version of MODFLOW 6 (v-mf6.1).

6.3. Comparison with Hassan et al. (2014)

The results of this study were compared with the former study of Hassan et al. (2014), who used different conceptual model and different numerical solution. The conceptual model of the study of Hassan et al. (2014) followed the conceptual model of the former study of Lubczynski & Gurwin (2005). In contrast, this study followed the conceptual model of the former study of Francés et al. (2014) based on the general 3D geological conceptual model of granite aquifers, defined by Dewandel et al. (2006). Both conceptual models of Lubczynski & Gurwin (2005) and Francés et al. (2014) have the same definition of the aquifer layers (layer one is the saprolite layer, and layer two is the fissured layer), but with different layers thickness and spatial distribution of the outcrops. Additionally, the transition of the heterogeneity field in the conceptual model of Lubczynski & Gurwin (2005) (Figure 3) is relatively smooth, compared to a sharp transition in the conceptual model of Francés et al. (2014) (Figure 7).

Regarding the numerical codes applied, Hassan et al. (2014) used GSFLOW (based on the coupling of PRMS and MODFLOW-2005), while in this study, MODFLOW 6 was used. The difference between the two model's conceptualization, in addition to some differences in parametrization, lead to different results. GSFLOW is a fully coupled hydrological model, coupling a surface model (PRMS) with a subsurface model (MODFLOW-2005), while MODFLOW 6 is a subsurface model taking into consideration the effect of the land surface processes. The different concepts between the two models were reflected in the water balance representation of the two studies. The water balance zones of the study of Hassan et al. (2014) consisted of four zones (surface zone, soil zone, percolation zone and groundwater zone),

while in this study, the water balance zones consisted of two zones (unsaturated zone and the groundwater zone). Additionally, the study of Hassan et al. (2014) included more parameters related to the four defined zones which did not exist in this study. Different parametrization and applied methods were observed in (a) different distribution of hydraulic and storage parameters of the unsaturated and saturated zones, (b) different estimation of the driving forces (effective precipitation and potential evapotranspiration, and (c) different simulation of overland flow; in Hassan et al. (2014), schematized through polygons representing hydrological response units (HRUs) accounting for land-surface resistance differences but without re-infiltration option, versus the Voronoi unstructured grid in this study better simulating topographic variability due to application of Voronoi unstructured grid and with re-infiltration concept, but simplifying land surface feature differences, accounting only for differences in soil infiltration in the UZF package.

The study of Hassan et al. (2014), GSFLOW-based, showed its advantage in representing the streamflow by introducing more hydrological components. They defined the total streamflow (q) as ($q = q_H + q_D + q_i + q_B$), where q_H is the Hortonian flow (infiltration excess runoff); q_D is the Dunnian flow (saturation excess runoff); q_i is the interflow (flow simulated by the soil zone); and q_B is the baseflow. In contrast, in this study, MODFLOW 6-based, the total stream flow was defined as ($q = RI^s + Exf_{gw}^s + q_B$), where RI^s is the rejected infiltration routed to streams; Exf_{gw}^s is the groundwater exfiltration routed to streams; and q_B is the baseflow.

In contrast to the GSFLOW model of Hassan et al. 2014, MODFLOW 6 has no ability to simulate q_i and no automatic way to represent q_H and q_D. However, in this study, the q_H and q_D were inherently simulated through components RI^s and Exf_{gw}^s. Figure 27 shows two cases of the streamflow defining the relationship between these components; case (a) showed the occurrence of q_H when the applied infiltration rate exceeds the K_{sat}, while case (b) showed the occurrence of q_D when the soil is fully saturated. In principle, there is a possibility to define q_H, q_D from the MODFLOW 6 output files using the information of P, RI^s and Exf_{gw}^s, but it needs a sort of script (in this study, Python script) to differentiate spatially and temporally between the areas that will have q_H and the areas that will have q_D. However, this method was not implemented in this study because of time limitation, and also because it does not affect the water balance.

(a)

Rejected infiltration occurred when the applied infiltration rate (q_a) exceeds the saturated hydraulic conductivity (K_{sat}). In this case example: q_a = P.

$q_H = RI^s$ when $P > K_{sat}$

(b)

Rejected infiltration and groundwater exfiltration occurred because the soil is fully saturated.

$q_D = RI^s + Exf_{gw}^s$ if $P > 0$

$q_D = Exf_{gw}^s$ if $P \leq 0$

d_{surf}: the depth below the land surface where the groundwater exfiltration can start.

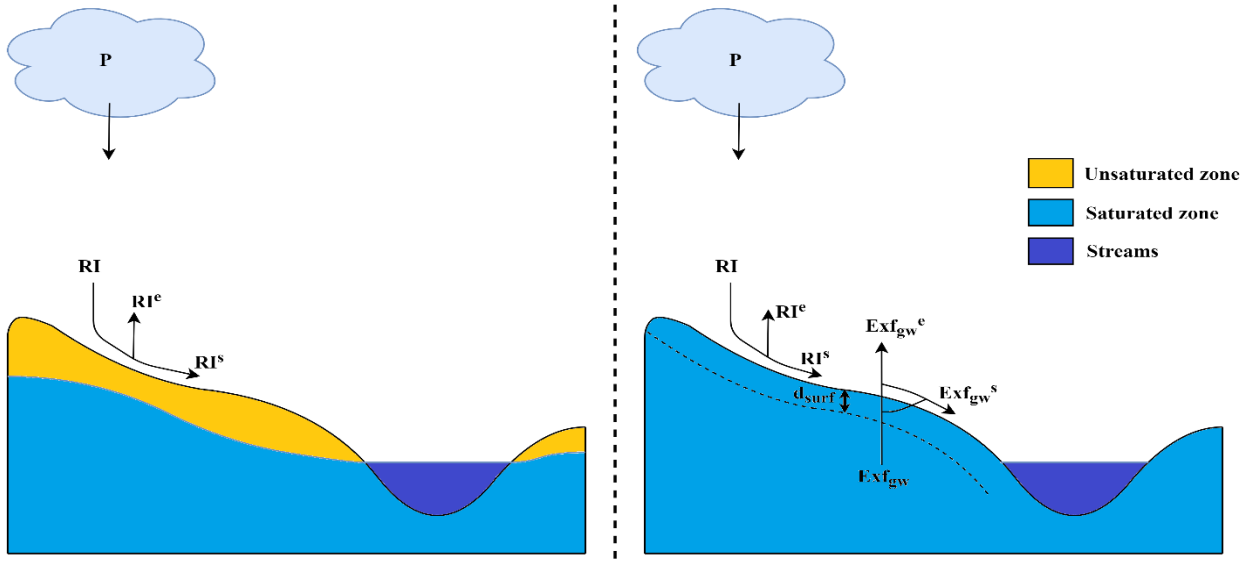

Figure 27: Two different cases for the streamflow, (a) representing Hortonian flow, and (b) representing Dunnian flow.

Both studies showed good calibration results, with overall groundwater heads $RMSE \leq 1$ m, individual groundwater $RMSE$ for the observation points in the range of 0.13 m to 1 m, and streamflow $VE \sim 0.5$.

Considering, the water balance, the two studies showed similar, i.e. with the same order of magnitude results for the individual water balance components. However, in this study, before applying the CR concept within the MVR package, a large difference in the water balance components, ET and q, were observed between the two studies. In this study, without using the CR concept, the ET and q were 91% and 6% of P respectively, while with the CR concept, the ET and q were 66.2% and 31.5% of P respectively, comparing to 73 % and 27.3 % of P respectively in the study of Hassan et al. (2014).

Both studies showed different temporal variability of ET_g, as the peaks of ET_g at Hassan et al. (2014) occurred in summer (June), but in this study in spring (April). The likely reason is that they used ($PET = ET_o$, peaks of ET_o are in summer), and in this study, ($PET = ET_o * K_c$), where the K_c is max at the spring time, as confirmed by the NDVI derived from the Landsat 7 TM images (described in section 4.3.2.5).

In general, MODFLOW 6 showed great ability to simulate surface-groundwater interactions within one, single modelling environment, similar to the fully coupled IHM such as GSFLOW while being more efficient considering its processing time and also improved regarding groundwater domain thanks to elimination of number of shortcomings present in older MODFLOW versions. The methods applied in this study (spatial-temporal driving forces estimation, unstructured grid, re-infiltration concept and the CR concept) enrich the MODFLOW 6 ability to provide better simulation of surface-groundwater systems.

7. CONCLUSION AND RECOMMENDATIONS

7.1. Conclusion

The Sardon catchment is a hard rock system with shallow water table conditions, dense drainage network, high heterogeneity and low storage conditions. Besides, it is a water-limited environment with high temporal variability of rainfall and fast aquifer responses to recharge. All these characteristics lead to complex, surface-groundwater interactions, which if to be realistically modelled, require the use of front line, modelling tools such as an IHM.

The water balance of the Sardon catchment showed the importance of the unsaturated zone in simulating surface-groundwater interactions. The ET_u was the main contribution to the total ET, while the unsaturated zone processes affected the groundwater zone fluxes (R_g , ET_g and Exf_{gw}) and the total water balance. The complexity of the system dynamics was reflected by large spatial and temporal variability of groundwater fluxes implying spatial recharge/discharge conditions conformed to typical for HRS-WLE mosaic pattern of R_n and fast recharge response to rainfall enhanced by low storage, resulting also in substantial Exf_{gw} contribution to water balance.

The calibration of long transient hydrological models is challenging and time-consuming, especially when using more modelling functions implemented in the new versions of groundwater numerical models such as MODFLOW 6. However, the new modelling developments showed their power to enhance the representation and the understanding of complex hydrology systems such as the Sardon catchment. In this study, MODFLOW 6 allowed for using a Voronoi unstructured grid which realistically represents the most important hydrogeological features, such as the curvatures of the Sardon streams and faults. Regarding the water balance, MODFLOW 6 showed more realistic representations in the UZF package than former versions of MODFLOW, by introducing a proper definition of the term θ_{resid}, and by allowing the Exf_{gw} to start from below the land surface. Additionally, the use of the MVR package, with applying the CR concept, enhanced the simulation of the surface-groundwater interaction in terms of applying the re-infiltration concept and better representing the overland flow than in former versions of MODFLOW.

Concluding, by applying MODFLOW 6 in the Sardon study area, introduced new valuable capabilities in terms of grid flexibility and new system concepts as well as numerical solutions in system parameterization and water balancing, that together improve the knowledge of the Sardon catchment hydrology. Once the surface flow component of MODFLOW 6 will be improved, for example as proposed in this study, the MODFLOW 6 will become true-IHM, that will not need any more coupling with separate surface flow software to study surface-groundwater interactions.

7.2. Recommendations

The $LAI\&S$ formula, used in the process of estimating the grass interception was defined by Menzel (1997). The climatic and soil conditions of the study area (in Switzerland) analysed by Menzel (1997) was different from the Sardon area (clay-sandy soil compared to hard rock for the Sardon area, cooler climate and higher average precipitation than the Sardon area). Therefore, more investigations of a specific $LAI\&S$ formula for the Sardon area is recommended for future studies. This could be achieved by obtaining some LAI field measurements with determining a correlation between the measured LAI and the LAI retrieved from remote sensing.

The estimation of the potential evapotranspiration (PET) was done in a spatial-temporal manner using the crop coefficient (K_c). However, K_c were calculated for only one year (2010) with the assumption that these K_c values are applicable and valid for all other years of the model simulation period. It is recommended to calculate individual K_c for each year of the model simulation period to have a better representation of the PET. This is expected to improve the water balance representation of the Sardon catchment.

Considering overland flow, the resistance of surface objects (e.g. surface roughness of objects) should be introduced to surface flow routing and also the retrieval of $q_H \text{ and } q_D$ separately from the rejected infiltration and from groundwater exfiltration.

The data used in this study were from the period of October 2007 to September 2014. The Sardon catchment has the advantage of the ADASs with automatic recording of many hydrological data needed for hydrology studies. The data from 2014 up till now exists and can be a good option to use it for further studies. Additionally, the data recording in the area started from 1997, so having a long record of data (from 1997 up till now) can be very useful for studying the impact of climate change in the Sardon catchment.

From a transport perspective, an option is to use the conservative tracer (e.g. NaCl) as a state variable to improve the reliability of the calibration of Sardon hydrological models. Another option is to analyse the impact of contamination, such as pesticides on the water resources of the Sardon catchment.

LIST OF REFERENCES

Allen, R., Pereira, L., Raes, D., & Smith, M. (1998). Crop evapotranspiration - Guidelines for computing crop water requirements - FAO Irrigation and drainage paper 56. In *Food and Agriculture Organization of the United Nations*.

Allison, G. B., Cook, P. G., Barnett, S. R., Walker, G. R., Jolly, I. D., & Hughes, M. W. (1990). Land clearance and river salinisation in the western Murray Basin, Australia. *Journal of Hydrology*, *119*(1–4), 1–20. https://doi.org/10.1016/0022-1694(90)90030-2

Anderson, M. P., Woessner, W. W., & Hunt, R. J. (2015). *Applied groundwater modeling : simulation of flow and advective transport* (Second edi).

Bakker, M., Post, V., Langevin, C. D., Hughes, J. D., White, J. T., Starn, J. J., & Fienen, M. N. (2016). Scripting MODFLOW Model Development Using Python and FloPy. *Groundwater*, *54*(5), 733–739. https://doi.org/10.1111/gwat.12413

Balugani, E., Lubczynski, M. W., Reyes-Acosta, L., van der Tol, C., Francés, A. P., & Metselaar, K. (2017). Groundwater and unsaturated zone evaporation and transpiration in a semi-arid open woodland. *Journal of Hydrology*, *547*, 54–66. https://doi.org/10.1016/j.jhydrol.2017.01.042

Campos, I., Neale, C. M. U., Calera, A., Balbontín, C., & González-Piqueras, J. (2010). Assessing satellite-based basal crop coefficients for irrigated grapes (Vitis vinifera L.). *Agricultural Water Management*, *98*(1), 45–54. https://doi.org/10.1016/j.agwat.2010.07.011

Campos, I., Villodre, J., Carrara, A., & Calera, A. (2013). Remote sensing-based soil water balance to estimate Mediterranean holm oak savanna (dehesa) evapotranspiration under water stress conditions. *Journal of Hydrology*. https://doi.org/10.1016/j.jhydrol.2013.04.033

Canadell, J., Jackson, R. B., Ehleringer, J. R., Mooney, H. A., Sala, O. E., & Schulze, E. D. (1996). Maximum rooting depth of vegetation types at the global scale. *Oecologia*, *108*(4), 583–595. https://doi.org/10.1007/BF00329030

Choudhury, B. J., Ahmed, N. U., Idso, S. B., Reginato, R. J., & Daughtry, C. S. T. (1994). Relations between evaporation coefficients and vegetation indices studied by model simulations. *Remote Sensing of Environment*, *50*(1), 1–17. https://doi.org/10.1016/0034-4257(94)90090-6

Criss, R. E., & Winston, W. E. (2008). Do Nash values have value? Discussion and alternate proposals. *Hydrological Processes*, *22*(14), 2723–2725. https://doi.org/10.1002/hyp.7072

Dewandel, B., Lachassagne, P., Wyns, R., Maréchal, J. C., & Krishnamurthy, N. S. (2006). A generalized 3-D geological and hydrogeological conceptual model of granite aquifers controlled by single or multiphase weathering. *Journal of Hydrology*, *330*(1–2), 260–284. https://doi.org/10.1016/J.JHYDROL.2006.03.026

Doherty, J., & Hunt, R. (2010). Approaches to highly parameterized inversion: A guide to using PEST for groundwater-model calibration. In *U. S. Geological Survey Scientific Investigations Report 2010-5169*. https://doi.org/10.3133/sir20105169

El-Zehairy, A. A., Lubczynski, M. W., & Gurwin, J. (2018). Interactions of artificial lakes with groundwater applying an integrated MODFLOW solution. *Hydrogeology Journal*, *26*(1), 109–132. https://doi.org/10.1007/s10040-017-1641-x

Francés, A. P. (2015). *Integration of hydrogeophysics and remote sensing coupled with hydrological models*. https://doi.org/10.3990/1.9789036539166

Francés, A. P., Lubczynski, M. W., Roy, J., Santos, F. A. M., & Mahmoudzadeh Ardekani, M. R. (2014). Hydrogeophysics and remote sensing for the design of hydrogeological conceptual models in hard rocks – Sardón catchment (Spain). *Journal of Applied Geophysics*, *110*, 63–81. https://doi.org/10.1016/J.JAPPGEO.2014.08.015

Gash, J. H. C. (1979). An analytical model of rainfall interception by forests. *Quarterly Journal of the Royal Meteorological Society*, *105*(443), 43–55. https://doi.org/10.1002/qj.49710544304

Gash, J. H. C., Lloyd, C. R., & Lachaud, G. (1995). Estimating sparse forest rainfall interception with an analytical model. *Journal of Hydrology*, *170*(1–4), 79–86. https://doi.org/10.1016/0022-1694(95)02697-N

Gómez, J. A., Giráldez, J. V., & Fereres, E. (2001). Rainfall interception by olive trees in relation to leaf area. *Agricultural Water Management*, *49*(1), 65–76. https://doi.org/10.1016/S0378-3774(00)00116-5

Hassan, S. M. T., Ghimire, C. P., & Lubczynski, M. W. (2017). Remote sensing upscaling of interception loss from isolated oaks: Sardon catchment case study, Spain. *Journal of Hydrology*, *555*, 489–505. https://doi.org/10.1016/J.JHYDROL.2017.08.016

Hassan, S. M. T., Lubczynski, M. W., Niswonger, R. G., & Su, Z. (2014). Surface–groundwater interactions in hard rocks in Sardon Catchment of western Spain: An integrated modeling approach. *Journal of Hydrology*, *517*, 390–410. https://doi.org/10.1016/J.JHYDROL.2014.05.026

Henson, W. R., Medina, R. L., Mayers, C. J., Niswonger, R. G., & Regan, R. S. (2013). CRT-Cascade Routing Tool to

Define and Visualize Flow Paths for Grid-Based Watershed Models. In *U.S. Geological Survey Techniques and Methods 6-D2*. https://doi.org/10.3133/TM6D2

Hesch, W. (2014). *MODFLOW-USG Case Study Discussing Various Grid Geometries for MODFLOW-USG*.

Hughes, J. D., Langevin, C. D., & Banta, E. R. (2017). Documentation for the MODFLOW 6 framework. In *U.S. Geological Survey Techniques and Methods 6-A57*. https://doi.org/10.3133/tm6a57

Langevin, C. D., Hughes, J. D., Banta, E. R., Niswonger, R. G., Panday, S., & Provost, A. M. (2017). Documentation for the MODFLOW 6 Groundwater Flow Model. In *U.S. Geological Survey Techniques and Methods 6-A55*. https://doi.org/10.3133/tm6a55

Long, J. C. S., Remer, J. S., Wilson, C. R., & Witherspoon, P. A. (1982). Porous media equivalents for networks of discontinuous fractures. *Water Resources Research*, *18*(3), 645–658. https://doi.org/10.1029/WR018i003p00645

Lubczynski, M. W. (2009). The hydrogeological role of trees in water-limited environments. *Hydrogeology Journal*, *17*(1), 247–259. https://doi.org/10.1007/s10040-008-0357-3

Lubczynski, Maciek W., & Gurwin, J. (2005). Integration of various data sources for transient groundwater modeling with spatio-temporally variable fluxes—Sardon study case, Spain. *Journal of Hydrology*, *306*(1–4), 71–96. https://doi.org/10.1016/J.JHYDROL.2004.08.038

Maréchal, J. C., Wyns, R., Lachassagne, P., Subrahmanyam, K., & Touchard, F. (2003). Anisotropie verticale de la perméabilité de l'horizon fissuré des aquifères de socle : Concordance avec la structure géologique des profils d'altération. *Comptes Rendus - Geoscience*. https://doi.org/10.1016/S1631-0713(03)00082-8

Markstrom, S. L., Niswonger, R. G., Regan, R. S., Prudic, D. E., & Barlow, P. M. (2008). GSFLOW - Coupled Ground-Water and Surface-Water Flow Model Based on the Integration of the Precipitation-Runoff Modeling System (PRMS) and the Modular Ground-Water Flow Model (MODFLOW-2005). In *U.S. Geological Survey Techniques and Methods 6-D1*. https://doi.org/10.3133/TM6D1

McDonald, M. G., & Harbaugh, A. W. (1988). A Modular Three-Dimensional Finite-Difference Ground-Water Flow Model. In *U.S. Geological Survey, Techniques of Water-Resources Investigations 06-A1*. https://doi.org/10.3133/twri06A1

McMahon, T. A., Peel, M. C., Lowe, L., Srikanthan, R., & McVicar, T. R. (2013). Estimating actual, potential, reference crop and pan evaporation using standard meteorological data: a pragmatic synthesis. *Hydrology and Earth System Sciences*, *17*(4), 1331–1363. https://doi.org/10.5194/hess-17-1331-2013

Menzel, L. (1997). *Modellierung der Evapotranspiration im System Boden-Pflanze-Atmosphäre*. ETH Zürich. https://doi.org/10.3929/ETHZ-A-001696316

Newman, B. D., Wilcox, B. P., Archer, S. R., Breshears, D. D., Dahm, C. N., Duffy, C. J., McDowell, N. G., Phillips, F. M., Scanlon, B. R., & Vivoni, E. R. (2006). Ecohydrology of water-limited environments: A scientific vision. *Water Resources Research*, *42*(6). https://doi.org/10.1029/2005WR004141

Niswonger, R. G., Panday, S., & Ibaraki, M. (2011). MODFLOW-NWT, A Newton formulation for MODFLOW-2005. In *U.S. Geological Survey Techniques and Methods 6-A37*. https://doi.org/10.3133/TM6A37

Niswonger, R. G., & Prudic, D. E. (2005). Documentation of the Streamflow-Routing (SFR2) Package to Include Unsaturated Flow Beneath Streams - A Modification to SFR1. In *U.S. Geological Survey Techniques and Methods 6-A13*. https://doi.org/10.3133/TM6A13

Niswonger, R. G., Prudic, D. E., & Regan, R. S. (2006). Documentation of the Unsaturated-Zone Flow (UZF1) Package for modeling Unsaturated Flow Between the Land Surface and the Water Table with MODFLOW-2005. In *U.S. Geological Survey Techniques and Methods 6-A19*. https://doi.org/10.3133/TM6A19

Panday, S., Langevin, C. D., Niswonger, R. G., Ibaraki, M., & Hughes, J. D. (2013). MODFLOW–USG version 1: An unstructured grid version of MODFLOW for simulating groundwater flow and tightly coupled processes using a control volume finite-difference formulation. In *U.S. Geological Survey Techniques and Methods 6-A45*. https://doi.org/10.3133/TM6A45

Parsons, A. J., & Abrahams, A. D. (2009). Geomorphology of desert environments. In *Geomorphology of Desert Environments*. Springer Netherlands. https://doi.org/10.1007/978-1-4020-5719-9

Qin, C., Zhu, A. -X., Pei, T., Li, B., Zhou, C., & Yang, L. (2007). An adaptive approach to selecting a flow-partition exponent for a multiple-flow-direction algorithm. *International Journal of Geographical Information Science*, *21*(4), 443–458. https://doi.org/10.1080/13658810601073240

Quinn, P., Beven, K., Chevallier, P., & Planchon, O. (1991). The prediction of hillslope flow paths for distributed hydrological modelling using digital terrain models. *Hydrological Processes*, *5*(1), 59–79. https://doi.org/10.1002/hyp.3360050106

Reyes-Acosta, J. L., & Lubczynski, M. W. (2013). Mapping dry-season tree transpiration of an oak woodland at the catchment scale, using object-attributes derived from satellite imagery and sap flow measurements. *Agricultural and Forest Meteorology*, *174–175*, 184–201. https://doi.org/10.1016/j.agrformet.2013.02.012

Salvati, L., Zitti, M., Di Bartolomei, R., & Perini, L. (2013). Climate Aridity under Changing Conditions and Implications for the Agricultural Sector: Italy as a Case Study. *Geography Journal*, *2013*, 7. https://doi.org/10.1155/2013/923173

Singhal, B. B. S., & Gupta, R. P. (2010). *Applied Hydrogeology of Fractured Rocks* (2nd ed.). Springer Netherlands. https://doi.org/10.1007/978-90-481-8799-7

Spanoudaki, K., Stamou, A. I., & Nanou-Giannarou, A. (2009). Development and verification of a 3-D integrated surface water–groundwater model. *Journal of Hydrology*, *375*(3–4), 410–427. https://doi.org/10.1016/J.JHYDROL.2009.06.041

Tekle, Y. W. (2017). *Scaling up Sardon Catchment groundwater recharge into Dehesa (Montado) hard rocks of Iberian peninsula*.

Tóth, J. (1963). A theoretical analysis of groundwater flow in small drainage basins. *Journal of Geophysical Research*, *68*(16), 4795–4812. https://doi.org/10.1029/jz068i016p04795

Vandermolen, J. (n.d.). *MODFLOW-USG and Voronoi Cells | Waterloo Hydrogeologic*.

Vegas Galdos, F., Álvarez, C., García, A., & Revilla, J. A. (2012). Estimated distributed rainfall interception using a simple conceptual model and Moderate Resolution Imaging Spectroradiometer (MODIS). *Journal of Hydrology*, *468–469*, 213–228. https://doi.org/10.1016/j.jhydrol.2012.08.043

Weiss, M., & Baret, F. (2016). *Sentinel2 ToolBox Level2 Products S2ToolBox Level 2 products: LAI, FAPAR, FCOVER Version 1.1*.

Weldemichael, M. Y. (2016). *Integrated numerical modeling applying stratiform hydrological conceptual model, Sardon catchment study case, Spain*.

Winston, R. B. (2019). ModelMuse Version 4: A graphical user interface for MODFLOW 6. In *U.S. Geological Survey Scientific Investigations Report 2019–5036*. https://doi.org/10.3133/sir20195036